

## Stratigraphy, mineralogy, and origin of layered deposits inside Terby crater, Mars

V. Ansan<sup>a,\*</sup>, D. Loizeau<sup>b</sup>, N. Mangold<sup>a</sup>, S. Le Mouélic<sup>a</sup>, J. Carter<sup>b</sup>, F. Poulet<sup>b</sup>, G. Dromart<sup>c</sup>, A. Lucas<sup>a</sup>, J.-P. Bibring<sup>b</sup>, A. Gendrin<sup>b</sup>, B. Gondet<sup>b</sup>, Y. Langevin<sup>b</sup>, Ph. Masson<sup>d</sup>, S. Murchie<sup>e</sup>, J.F. Mustard<sup>f</sup>, G. Neukum<sup>g</sup>

<sup>a</sup>Laboratoire de Planétologie et Géodynamique de Nantes, Université de Nantes/CNRS UMR6112, 2 rue de la Houssinière, BP 92208, 44322 Nantes, France

<sup>b</sup>Institut Astrophysique Spatiale, Université Paris-Sud/CNRS, UMR 8617, 91405 Orsay cedex, France

<sup>c</sup>Laboratoire de Sciences de la Terre, ENS Lyon/CNRS/Université Lyon 1, UMR 5570, 69622 Villeurbanne, France

<sup>d</sup>Lab. IDES, CNRS UMR 8148, Université Paris-Sud/CNRS, 91420 Orsay cedex, France

<sup>e</sup>Johns Hopkins Univ., Appl. Phys. Lab., Johns Hopkins Rd., Laurel, MD 20723, USA

<sup>f</sup>Brown Univ., Dept. Geol. Sci., Providence, RI 02912, USA

<sup>g</sup>Freie Universitaet Berlin, Fachbereich Geowissenschaften, Malteserstr. 74-A, 12249 Berlin, Germany

### ARTICLE INFO

#### Article history:

Received 4 January 2010

Revised 6 September 2010

Accepted 10 September 2010

Available online 19 September 2010

#### Keywords:

Mars, surface

Infrared observations

Geological processes

Cratering

Image processing

### ABSTRACT

The 174 km diameter Terby impact crater (28.0°S–74.1°E) located on the northern rim of the Hellas basin displays anomalous inner morphology, including a flat floor and light-toned layered deposits. An analysis of these deposits was performed using multiple datasets from Mars Global Surveyor, Mars Odyssey, Mars Express and Mars Reconnaissance Orbiter missions, with visible images for interpretation, near-infrared data for mineralogical mapping, and topography for geometry. The geometry of layered deposits was consistent with that of sediments that settled mainly in a sub-aqueous environment, during the Noachian period as determined by crater counts. To the north, the thickest sediments displayed sequences for fan deltas, as identified by 100 m to 1 km long clinofolds, as defined by horizontal beds passing to foreset beds dipping by 6–10° toward the center of the Terby crater. The identification of distinct sub-aqueous fan sequences, separated by unconformities and local wedges, showed the accumulation of sediments from prograding/onlapping depositional sequences, due to lake level and sediment supply variations. The mineralogy of several layers with hydrated minerals, including Fe/Mg phyllosilicates, supports this type of sedimentary environment. The volume of fan sediments was estimated as >5000 km<sup>3</sup> (a large amount considering classical martian fan deltas such as Eberswalde (6 km<sup>3</sup>)) and requires sustained liquid water activity. Such a large sedimentary deposition in Terby crater is characteristic of the Noachian/Phyllosian period during which the environment favored the formation of phyllosilicates. The latter were detected by spectral data in the layered deposits of Terby crater in three distinct layer sequences. During the Hesperian period, the sediments experienced strong erosion, possibly enhanced by more acidic conditions, forming the current morphology with three mesas and closed depressions. Small fluvial valleys and alluvial fans formed subsequently, attesting to late fluvial processes dated as late Early to early Late Hesperian. After this late fluvial episode, the Terby impact crater was submitted to aeolian processes and permanent cold conditions with viscous flow features. Therefore, the Terby crater displays, in a single location, geologic features that characterize the three main periods of time on Mars, with the presence of one of the thickest sub-aqueous fan deposits reported on Mars. The filling of Terby impact crater is thus one potential “reference geologic cross-section” for Mars stratigraphy.

© 2010 Elsevier Inc. All rights reserved.

### 1. Introduction

Fresh craters falling within the 100–200 km range should be displayed as a large circular depression with a central peak or with a peak ring and sharp rims, as seen on the Moon. In contrast, many ancient large (>20 km-in-diameter) impact craters observed on Mars in

Viking images have anomalous morphology (Chapman, 1974; De Hon, 1992; Newsom et al., 1996; Cabrol and Grin, 1999, 2002). They are characterized by a flat floor and by the presence of inner landforms, often interpreted as a result of volcanic filling or sedimentary deposition. These anomalous impact craters are essentially located in the Noachian highlands, dated to >3.7 Ga (Tanaka, 1986; Hartmann and Neukum, 2001; Hartmann, 2005), and their degraded rims and internal fillings have been interpreted as due to the effects of deposition followed by strong erosion on Early Mars (Tanaka, 1986; Craddock and Maxwell, 1993; Golombek and Bridges, 2000; Craddock and Howard, 2002), under a surface environment different

\* Corresponding author. Laboratoire de Planétologie et Géodynamique de Nantes, Université de Nantes/CNRS UMR6112, 2 rue de la Houssinière, BP 92208, 44322 Nantes, France.

E-mail address: [veronique.ansan@univ-nantes.fr](mailto:veronique.ansan@univ-nantes.fr) (V. Ansan).

than the one seen at present. Indeed, lunar craters modified by 3.7 Ga of meteoritic and volcanic activity do not display the same shape as ancient martian craters. Despite the low spatial resolution in Viking images, some of these impact craters were interpreted as paleolakes on the basis of the presence of alluvial fans, deltas, sedimentary terraces, or shorelines (e.g., De Hon, 1992; Lucchitta et al., 1992; Scott et al., 1995; Newsom et al., 1996; Grin and Cabrol, 1997; Zimbleman, 1998; Cabrol and Grin, 1999, 2000, 2002; Ansan and Mangold, 2004). These types of observations have been found in parallel to those seen for large valley networks that incise the Noachian highlands (e.g., Milton, 1973; Baker and Kochel, 1979; Pieri, 1980; Carr and Clow, 1981; Mars Channel Working Group, 1983; Howard, 1988; Gulick and Baker, 1989; Baker et al., 1992; Carr, 1996; Grant, 2000; Gulick, 2001; Irwin and Howard, 2002; Howard et al., 2005; Irwin et al., 2005; Ansan and Mangold, 2006; Ansan et al., 2008). Such interpretations have been locally confirmed by post-Viking data in several craters (e.g., Malin and Edgett, 2000, 2003; Ori et al., 2000; Moore and Howard, 2005; Fassett and Head, 2005; Pondrelli et al., 2005, 2008; Mangold and Ansan, 2006; Grant et al., 2008; Hauber et al., 2009). However, the frequency of such craters at the surface of Mars and the duration of the sedimentary activity related to their filling are still a matter of debate.

Sedimentary features associated with craters as alluvial fans or deltas are mainly identified by their topography and fan shape (e.g., De Hon, 1992; Ori et al., 2000; Moore and Howard, 2005; Mangold and Ansan, 2006; Pondrelli et al., 2008; Metz et al., 2009a). The presence of light-toned layered material (e.g., Tanaka, 1999; Edgett and Malin, 2002; Malin and Edgett, 2003; Moore et al., 2003; Ansan and Mangold, 2004; Ansan et al., 2006; Lewis and Aharonson, 2006; Wilson et al., 2007), or of hydrated minerals such as those found recently by near infrared spectrometers (Poulet et al., 2005; Ansan et al., 2005; Mangold et al., 2007; Milliken et al., 2007; Murchie et al., 2007; Mustard et al., 2008; Ehlmann et al., 2008; Milliken and Bish, 2010) can help with interpretations. However, the evidence for sub-aqueous deposition is often uncertain, especially in the case of the partial preservation of fan shape. Only a detailed geometric analysis for sediment structure (as well as the context of deposition) can demonstrate an aqueous origin.

Here, the geology of the large anomalous Terby impact crater, located north of the Hellas basin, is revisited (Fig. 1). A thick assemblage of light-toned layered material was observed inside this crater (e.g. Ansan and Mangold, 2004; Wilson et al., 2007), and a geometric analysis of these layers was determined using visible images acquired by the High Resolution Stereo Camera (HRSC) on board the Mars Express orbiter (Chicarro et al., 2004; Neukum et al., 2004; Jaumann et al., 2007). The dataset allowed us to calculate a Digital Elevation Model (DEM) in the central N–S strip of the Terby impact crater using a spatial sampling of 15 m. The mineralogy of light-toned layered deposits was analyzed using the “Observatoire pour la Minéralogie, l’Eau, les Glaces et l’Activité” (OMEGA) spectrometer at a 300 m to 2 km spatial sampling (Bibring et al., 2004), and by the “Compact Reconnaissance Imaging Spectrometer for Mars” (CRISM) spectrometer at 20 m for spatial sampling (Murchie et al., 2007). Additional available datasets were also utilized, including altimetry acquired by the Mars Orbiter Laser Altimeter (MOLA) (Smith et al., 1999), Thermal Emission System (TES) data for thermal inertia (Christensen et al., 2001), Thermal Emission Imaging System (THEMIS) images (Christensen et al., 2003), Mars Orbiter Camera (MOC) images (Malin et al., 1998), and High Resolution Imaging Science Experiment (HiRISE) images (McEwen et al., 2007).

## 2. Geological setting

The 174 km diameter Terby impact crater (28.0°S–74.1°E) is located on the northern rim of the Hellas basin (Fig. 1). From a geologic point of view, the area is very interesting since it displays

both flat floor impact craters and light-toned layered deposits (Malin and Edgett, 2000), as well as periglacial and glacial features, e.g. lobate aprons, debris aprons, ice-rich viscous flow, and glacial tongues (Squyres, 1989; Crown et al., 1992; Baratoux et al., 2002; Mangold, 2003; Milliken et al., 2003; Pierce and Crown, 2003) that likely formed during the Amazonian period as a consequence of snowfalls during high obliquity (Forget et al., 2006). These features have been identified within the Terby impact crater as glacial viscous flows in the northwest, and as possible eskers on the floor of the closed depression (Wilson et al., 2007). Therefore, the Terby impact crater has recorded many episodes of geologic and climatic history for Mars. Unfortunately, this area is often difficult to observe from orbiters since it is frequently shielded by dust storms, clouds, and frost deposition in winter (Martin, 1974; Peterfreund and Kieffer, 1979; Zurek, 1982; Mckim, 1996; Cantor, 2007).

The Terby impact crater is believed to have formed during the Early to Middle Noachian (Tanaka, 1986; Leonard and Tanaka, 2001; Werner, 2008), and includes younger materials such as undifferentiated mantle deposits of an uncertain origin (Leonard and Tanaka, 2001). The Terby crater has an anomalous inner flat morphology without obvious sedimentary or erosional landforms (fans, terraces, shorelines, etc.), at the ~200 m Viking scale. The rim is heavily degraded, the result of intense aeolian and fluvial erosion, interpreted as due to an early, relatively thick atmosphere with a warm climate, or as a result of hydrothermal activity (Brakenridge et al., 1985; Craddock and Maxwell, 1993; Tanaka et al., 1998; Craddock and Howard, 2002). The northern inner part shows an interesting dissected relief standing above the southern inner flat area, and is marked by pits and irregular depressions. The material filling the crater has been interpreted as friable aeolian, fluvial, and possibly volcanic air-fall deposits, or possibly, ice-cemented locally, dating to the boundary of the Noachian and Hesperian periods as determined from Viking data (Leonard and Tanaka, 2001).

MOLA altimetry shows that the inner impact rim stands at an elevation of –3000 m for the lowest section and that it is ~1 km high on average (Fig. 1b). The northwestern border of the Terby impact rim is interrupted by a 22 km diameter impact crater, while the northeastern border is characterized by relatively flat terrain standing at an elevation of –1 km. The southern impact rim is cut by a 50 km diameter, relatively fresh, complex impact crater with a central peak (C in Fig. 1). The Terby impact crater displays a flat interior in the central and southern parts, stands at –4500 m (Fig. 1b), and covers a surface of ~17,500 km<sup>2</sup>.

To the north, the flat interior is carved by two closed depressions (Dw and Dc) of ~500 m in depth, separated by three mesas (M1, M2, and M3, as seen in Fig. 1). The northern M1 and M2 mesas are disconnected from the flat inner area, whereas the M3 mesa is linked to it. The mesas display an increase in elevation from –4000 m in the eastern part to –2000 m in the western part, and have a maximum relief of 3 km above the bottom of the closed-depression Dw (Fig. 1c). The mean width is 25 km and the length is ~60 km (Fig. 1c and d). Mesa tops have a gentle slope of ~1° to the south (Fig. 1c). At the MOC scale, mesa sides show many layers <10 m in thickness that accumulate up to 2.5 km in thickness for the mesa M1 (Malin and Edgett, 2000; Ansan and Mangold, 2004; Ansan et al., 2005, 2006; Wilson et al., 2007). Thermal infrared data (TES and THEMIS) show that the interior of the Terby impact crater is mainly covered by a low inertia mantle (intermediate gray tone in Figs. 1e and 2a, due to their ability to lose heat stored during the day at night). On the contrary, mesa sides display bright areas at night (Fig. 2a) that consist of more indurated rock, due to their ability to keep day-time heat.

Determining the nature and origin of layered materials was the main goal of this study. We sought to answer several questions. Would layer geometry provide information regarding formation

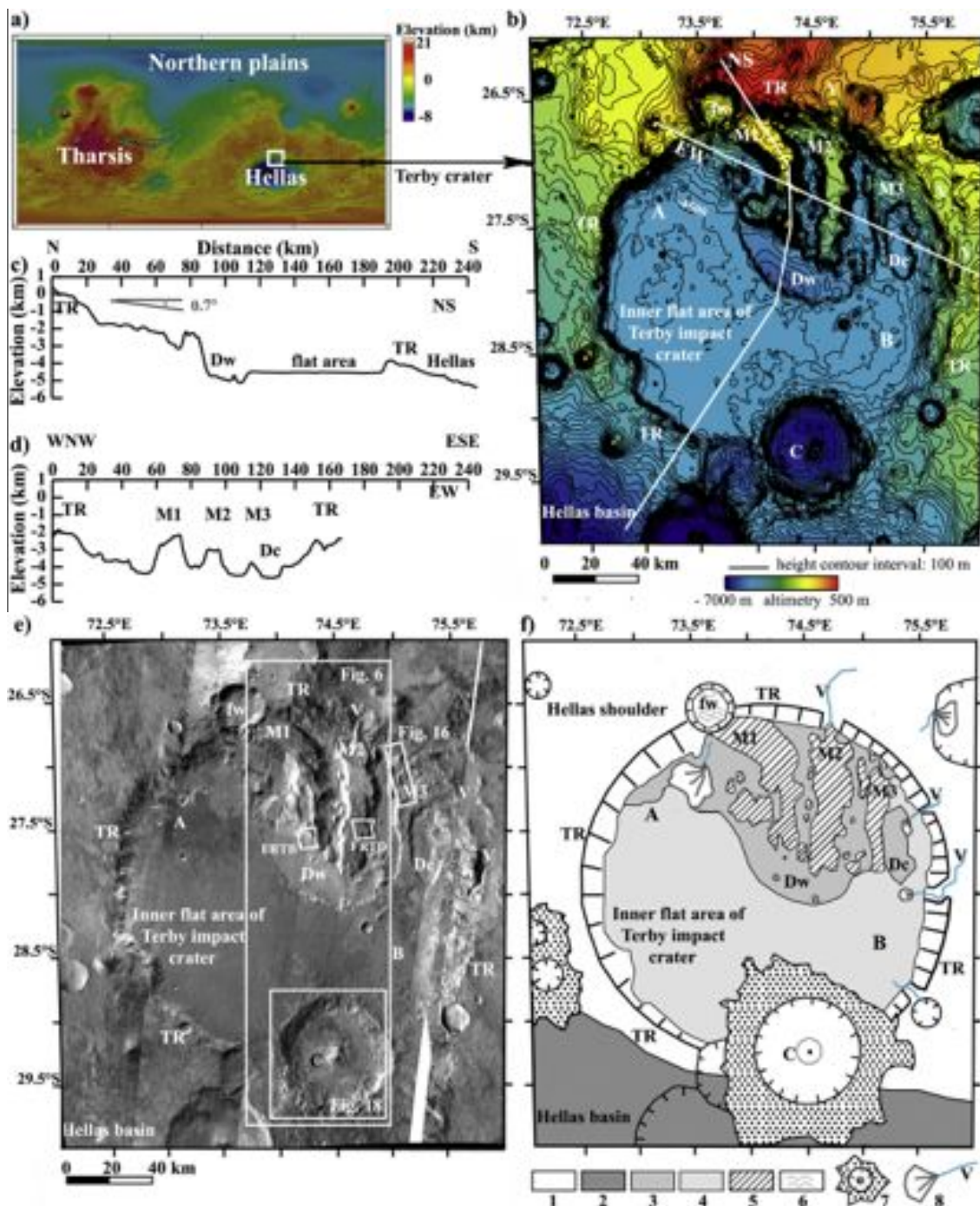


**Fig. 1.** (a) Location of Terby impact crater to the north of Hellas Basin (white box) on the MOLA altimetry map (Smith et al., 1999). (b) MOLA topography of Terby impact crater with height contour lines with 100 m spacing in sinusoidal projection centered at 75°E of longitude. The 174 km diameter Terby impact crater has a 5.5 km deep relief between its rim and its lowest northern area. The flat inner Terby impact crater stands at -4 km in elevation, except in its northern area where closed depressions border high flat appendices named mesas. White lines, labeled NS and EW, correspond to the location of topographic profiles. TR: Terby impact crater rim. Dw: closed W-shaped depression. Dc: closed oval depression. M1, M2 and M3: the three mesas. V: fluvial valley. fw: viscous flow features. A, B and C are the locations of high TES thermal inertia ( $>650 \text{ J m}^{-2} \text{ K}^{-1} \text{ s}^{-0.5}$ ). (c) N-S topographic profile. (d) E-W topographic profile. (e) Mosaic of 19 day-time IR THEMIS images (106452002, 108287002, 108961002, 107900003, 105316002, 107176002, 102657003, 107151005, 102295002, 107126002, 107850004, 106377002, 107101002, 109510003, 107438002, 107825005, 106714002, 109485003 and 107076002), on which are overlaid the location of CRISM data (FRTB corresponding to the FRT000622B image and FRTD to the FRT00084D6 image), and (f) Context map of Terby area: 1. Hellas shoulder, 2. Hellas basin, 3. Closed depression in the floor of Terby impact crater, 4. Inner flat area of Terby impact crater, 5. Layered terrain of mesas labeled M1, M2 and M3, 6. Viscous flow, 7. Impact crater with peak, rim and ejecta, and 8. Valley V and alluvial fan.

processes? What is the mineralogy of these layers? Is the filling volcanic or sedimentary? If sedimentary, by which geological processes did they form: by subaerial or sub-aqueous deposition? Hereafter, the data and their processing are presented along with

details for the spectral analyses. We then describe the geometry and mineralogy of inner filling in the Terby impact crater. Finally, the geologic environment and the temporal succession as determined by our analyses are discussed.

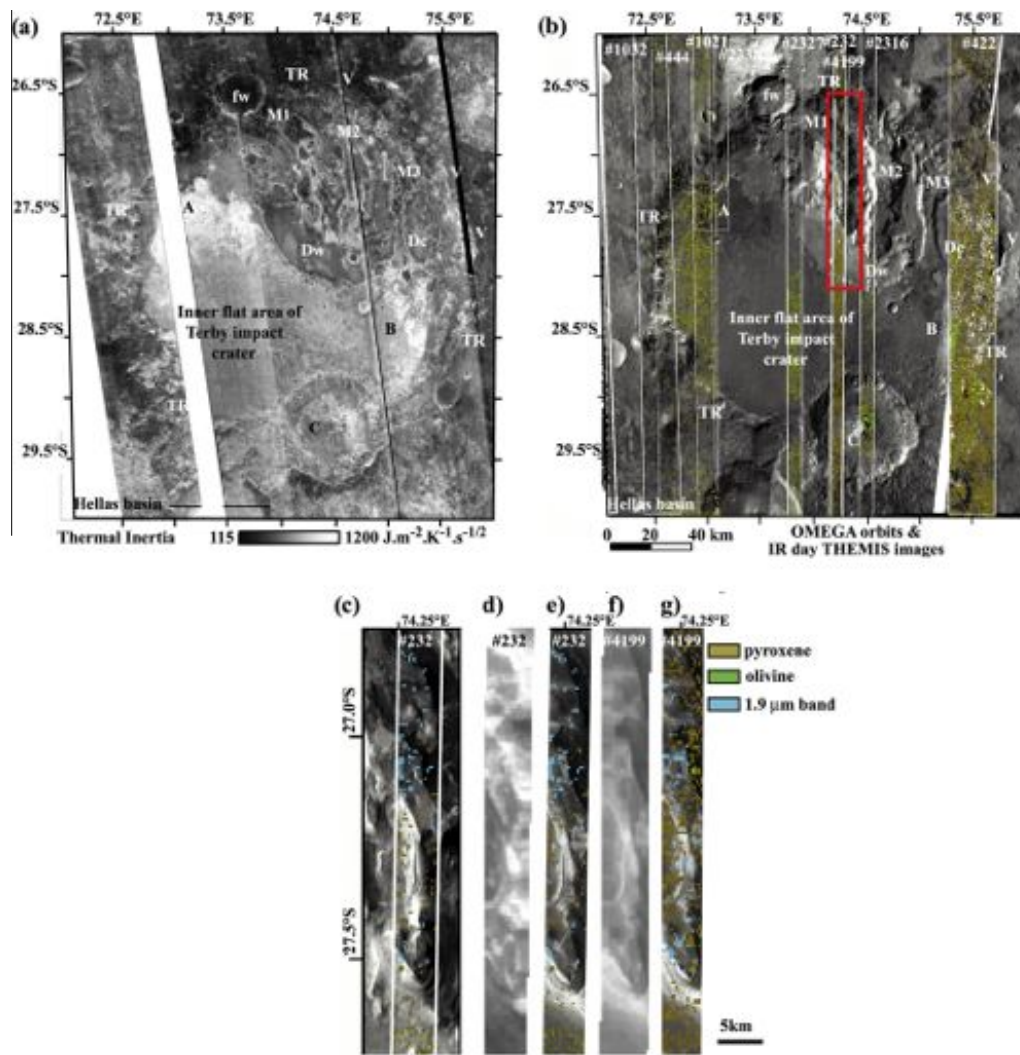


**Fig. 2.** (a) Mosaic of day-time IR THEMIS image and (b) mosaic of 12 night-time IR THEMIS images (I01215006, I01939005, I02301004, I03437003, I05247010, I05272009, I05634012, I05996006, I05659012, I05684012, I06358011 and I06383006). THEMIS images have a resolution of  $\sim 100$  m pixel<sup>-1</sup>. The labels correspond to those used in Fig. 1. (b) Location of the OMEGA orbits overlaid on the IR day-time THEMIS images of the Terby impact crater. Map of the different absorption bands associated to mineral families (pyroxenes, olivine and hydrated minerals) is superimposed on the figure. The red box focuses on the mesa M1. (c) Detailed view on the mesa M1, showing the mineral families detected in the orbit #232 overlapping the IR night-time THEMIS images. (d) Albedo reflectance at 1  $\mu$ m of the OMEGA orbit #232 (sun illumination from NE). (e) Mineral families detected in the OMEGA orbit #232 superimposed on the HRSC image. (f) Albedo reflectance at 1  $\mu$ m of the OMEGA orbit #4199 (sun illumination from NW). (g) Mineral families detected in the OMEGA orbit #4199 superimposed on the HRSC image. (For interpretation of the references to color in this figure legend, the reader is referred to the web version of this article.)

### 3. Data and processing

In this study, we used both near-infrared and thermal infrared data, and visible images, which characteristics are detailed below.

#### 3.1. OMEGA spectral data

OMEGA is a visible and near-infrared (VNIR) hyperspectral imager that provides three-dimensional data cubes with spatial samplings from a few kilometers to 300 m. For each pixel a spectrum between 0.35 and 5.1  $\mu$ m is determined using 352 contiguous spectral elements (spectels) of 7–20 nm in width. The spectrometer consists of three overlapping detectors (from 0.35 to 1  $\mu$ m, from 0.9 to 2.7  $\mu$ m, and from 2.5 to 5.1  $\mu$ m) (Bibring et al., 2004). Our study utilized data recorded by the second detector, for which the wavelength domain was well calibrated, was dominated by solar reflection, and that enabled the identification of many minerals (Bibring et al., 2005).

Data processing first took into account the modular transfer function for each spectral element, the solar spectrum, and absorption due to the atmosphere (by assuming a power law variation of CO<sub>2</sub> absorption with altitude). The output spectra equivalent to the apparent I/F reflectance (the flux received by the detector from the surface of Mars divided by the solar flux at the martian distance) can be utilized to retrieve the presence of minerals on the surface by studying absorption bands. The analysis was based on an estimation of the band depths of characteristic absorption bands within the 0.9–2.7  $\mu$ m domain. We calculated the spectral index of these bands as determined in Table 1 which lead to the determination of some minerals or groups of minerals located within the top hundreds of micrometers of the surface. One issue with the interpretation is the likely mixing of minerals, because several minerals compose rocks while each spectrum corresponds to a large area (at least 300 m  $\times$  300 m). However, spectral features can confidently be utilized to map mineral diversity on the martian surface (Bibring et al., 2005).

**Table 1**  
Spectral characteristics of mineral families detected by OMEGA in the Terby impact crater.

Candidate minerals	Characteristic absorption band center ( $\mu\text{m}$ )	Spectral index	USGS spectral library	Detection threshold
Olivine	1.03–1.05	$R(1.56)/(0.1 * R(1.01) + 0.2 * R(1.21) + 0.7 * R(1.33))$	Olivine GDS70.a $\text{Mg}_2\text{SiO}_4\text{--Fe}_2\text{SiO}_4\text{Fo}_{89}$	1.03
HCP (clino-pyroxene)	2.2	$1 - (R(2.15) + R(2.20))/(R(1.81) + R(2.50))$	Augite NMNH120049 (Ca,Mg,Fe) $_2$ (Si,Al) $_2$ O $_6$	1%
Hydrous minerals	1.93	$1 - (R(1.93) + R(1.94))/(R(1.80) + R(2.12))$		2%
Fe-OH or Mg-OH smectites	2.30 (along with 1.93)	$1 - R(2.30)/(0.25 * R(2.26) + 0.25 * R(2.27) + 0.5 * R(2.34))$	Nontronite NG-1.a $\text{Na}_{0.3}\text{Fe}_2^{3+}(\text{Si}, \text{Al})_4\text{O}_{10}(\text{OH})_2 \cdot n\text{H}_2\text{O}$	2%

R is the reflectance I/F at the given wavelength in  $\mu\text{m}$ .

Dust storms can partially or completely obscure the surface from orbital view (Akabane et al., 1992; Cantor, 2007), as occurred periodically during the first three years of the Mars Express mission. As a consequence, several OMEGA orbital strips covering the Terby impact crater were not usable. However, several orbits had a good enough signal with which to extract mineralogy (Fig. 2b) at different spatial sampling: two orbits at a medium resolution ( $\sim 500$  m pixel $^{-1}$ , 64 pixel large band, orbit: #0422, #0444), and seven orbits at a high resolution ( $\sim 300$  m pixel $^{-1}$ , 16 pixel narrow bands: orbits #0232, #1021, #1032, #2316, #2327, #2338, #4199). Orbits #0232 and #4199 were exactly overlapping, enabling cross-validation despite different illumination conditions (the data were recorded at different local times during the southern summer, Fig. 2d and f).

Three families of minerals were identified in the Terby impact crater (Figs. 2 and 3):

- (i) Absorptions due to iron between 0.8 and 1.5  $\mu\text{m}$  typical of olivine (Fig. 3a, e.g. laboratory spectrum of forsterite, Clark et al., 1993). These absorption bands are deep and broad (difference in reflectance  $>0.02$  in Fig. 3a) and may have been caused by olivine of high iron content (i.e., fayalite) or large particle sizes. The OMEGA spectra extracted from orbit #2316 were compared to laboratory olivine spectra. Olivine-bearing areas in the Terby impact crater were mapped (Fig. 2b) using a calculation for the spectral index of the broad band related to a positive slope between 1.0  $\mu\text{m}$  and 1.56  $\mu\text{m}$  (Table 1). A detection threshold of 1.03 was chosen to ensure that no pixel showed the presence of olivine due to instrument noise alone, without discarding pixels with true low detection.
- (ii) Two broad absorption bands centered at  $\sim 1.0$  and  $\sim 2.2$   $\mu\text{m}$  revealed the presence of pyroxenes. The position of the centers of these bands varied with calcium content in pyroxene. For a high calcium pyroxene (HCP), the centers are at  $\sim 1.05$  and  $\sim 2.30$   $\mu\text{m}$ , and for low calcium pyroxene (LCP) at  $\sim 0.9$  and  $\sim 1.8$   $\mu\text{m}$ . The most abundant type was the high calcium pyroxenes, as shown by the OMEGA spectral ratio compared to laboratory spectra (Fig. 3b). Pyroxene-rich areas in the Terby impact crater were mapped (Fig. 2b) using the calculation of the spectral index of the broad  $\sim 2.2$   $\mu\text{m}$  band (Table 1). A detection threshold of 1% was enough to discard most falsely detected pixels (Poulet et al., 2007).
- (iii) A narrow absorption band centered at 1.93  $\mu\text{m}$  (Fig. 3c) for orbits #232 and #4199 indicated the presence of hydrated minerals (Fig. 2b–f). The 1.93  $\mu\text{m}$  band is due to a combination of the H–O–H bend,  $\nu_2$  at  $\sim 6.1$   $\mu\text{m}$ , and a symmetric OH stretch,  $\nu_3$  at  $\sim 2.9$   $\mu\text{m}$  (Clark et al., 1990). This absorption band was weak in OMEGA data, just above the detection threshold, that were fixed at 2% (also see Poulet et al., 2007). Detection was coherent between the two orbits acquired under conditions of opposite illumination (Fig. 2d and f) even though a few points were not found exactly at

the same location, possibly due to differences in an illumination condition or due to detection close to the minimum threshold. For many of the pixels showing this absorption band, the spectrum was also marked by a narrow shallow absorption band centered at  $\sim 2.3$   $\mu\text{m}$ . This band is generally caused by either Fe–OH (at 2.29  $\mu\text{m}$ ) or Mg–OH ( $>2.32$   $\mu\text{m}$ ), or to a mixing of the two (Clark et al., 1990; Poulet et al., 2005) although weakness in the absorption band would not allow us to discriminate between the two. Thanks to a combination of the two narrow absorption bands at 1.93  $\mu\text{m}$  and 2.30  $\mu\text{m}$ , we favor the family of hydrated phyllosilicates with Fe/Mg-rich smectites, such as nontronite or/and saponite, as best fit (Fig. 3c). The lack of a band at 1.41  $\mu\text{m}$ , for these minerals, was likely due to an instrumental deficiency and/or to the coating effect, with a dead spectral element appearing at 1.414  $\mu\text{m}$  after orbit 171 (Poulet et al., 2008).

Several spectra also displayed a single 1.93 or 2.30  $\mu\text{m}$  band. The first type can be attributed to undetermined hydrated minerals whose nature could not be discriminated. The second type, with a single Fe–OH band, is difficult to connect to a specific mineral. Nevertheless, it may indicate the presence of hydrated silicates such as smectites with a reduced H $_2$ O band at 1.93  $\mu\text{m}$ , due to desiccation (by heating or atmospheric desiccation) as observed experimentally (Milliken and Mustard, 2005). Small absorption features that were close to the detection limit might also be due limited spatial resolution, inducing a mixing with more neutral components. The issue can be solved locally using CRISM data.

### 3.2. CRISM spectral data

CRISM is a visible and near-infrared (VNIR) hyperspectral imager that measures reflected sun-light from 0.362 to 3.920  $\mu\text{m}$  at 6.55 nm per channel, providing three-dimensional data cubes with spatial samplings from a few 100 m to 18 m (Murchie et al., 2007). We used two full spatial (20 m pixel $^{-1}$ ) and spectral images (FRT0000622B and FRT000084D6, Fig. 4) acquired in 2007 (day 159 for FRT0000622B and day 292 for FRT000084D6). The spectra are located in the southern section of mesa M1 and on the eastern side of mesa M2, respectively (Fig. 1e).

CRISM frames were calibrated to atmospherically-removed reflectance using data processing as described in Murchie et al. (2009). Many CRISM spectra showed a narrow absorption band centered at 1.41  $\mu\text{m}$  associated with a weak absorption band at 1.93  $\mu\text{m}$ , and a feature at  $\sim 2.3$   $\mu\text{m}$  indicative of the presence of hydrated minerals (Fig. 5). The absorption band at 1.93  $\mu\text{m}$  was not obvious in the reflectance spectra probably because it occurs in a region of the spectra where strong atmospheric signatures are present and the signal is weak. The signature was unambiguously revealed using a technique of spectral ratio (Fig. 5a), which consists of a ratio of the observed spectrum to that of a spectrally neutral region with a similar atmospheric path length acquired during

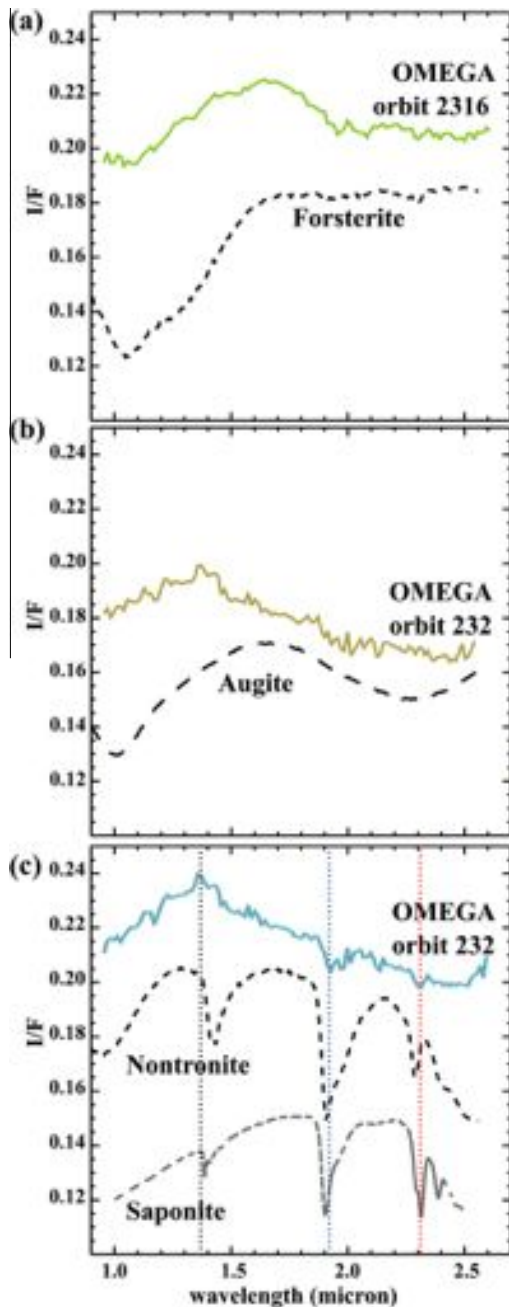


**Fig. 3.** Three characteristic OMEGA spectra of each mineral family are presented and compared to mineral laboratory spectra (dashed line) that are shifted for clarity. The latter have not the same I/F reflectance scale as the OMEGA spectra, but we can compare their shape and absorption bands with the OMEGA ones: (a) olivine (laboratory spectrum: forsterite type, olivine GDS70.a, USGS spectral library, Clark et al., 1993), (b) pyroxene (laboratory spectrum, HCP, here Augite NMNH120049, USGS spectral library, Clark et al., 1993), and (c) phyllosilicate spectra (laboratory spectra: nontronite NG-1.a, USGS spectral library, Clark et al., 1993, and saponite c1sa53, CRISM-RELAB spectral library, <http://pdsgeosciences.wustl.edu/MROCRISMSpectralLibrary/>). Vertical dotted lines correspond respectively to 1.41  $\mu\text{m}$  (black), 1.93  $\mu\text{m}$  (blue) and 2.30  $\mu\text{m}$  (red). (For interpretation of the references to color in this figure legend, the reader is referred to the web version of this article.)

the same observation sequence. Some of spectra showed an additional broad shallow absorption band at  $\sim 2.30 \mu\text{m}$ , indicative of Fe-OH and/or Mg-OH bonds (Fig. 5b), and the observations confirm detections made with OMEGA at a lower spatial resolution. Because of the combination of the three absorption bands at 1.41, 1.93, and 2.30  $\mu\text{m}$ , we favor, as for OMEGA data, the family of hy-

drated phyllosilicates, and specifically the Fe/Mg-rich phyllosilicates such as nontronite and saponite, or possibly vermiculite (Fig. 5c), this latter mineral fitting less precisely CRISM spectra.

The spatial distribution of the 1.93 and 2.30  $\mu\text{m}$  features shown in Fig. 4 were mapped using the spectral parameters defined in Table 2. The maps were derived from cubes filtered spectrally by a window of three spectral elements and then continuum-removed. The maps have a threshold at 0.7% and 0.9% for the 1.93  $\mu\text{m}$  and 2.30  $\mu\text{m}$  features, respectively. The thresholds allow the removal of most of the noise in the spectrum. The maps were then filtered to remove residual streaks and noise. The 1.93 and 2.30  $\mu\text{m}$  spectral parameters were spatially correlated, which is an indication of the presence of Fe–Mg phyllosilicates. Note, however, that only a few areas displayed single 1.93  $\mu\text{m}$  bands such as those on the toe of the mesa M1 as shown by the arrow in Fig. 4. These hydrated minerals could correspond to sulfates, or possibly zeolites (Carter et al., 2010).

### 3.3. HRSC image and HRSC DEM

The Terby impact crater was imaged in both nadir (Fig. 6) and stereo modes by the High Resolution Stereoscopic Camera (HRSC) (Neukum et al., 2004; Jaumann et al., 2007), with a high spatial resolution of 11.9 m  $\text{pixel}^{-1}$  at the center of nadir image located at 25.17°S and 74.32°E (orbit #4199). Panchromatic images are located on the central meridian part of the Terby impact crater. Several sections of these images appear blurred and without contrast since they were acquired in periods of active dust storm activity. A dust storm is visible at the south of the flat plateau near the small impact crater C (Fig. 6a). Despite atmospheric effects, the mesas were not touched by this strong opacity and layers on scarps are well visible (Fig. 6b).

We generated the HRSC DEM (Fig. 6c and d) using photogrammetric software developed both at the Deutsches Zentrum für Luft- und Raumfahrt (DLR) and at the Technical University of Berlin (Scholten et al., 2005; Albertz et al., 2005; Gwinner et al., 2007). The height was calculated while taking into account the martian geoid defined as the topographic reference for martian heights (i.e. areoid, Smith, 1999) with a height accuracy  $<20 \text{ m}$  (Ansan et al., 2008). Since the quality of the HRSC DEMs strongly depends on the acquisition geometry of the triplet of images that controls their spatial resolution, the image quality (compression ratio, aerosols, etc.), and the surface roughness, that of Terby impact crater was very good (Fig. 6c) in regards to spatial gridding (15 m  $\text{pixel}^{-1}$ ) and topography accuracy on rough surfaces like mesas sides. A total of 3,000,815 homologous points were detected between 26°S and 28.5°S in latitude, using 3D coordinates that have a relatively good spatial accuracy ( $\sigma_x = 2.87 \text{ m}$ ,  $\sigma_y = 7.14 \text{ m}$  and  $\sigma_z = 4.39 \text{ m}$ ), implying a statistical height error of 6.11 m for each point. Unfortunately, the topography of closed depressions Dw and Dc and the inner flat area of the Terby impact crater was poorly determined due to the poor detection of homologous points on the smooth surface.

### 3.4. Thermal infrared imagery and high resolution visible images

For the regional view of Terby crater, we used 19 day-time thermal infrared THEMIS images (Fig. 1e) and 12 night-time thermal infrared THEMIS images having a resolution of  $\sim 100 \text{ m pixel}^{-1}$  (Fig. 2a) allowing us to identify morpho-structural units and determine their thermal properties. In order to obtain more details for this area, 63 visible THEMIS images at a spatial resolution of 17 m  $\text{pixel}^{-1}$  were utilized. The images mainly covered the northern inner part of the Terby impact crater. In addition, 89 MOC narrow angle images with the resolution ranging from 1.5 m to 6 m  $\text{pixel}^{-1}$  were used, and partially covered the northern part of

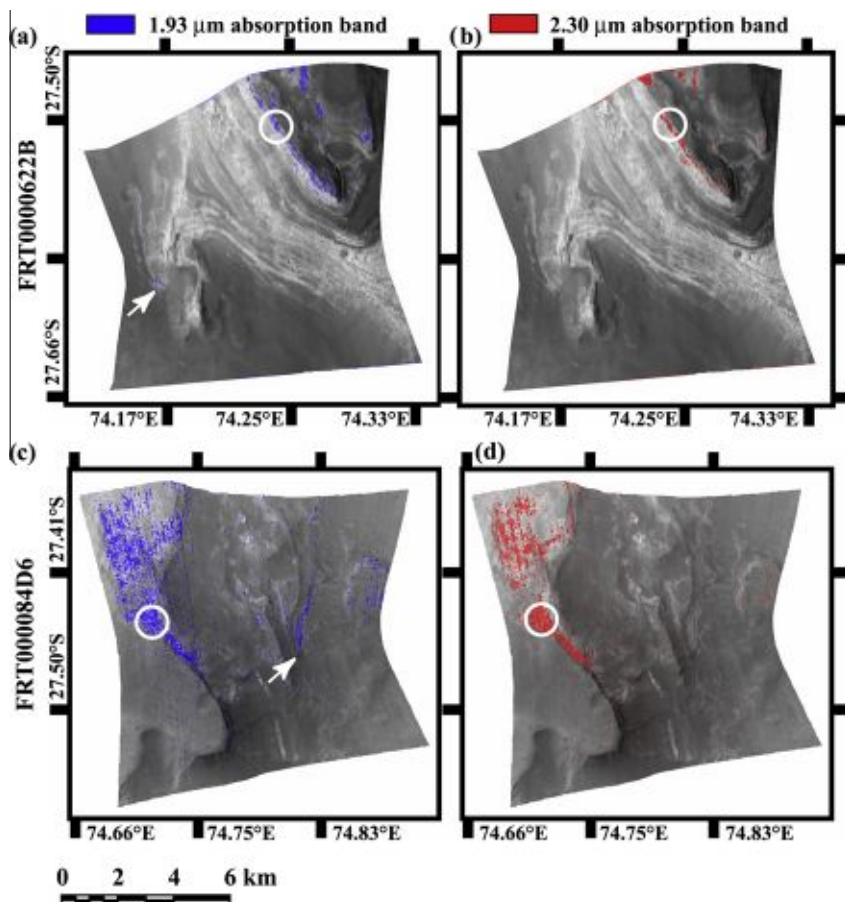


**Fig. 4.** Two CRISM full resolution targets ( $18 \text{ m pixel}^{-1}$ ), located on the end of mesa M1 (FRT00006222B, see FRTB in Fig. 1e for context) and the eastern side of mesa M2 (FRT000084D6, see FRTD in Fig. 1e for context). For each target, the  $1.93 \mu\text{m}$  (blue, a and c) and  $2.30 \mu\text{m}$  (red, b and d) absorption bands depth maps are superimposed on the CRISM albedo image at  $1 \mu\text{m}$ . On each target, circles correspond to the locations where reflectance spectra are extracted in Fig. 5, and arrows indicate undetermined hydrated minerals detected at the toe of the mesas. (For interpretation of the references to color in this figure legend, the reader is referred to the web version of this article.)

the Terby impact crater. The High Resolution Imaging Science Experiment (HiRISE) of the Mars Reconnaissance Orbiter mission (McEwen et al., 2007) delivered 13 images for the northern part of the Terby impact crater at the time of this study. The instrument can offer images with a spatial resolution of  $25 \text{ cm pixel}^{-1}$ , permitting a detailed study of outcrop geometry.

### 3.5. Mapping and quantitative geometry of layers

All previously cited data were ortho-rectified on the martian ellipsoid, using an equatorial axis of 3396.19 km and a polar axis of 3376.20 km as defined by the International Astronomical Union as the Mars IAU 2000 (Seidelmann et al., 2002), with a sinusoidal projection centered at the  $75^\circ\text{E}$  meridian. The geographic coordinates followed the martian standard coordinate system – with planetocentric latitudes and east longitudes (Duxbury et al., 2002). All of the datasets were then included in a Geographic Information System (GIS).

Based on a detailed topography for the central part of the Terby impact crater, the geomorphology and the geology of the Terby crater was studied by superimposing visible images (HRSC, MOC and HiRISE) on the HRSC DEM (Fig. 6d). We studied in details the layered terrains inside Terby crater, in order to determine their nature, genetic processes and depositional environments.

Many layers are exposed along the edge of the landform, and they occur in a wide range of outcrop orientations and elevations. Layers of rocks were traced in various outcrops and examined up to their lateral boundaries. As usually defined on Earth, layers show-

ing the same sedimentary structure and texture compose a rock unit, which likely accumulated under the same environmental conditions or under conditions that were uniformly changing (e.g., Reading, 1996). Although we did not observe the rock texture directly (i.e. grain size and sorting), we deduced some indirect information, in a few places, from their erosional behavior. The contacts, or boundaries, of rock units were defined by major changes in lithology, textures or sedimentary environments, associated with possible erosion surfaces or unconformities. The stratigraphic relationships between rock units were established using the classical Steno's principle (i.e. the younger layer superimposes the older one). Geological cross-sections were then established in which distinct stratigraphic units are plotted.

The geometry of layers (thickness, length, and dip) assumed locally as planar can be determined using the method of the intersection of geologic planar layers with height contour lines and by extraction of three points belonging to this plane. The strike of layer is the clockwise angle from the north determined by the intersection of the plane by a horizontal plane. The dip azimuth is the orthogonal trending to the strike along which the layer is tilted. The dip value is the downward angle between a horizontal plane and the plane of layer. The quantitative measurements of attitude of the layers were computed from the HRSC DEM, with their corresponding error estimates on the basis of statistical uncertainties on the HRSC DEM. The statistical error on strikes and dip azimuths is less  $30^\circ$  and the statistical error on dip values is less than  $2.5^\circ$ . In addition, numerous measurements were done to minimize the uncertainties.

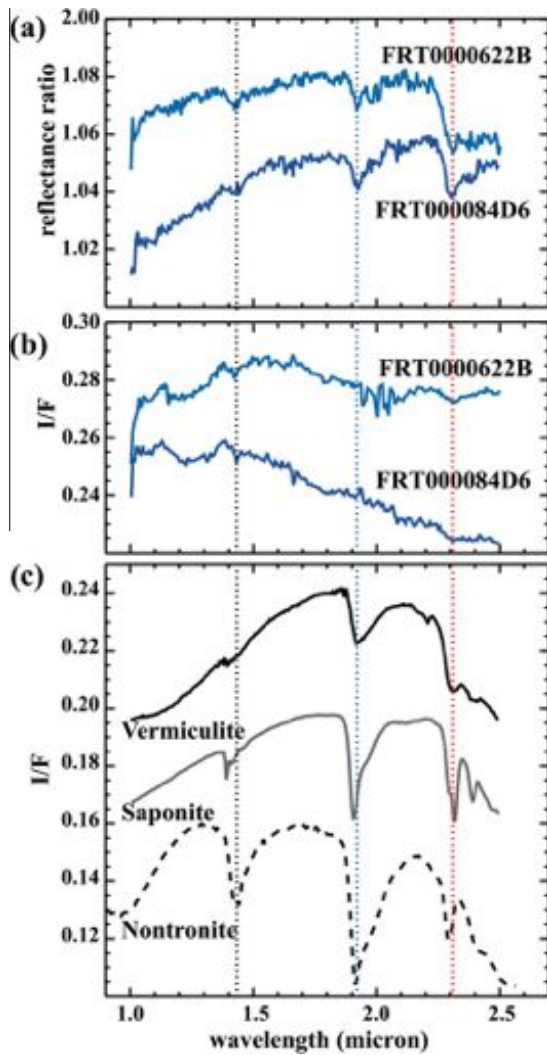


**Fig. 5.** Characteristic CRISM spectra extracted from layered mesa terrains (see location in Fig. 4) indicative of phyllosilicates. Spectra are shifted for clarity: (a) spectral ratios, (b) CRISM spectra, and (c) laboratory spectra of phyllosilicates with offsets for clarity (samples referred to NG-1.a for nontronite, in USGS spectral library, Clark et al., 1993; c1sa53 for saponite and sample cave01 for vermiculite, both in CRISM-RELAB spectral library, <http://pds-geosciences.wustl.edu/MROCRISMSpectralLibrary/>). Vertical dotted lines correspond respectively to 1.41  $\mu\text{m}$  (black), 1.93  $\mu\text{m}$  (blue) and 2.30  $\mu\text{m}$  (red). (For interpretation of the references to color in this figure legend, the reader is referred to the web version of this article.)

In the case where layers are exposed only on scarp without natural topographic curvature, the dip direction and angle of layers

**Table 2**  
Spectral characteristics of mineral families detected by CRISM in the Terby impact crater.

Candidate minerals	Characteristic absorption band center ( $\mu\text{m}$ )	Spectral index	Detection threshold (%)
Hydrous minerals	1.93	Mean ( $BD_{1.92}$ , $BD_{1.93}$ ) with $BD_{1.92} = 1 - R(1.92)/\text{median}[R(1.686), R(1.715), R(1.828)]$ $BD_{1.93} = 1 - R(1.93)/\text{median}[R(1.686), R(1.715), R(1.828)]$	0.7–2
		Median ( $BD_{2.29}$ , $BD_{2.30}$ , $BD_{2.31}$ , $BD_{2.32}$ , $BD_{2.32\text{drop}}$ ) with $BD_{2.29} = 1 - R(2.29)/\text{median}[R(2.205), R(2.246), R(2.395), R(2.408)]$ $BD_{2.30} = 1 - R(2.30)/\text{median}[R(2.205), R(2.246), R(2.395), R(2.408)]$ $BD_{2.31} = 1 - R(2.31)/\text{median}[R(2.205), R(2.246), R(2.395), R(2.408)]$ $BD_{2.32} = 1 - R(2.32)/\text{median}[R(2.205), R(2.246), R(2.395), R(2.408)]$ $BD_{2.32\text{drop}} = 1 - R(2.32)/\text{median}[R(2.150), R(2.164), R(2.205)]$	0.9–2
Fe-OH or Mg-OH smectites	2.30		

$R$  is the filtered and continuum-removed reflectance at the given wavelength in  $\mu\text{m}$ .

were determined along continuous exposed layers in the outcrop plans, corresponding therefore to apparent dips. The apparent dip orientation of layers was assumed orthogonal to layer segment. The given apparent layer dips were representative of a set of layers showing the same apparent geometry outcropping on a minimum area of 200 m in horizontal length  $\times$  5 m in height. We extracted the  $x$ ,  $y$ ,  $z$  coordinates of points selected at each continuous layer segment end from the HRSC DEM.

Although the major source of uncertainty in these measurements was the location of points chosen by the user, we chose to extract lengths of layer segments ranging from a few hundred meters to over 1 km on visible images so as to minimize the uncertainty. The second source of uncertainty was the high difference in spatial resolution between the HRSC DEM and visible images such as from MOC and HiRISE. However, this was minimized by selecting long (>200 m) layer segments in visible images. The third source of uncertainty was a possible shift between HRSC DEM and visible images, assumed to be lesser than 15 m in  $x$  and  $y$  direction, even if ortho-rectified. The two previous sources of uncertainty could lead to a misinterpretation of layer geometry, especially close to mesa cornices. For these reasons, we determined the layer dips at elevations located >50 m under the mesa summits.

In summary, we measured the apparent dip orientations and angles of >200 m long segments of layers from their  $x$ ,  $y$ ,  $z$  coordinates in the HRSC DEM. For the shortest layer segments (200 m), the dip angle accuracy is  $1.8^\circ$  for an apparent dip of  $1^\circ$ . The dip accuracy decreases down to  $0.3^\circ$  for the same apparent layer dip for exposed layer segments long of 1 km. For this reason, we favored measures on long segments (>500 m).

Finally, we tried to interpret the geological cross-section using sequence stratigraphy methods (Vail, 1987; Posamentier et al., 1988). They are based on lithofacies and sedimentary structure analysis, and recognition of surfaces like unconformities and erosional truncations, interpreted to result of three main factors: (i) tectonics – this factor is absent in the studied area; (ii) water level; and (iii) the sedimentary supply. This point is discussed in part 6.

#### 4. Geology of the Terby impact crater and the geometry of layered material

##### 4.1. Composition of the main geologic units

Near-infrared OMEGA and CRISM orbital data highlight the mineralogical composition of the superficial material within the Terby impact crater (Figs. 2b and 4). The dominant mineral family as detected by the OMEGA spectrometer is composed of pyroxenes present almost everywhere (inner flat area, closed-depression Dw and Dc, and mesas M1, M2, and M3). The pyroxenes distribution was correlated to two types of terrains. Firstly, low night-time

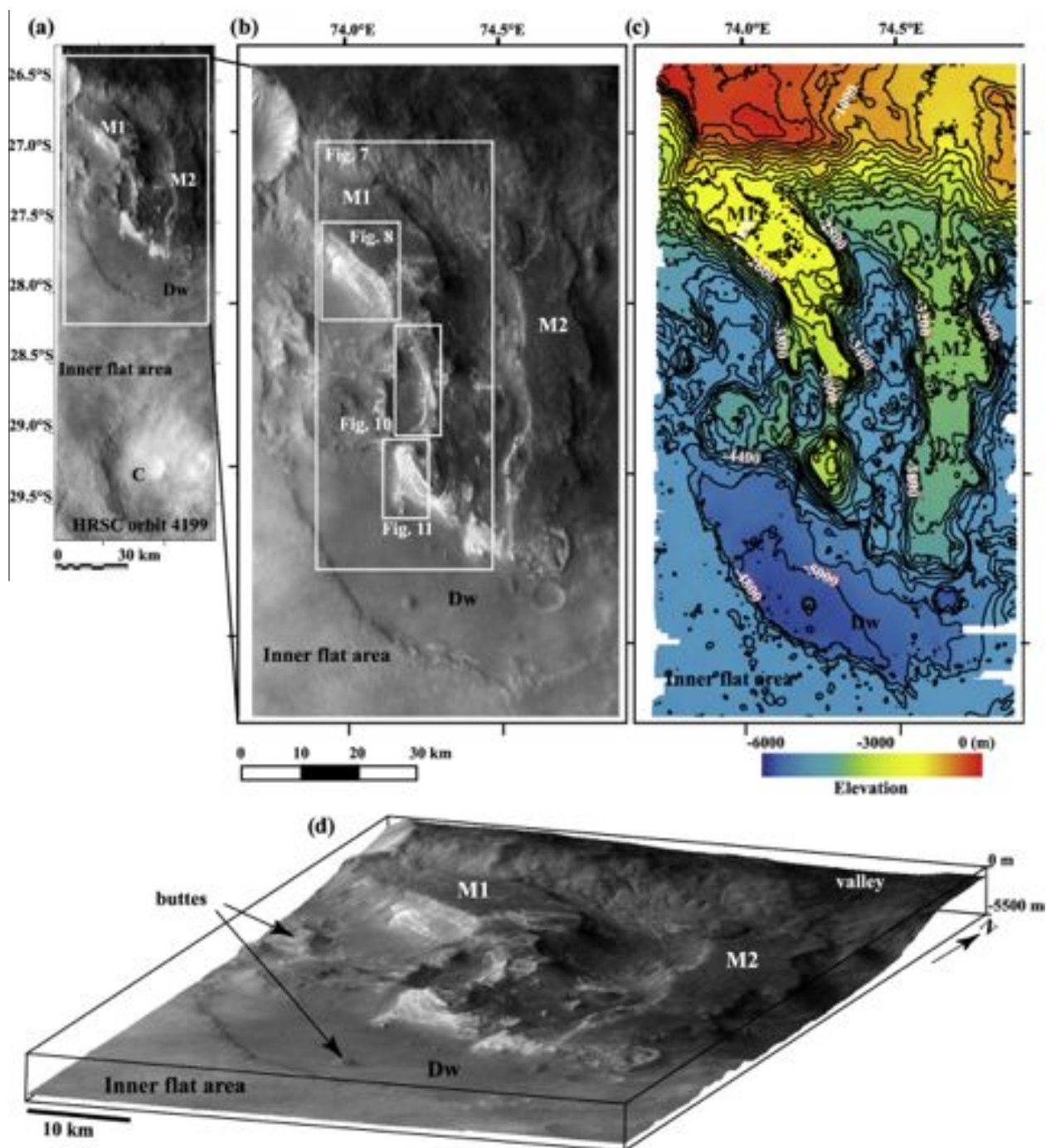


**Fig. 6.** (a) The nadir #4199 HRSC image covers the central part of the Terby impact crater with a spatial resolution of  $15 \text{ m pixel}^{-1}$  (see Fig. 1e for context). Image is projected on Mars ellipsoid with a sinusoidal projection centered at  $75^\circ\text{E}$  of longitude. See the front of dust storm coming from Hellas basin at the south part of image. (b) Zoom on the northern part of the HRSC image showing the detailed geomorphic view of the layered mesas, closed depressions and plateau of the Terby impact crater. (c) The HRSC DEM with spatial grid at  $15 \text{ m pixel}^{-1}$ . The height contours are  $200 \text{ m}$  spaced. (d) 3D view of HRSC #4199 with no vertical exaggeration. Labels as in Fig. 1.

temperature regions contain pyroxenes (dark terrains in Fig. 2a), corresponding to TES thermal inertia ranging from  $<200$  to  $400 \text{ J m}^{-2} \text{ K}^{-1} \text{ s}^{-0.5}$  (Putzig et al., 2005, 2007) suggesting that these pyroxene-bearing regions could be interpreted as either a surface mantled by well-sorted sub-millimeter-scale particles (i.e. sand sized) or indurated fine-grained material (e.g. Jakosky, 1986; Jakosky and Christensen, 1986; Mellon et al., 2000; Putzig et al., 2005). Secondly, the western part A and the eastern part B of the interior plateau contain pyroxenes, correlated with very bright regions in the night-time data (Fig. 2a) and associated with a high TES thermal inertia  $>600 \text{ J m}^{-2} \text{ K}^{-1} \text{ s}^{-0.5}$  (Putzig et al., 2005, 2007). These

regions could correspond to coarse-grained material, or to rocky outcrops (Jakosky and Christensen, 1986; Mellon et al., 2000; Putzig et al., 2005). Therefore, the surface of the interior plateau inside the Terby crater is likely covered by an aeolian mantle mixed with pyroxene-bearing sand dunes visible in high resolution images, except in two regions A and B, where the substratum outcrops.

While the surface is superficially covered by mafic minerals, the mineralogy of the layered terrains in mesas seems different. In fact, two OMEGA swaths, acquired under opposite illumination during the southern summer and spaced by three years, covered the central part of the western mesa M1 (Fig. 2c–g). When correlated with

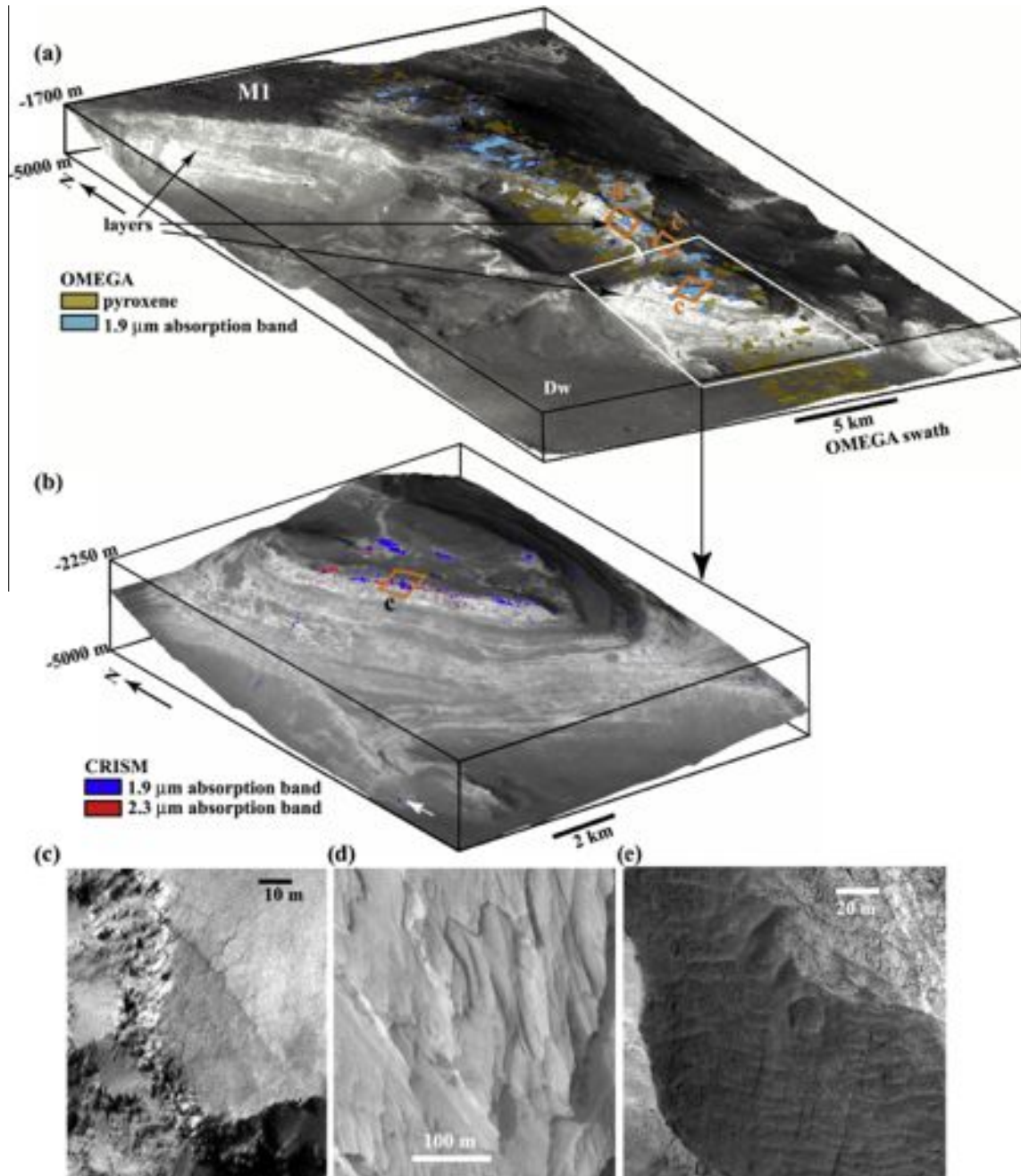


**Fig. 7.** Mesa M1: (a) 3D view of the HRSC image on which OMEGA detections of absorption bands of orbit #232 are overlaid (pyroxenes and  $1.9 \mu\text{m}$  absorption band). See Fig. 6 for context. No vertical exaggeration. Orange boxes indicate the location of HiRISE observations shown at the bottom of figure. (b) Detailed 3D view of the southern end of mesa M1 where detection of CRISM data at  $1.93 \mu\text{m}$  and  $2.30 \mu\text{m}$  absorption bands are superimposed. The white arrow shows the location of hydrated minerals at the bottom of the mesa M1. (c)–(e) Detailed views of geologic features associated to OMEGA and CRISM spectral signatures, observed by HiRISE camera on the mesa M1: (c) a thick fractured layer whose blocks formed boulders accumulated at its toe (PSP\_001662\_1520), (d) ventifacts (aeolian erosive features) in soft thin light-toned layers (PSP\_001595\_1520), and (e) accumulation of pyroxene sand arranged in ripples and dunes at the top light-toned layers (PSP\_001595\_1520). (For interpretation of the references to color in this figure legend, the reader is referred to the web version of this article.)

the HRSC image, pyroxenes were present on the darkest areas at the mesa top or along layer benches (Fig. 2e and g). HiRISE images showed that pyroxenes are present as a dust mantle or as sand-size particles composing dunes (Fig. 7e). Some pyroxenes may be present in mesa layers because they seem present in debris aprons accumulated at the toe of layers, but they have not been detected in layer scarps. In contrast, hydrated minerals detected by the OMEGA spectrometer (Figs. 2 and 7a) were detected over light-toned layers at the top of the mesa M1 ( $-2000 \text{ m}$  to  $-2500 \text{ m}$  in elevation). On the southern side of the mesa (Figs. 4 and 7b), the presence of phyllosilicates was confirmed by CRISM data

(FRT0000622B) where spectral signatures were also located on the top of the mesa M1 ( $-2300 \text{ m}$  to  $-2500 \text{ m}$  in elevation). In addition, phyllosilicates were also detected by CRISM on the summit of the central mesa M2 (Figs. 1 and 4). Undetermined hydrated minerals, possibly sulfate or zeolites (Carter et al., 2010), were punctually detected on the western side of the mesa M1 down to its toe, standing at  $-5000 \text{ m}$  in elevation (arrows in Figs. 4 and 7b).

At the HiRISE scale, hydrated minerals were associated with a succession of layers eroded by wind-driven abrasion (Fig. 7d) implying that the material at the surface is relatively fresh, and to thick fractured layers located at the summit of the southern

end of mesa M1 (Fig. 7c) indicating that the material is relatively indurated and weak enough to split at the meter-scale. In both cases, the observations indicate that phyllosilicates are part of the bulk rock rather than present as a chemical coating or as an aeolian mantle. The amount of hydrated minerals in the layers remains unknown, and does not allow us to discriminate the process of formation of light-toned layers. Determining a detailed geometry of the layers forming the mesas will help us answer this question.

#### 4.2. Detailed study of mesas

The northern part of the Terby impact crater consists of three mesas M1, M2, and M3, separated by W-shaped closed depressions Dw (Fig. 1). At the regional scale (Figs. 1e and 6b), the mesas consist of a succession of predominantly light-toned layered materials exposed by erosion. The material has many repetitive beds that appear to be laterally continuous, indicating that one can identify a given layer in several locations and define its dip, using topographic data. The HRSC nadir image having a good spatial resolution of 15 m pixel<sup>-1</sup> combined with its HRSC DEM at the same spatial resolution (Fig. 6) permitted us to determine the geometry of these layers in detail. MOC and HiRISE images were utilized to complete the geomorphologic and the geologic analysis.

##### 4.2.1. Mesa M1 stratigraphy

**4.2.1.1. Northern section of mesa M1.** The western mesa M1 is the highest mesa with a southward topographic slope of 0.7° (Fig. 1c). In 3D HRSC views of mesa M1 (Figs. 6d and 7), the summit and different parts of its sides were covered by a dark mantle whose low thermal inertia and deposition on slopes as steep as 20° (Fig. 8a) supported the accumulation of wind-blown material subsequent to the erosion of the mesa M1. Beneath the dark mantle, the northwestern side of the mesa M1 displayed a >2500 m thick series of light-toned layers, laterally continuous, and dipping regionally southward (Fig. 8a). The MOC mosaic indicated that layering is expressed by differential erosion that results in alternating benches and scarps with parallel to sub-parallel planar bedding (Fig. 8b). The layers were indurated enough to be eroded in boulders at the scarp toes, forming local debris aprons (Fig. 8b). Although the layers dip gently southward (Fig. 8a), they display variations in apparent dip angles. These layers are divisible into depositional units composed of discrete bundles of geometrically similar strata, bounded by unconformities (Fig. 8c) (see Table A1 for measures of layer attitude).

The HiRISE image PSP\_013160\_1530 (Fig. 9) shows these different stratigraphic units in details. Five stratigraphic units (R0–R5) have been identified based on their erosive features, lithofacies, architecture or sedimentary structures, and their respective stratigraphic position (Fig. 9b and g) (see Table A1 for measures of layer attitude):

- (R0) >500 m of meter-scale thick, light-toned layers showing a regular dip of ~2°S. Layers are usually fractured by two sets of orthogonal fractures spaced of few meters, and mantled by sand dunes (Fig. 9e). They are cratered by <10 m impact craters. Some upper layers are truncated (Fig. 9e) indicating that they are eroded after their deposition.
- (R1) 150–300 m of ~10s m thick, light-toned layer sets dipping ~5° southward (Fig. 9g). This stratigraphic unit is thicker to the north. Each set of layer is underlined in topography by a scarp at the bottom which debris aprons accumulated. In the north part, some sets of layers are truncated at the middle of stratigraphic unit (Fig. 9d), indicating that they have submitted to a local erosion. The upper layers of this stratigraphic unit have been eroded in the southern part

(i.e. layer truncations in Fig. 9e). Notice that the layers at the base of this unit have the same dip as that of R0 (2°S) in the southern part of HiRISE image (Fig. 9a).

- (R2) 50–500 m of layers (Fig. 9g), which individual thickness is difficult to measure because of aeolian mantling and debris aprons (Fig. 9d–f). However, we observed thin, meter-scale, sub-horizontal light-toned layers in the south part of image (Fig. 9f). These layers overlapped northward the previous surface of erosion or unconformity  $\delta$  with a progressive change in dip values (i.e. from sub-horizontal in the central part of the image (Fig. 9e) to 6°S in the northern part of image (Fig. 9d)). The upper part of this stratigraphic unit is truncated by a sub-horizontal surface of erosion (Fig. 9d).
- (R3) 350–700 m of ~10s m thick, light-toned layers, showing an “éventail” mega-structure (Fig. 9b). The detailed mapping of these layer sets shows they overlapped northward with a sub-horizontal dip southward (<2°). This unit is also truncated by an undulating surface of erosion (Fig. 9c).
- (R4) 200–250 m of sub-horizontal, light-toned layers lowly dipping southward. This stratigraphic unit is composed of two members: at the base, ~150 m of meter-scale light-toned layers covered in conformity by four sets of layers, each thick of ~20 m.
- (R5) 200 m to < 50 m of inclined, relatively dark-toned layers which individual thickness is estimated to be ~10 m. Layers overlapped the previous stratigraphic unit (Fig. 9c), suggesting an unconformity  $\delta$  at their base.

Although the two upper stratigraphic units are not easily visible in MOC images, the organization of layers in several stratigraphic units is similar to that observed in HiRISE image. Each stratigraphic unit is separated by an erosional surface or unconformity  $\delta$ , underlined by layer truncations in the lower unit and layers overlaps in the upper unit. Notice that some of these unconformities could pass to correlative conformity, namely surface lacking erosion (e.g. surface  $\delta$  between R0 and R1 to the south, in Fig. 9). In each stratigraphic unit, the layers showed a general bending at their southern end (a sigmoidal shape, or a symmetrical sigmoidal to an oblique clinoform) with a layers dipping at ~6° southward to the front, overlain by a sub-horizontal layers at the top (~1° southward dip), and underlain by sub-horizontal layers (Figs. 8d and 9b). It is particularly well expressed in the stratigraphic units R1–R3.

**4.2.1.2. Middle section of mesa M1.** The middle part of the mesa M1 top is characterized by a 1000 m thick series of <10 m thick layers, arranged in the same geometry as that described previously (Fig. 10): sub-horizontal layers passing progressively to layers dipping 6° southward, as for a clinoform (see Table A2 for measures of layer attitude). Layers change locally in dip orientation (from South to Southeast) and pile up with local sedimentary wedges associated with gradual pinching (distal condensed section).

A 1500 m thick stratigraphic unit S1 with a meter thick planar layer extends over 5 km showing a regional apparent dip of ~3° southward (Fig. 10b and c). The summit of this unit is truncated by an erosional surface  $\delta_2$  dipping 5° southward (Fig. 10b–d). To the south, the stratigraphic unit S1 shows a ~1 km wide and 300 m high convex-shape (Fig. 10b and d). The structure resembles a tectonic fold, but no “extra-dos” faulting is present. If formed by tectonic processes, such as by gravity sliding, the structure must have occurred before layer induration. A diapiric structure is an alternative explanation. Such a structure would form from a bulk difference of material or density, and also before induration (Morgan et al., 1968; Coleman, 1988). In both processes, soft folding without fractures and layer truncation by the erosional surface  $\delta_1$  dipping 10° to the South (Fig. 10d–g) indicate formation before the mesa layers had been built entirely.

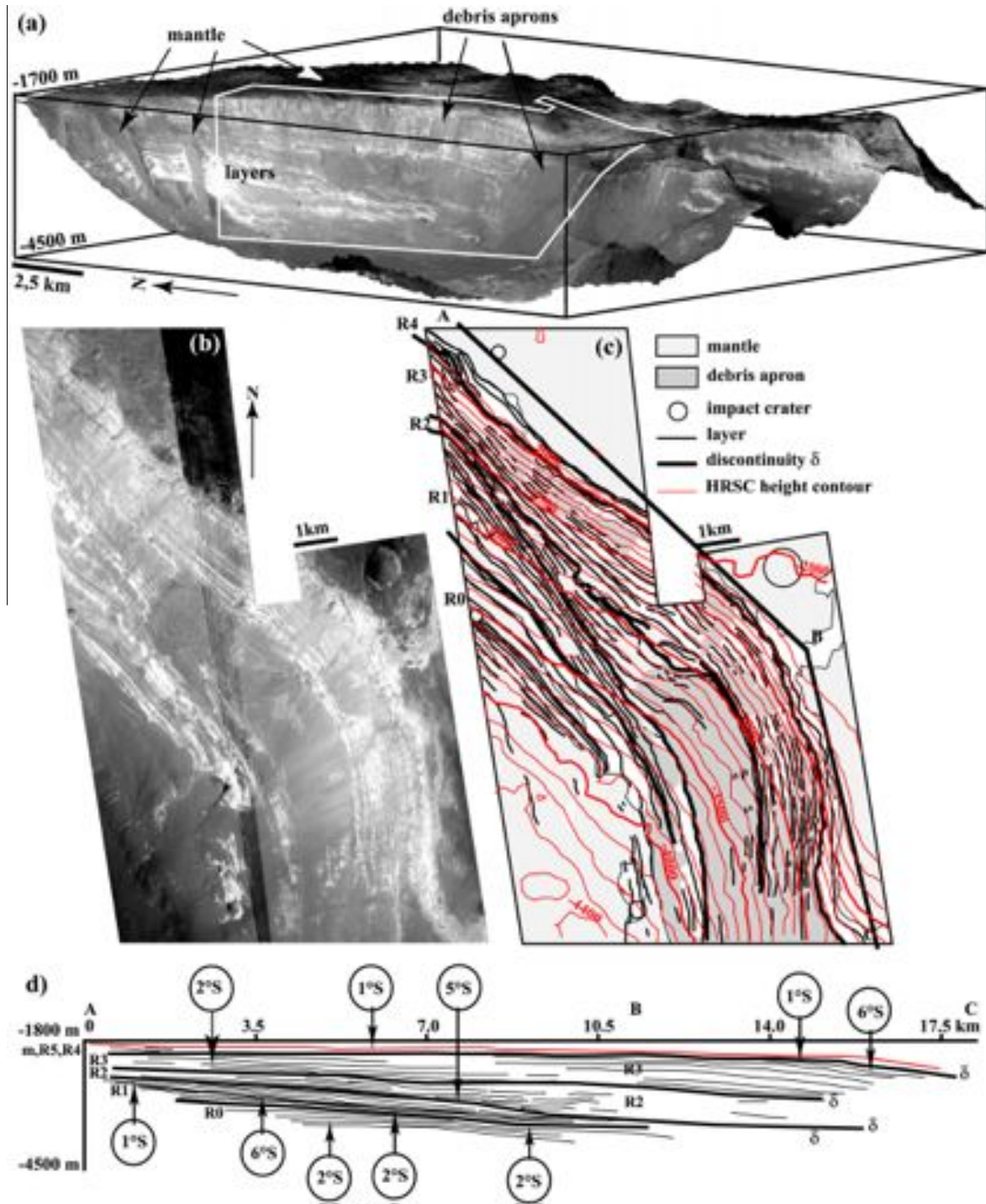


**Fig. 8.** (a) 3D detailed view of the HRSC image focused on the western light-toned side of mesa M1 (see Fig. 6 for location). The top and some places of mesa side are covered by dark dust mantle. Some light-toned layers outcrop on the mesa side with a low dip southward. Few debris aprons are present on different elevations on the mesa side. White box indicates the location of the MOC mosaic. (b) Mosaic of MOC images (R1400141, R0900856, R0801718, R0800448) at resolution of  $4 \text{ m pixel}^{-1}$ . (c) Interpretative map of MOC images on which dust mantle, debris aprons, impact craters and light-toned layers are plotted. The HRSC height contour lines are  $100 \text{ m}$  spaced. Discontinuities are present in the stack of light-toned layers and define the bottom and the top of stratigraphic units labeled R0–R4. (d) Geological cross-section A–B–C made from MOC and HiRISE images (Fig. 9), on which layer dips are labeled in opened-circle.  $\delta$  corresponds to each surface discontinuity separating stratigraphic units. No vertical exaggeration. See the text for explanation.

A series of layers S2 thickening southward is sandwiched between two surfaces of discontinuity,  $\delta_1$  and  $\delta_2$  (Fig. 10). The basal layers of this stratigraphic unit overlapped northward the erosional surface  $\delta_1$  (Fig. 10e). Layers changed progressively their dip values, from  $10^\circ\text{S}$  in southern part of image to  $\sim 1^\circ\text{S}$  above the fold hinge. This “en éventail” structure is characteristic of sedimentary fea-

tures prograding southward parallel to the surface of the discontinuity  $\delta_1$  after a period of erosion.

The upper stratigraphic unit S3 can be observed in detail at the HiRISE scale (Fig. 10b), in an elongated residual butte. Here, layers have a meter-scale thickness, showing local pinching, with a general dip of  $1^\circ$  southward. The southern part of the residual butte

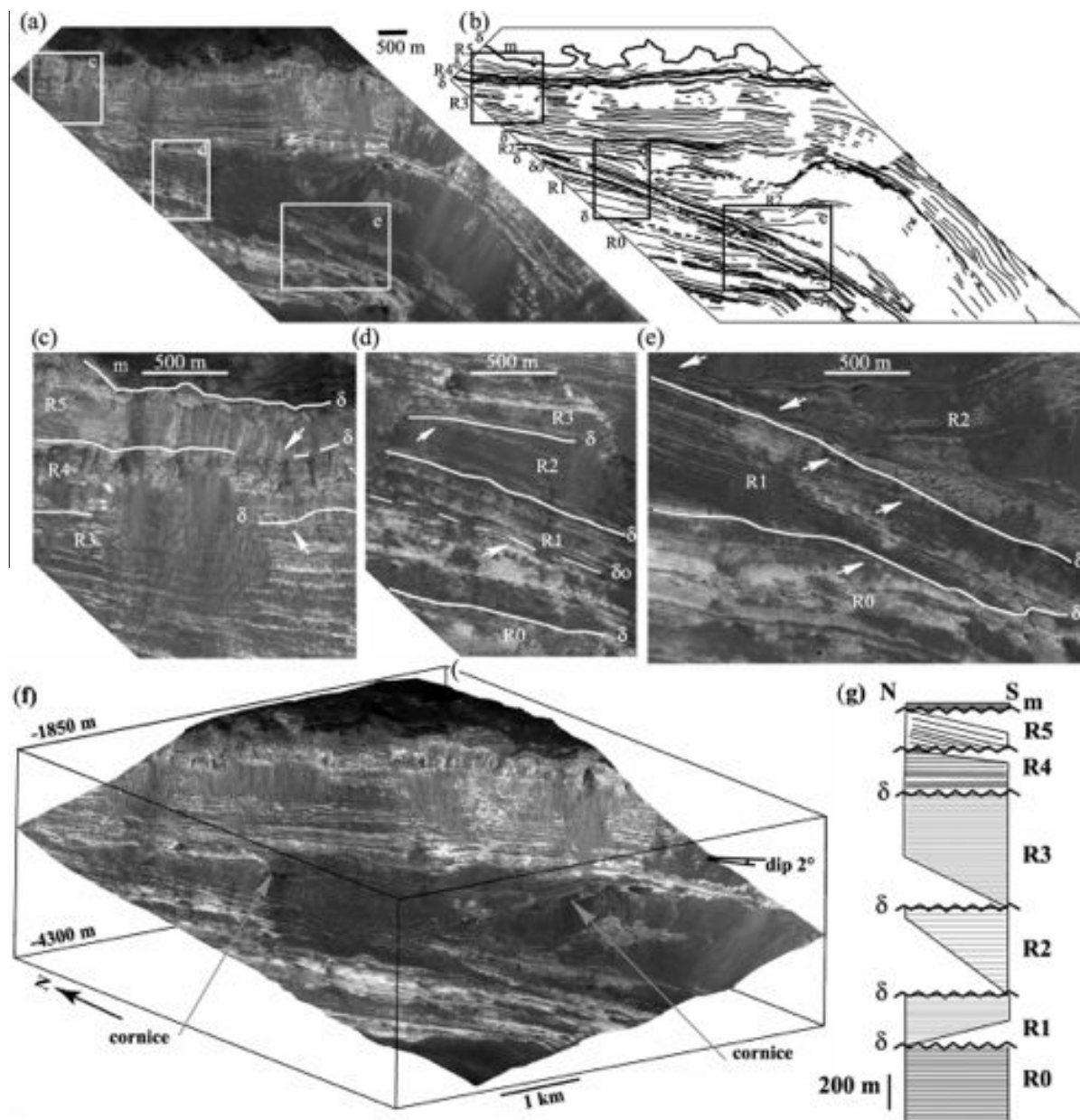


**Fig. 9.** (a) The HiRISE image PSP\_0013160\_1520 displays the different stratigraphic units with a spatial resolution of  $50 \text{ cm pixel}^{-1}$ . (b) Geological interpretative map of layers (thin lines) with main surface discontinuities  $\delta$  (thick lines) separating stratigraphic units labeled R#. "m" corresponds to the mantle. The boxes show the locations of zooms. (c) Detailed view of the upper part of the mesa M1 with three surface discontinuities  $\delta$  separating four stratigraphic units. Arrow oriented downward shows layer downlap whereas arrow oriented upward shows truncation of layers. (d) Detailed view of the central part of the mesa M1 with layer truncations (arrows) indicative of a surface of erosion  $\delta$ .  $\delta_o$  corresponds to a local surface of discontinuity included in the stratigraphic unit R1. (e) Detailed view of the lower part of the mesa M1 with layer truncations (arrows oriented upward) indicating a surface discontinuity. Notice that the layers of the stratigraphic unit R2 onlap the surface discontinuity  $\delta$ . (f) 3D view of the HiRISE image on the HRSC DEM. (g) Stratigraphic log showing the variation in thickness of stratigraphic units at each side of the boundaries of HiRISE image.

shows many layers arranged in wedges, whose upper parts are truncated (Fig. 10b). In the south of the 2 km long topographic pass (Fig. 10a and h), the toe of the hillslope shows stacks of parallel  $\sim 20^\circ$  dipped layers separated by curvilinear or spoon-shaped truncations (Fig. 10h and i). The truncations and wedges could correspond to an erosive surface or to a scour of distributary channels. The channels would be filled by aggrading sand bars viewed in transverse channel cross-sections (Fig. 10h), draped by fine-grained material (i.e. thin sigmoidal shape in Fig. 10g). The channels were  $\sim 200 \text{ m}$  wide and a few tens of meters deep, and their pathway shifted quickly, forming the overlapping spoon-shaped truncations. Many layers of this unit S3 outcropping at the summit of the mesa M1 are associated with hydrated minerals (Fig. 7a).

**4.2.1.3. Southern section of mesa M1.** The southwestern side of the mesa M1 is composed of the following six major stratigraphic units, as seen in detail in the HiRISE image from the bottom to the top (Fig. 11) (see Table A3 for measures of layer attitude):

- (T1) 300 m of meter thick, cohesive, fractured, light-toned layers that are regularly spaced by a succession of more friable layers, a few tens of meters thick.
- (T2) 500 m of meter-scale layers showing numerous sedimentary wedges with local layer dips of  $5^\circ \text{S}$  (Fig. 11).
- (T3) 200 m of meter-scale, sub-parallel, light-toned layers, regionally dipping  $2^\circ$  southward.

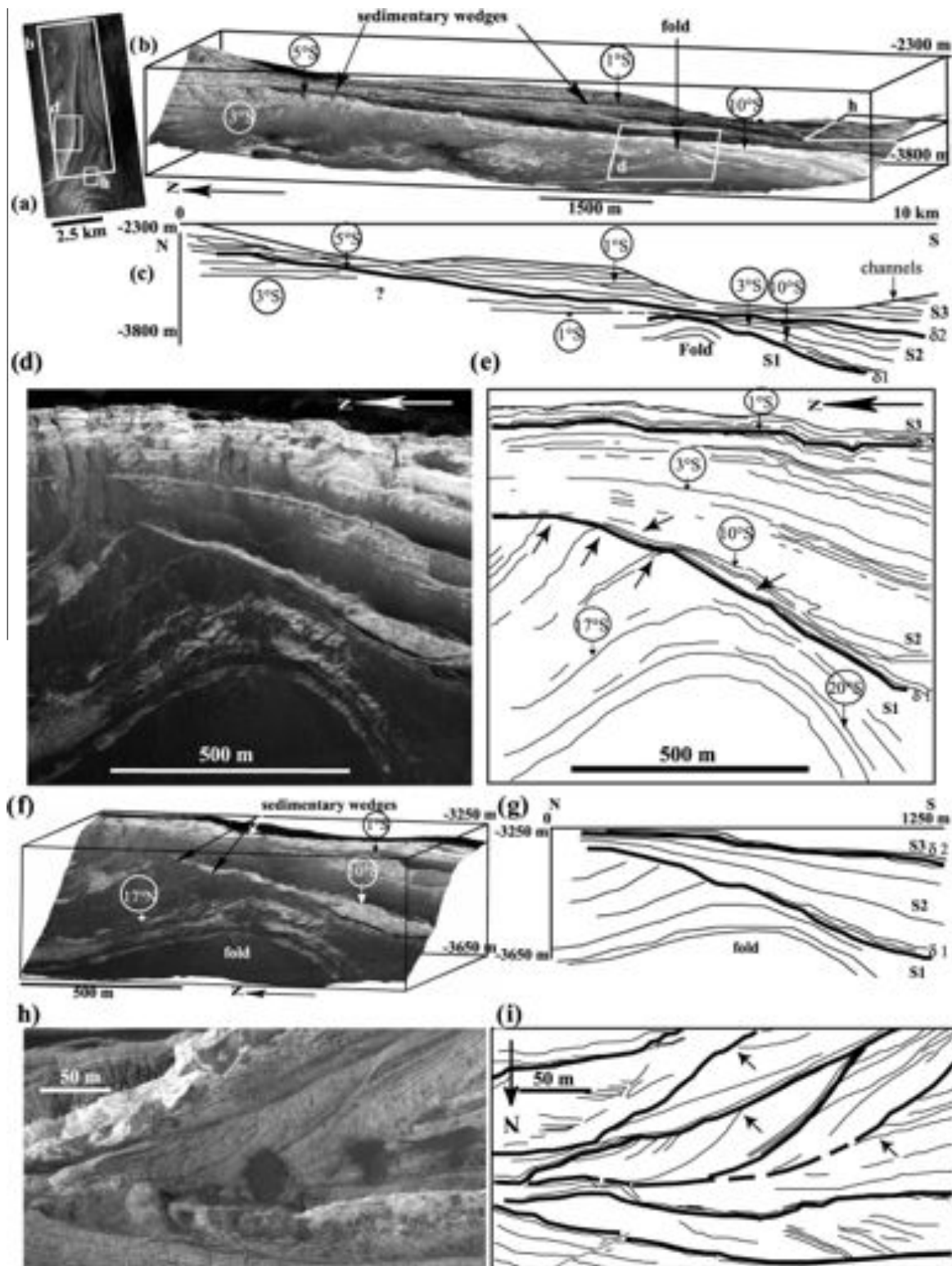


**Fig. 10.** (a) A detailed layers geometry can be determined from the HiRISE image PSP\_001595\_1520 (see Fig. 6 for context). Labels in boxes indicate close-ups. (b) 3D view of the HiRISE image superimposed on the HRSC DEM. Layers have a general sub-horizontal dip southward, but locally they change in dip orientation and angle, and in thickness, forming local sedimentary wedges. (c) Detailed geologic cross-section without vertical exaggeration. S1–S3 are stratigraphic units separated by unconformities  $\delta$ . Layers are in thin lines and unconformities in thick lines. Dip values are indicated in circles. (d) Zoom on the central part of the mesa showing sedimentary wedges on the top of a fold. The map symbols are the same as used in previous cross-section. Arrows indicate truncation. (e) Geologic map made from the close-up. (f) 3D view with no vertical exaggeration. (g) Interpretative geologic cross-section of (d). (h) Sets of light-toned layers showing different dips in value and orientation, and dark aeolian dunes cover partially the layers. This close-up is located at 27.3°S and 74.3°E. (i) Interpretative geologic map of lenticular bedforms with irregular spoon contour (local unconformity in thick lines). Notice that some layers are cross-cut by fault at the bottom of image. Arrows indicate truncation.

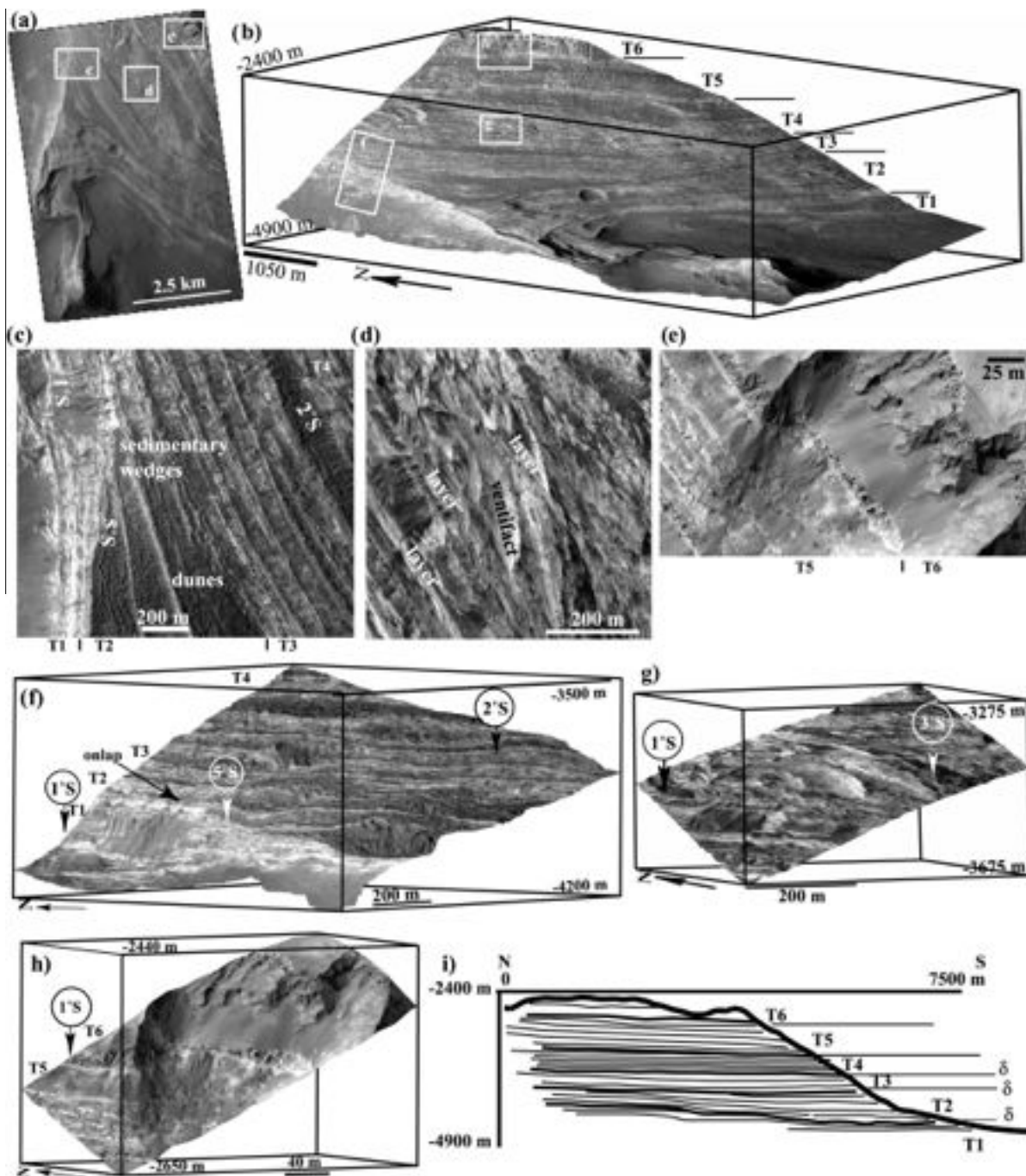


**Fig. 11.** (a) HiRISE PSP\_001662\_1520 image centered on the southern part of the mesa M1 (25 cm pixel<sup>-1</sup>). See Fig. 6 for context. Labels in boxes indicate close-ups. (b) 3D view of the HiRISE image draped on HRSC DEM. Light-toned layers are dipping  $\sim 2^\circ$  southward, except locally in box f. Six stratigraphic units are labeled with T#. Detailed views of these units (north is upward): (c) Close-up on the lower sub-horizontal stratigraphic unit T1 truncated, on which layers of unit T2 onlap with a mean dip of  $5^\circ$ S. These layers are covered by dunes. The upper stratigraphic unit T3 shows a regular dip of  $2^\circ$ S above an unconformity. (d) Detailed view of the stratigraphic unit T4 eroded by aeolian flutes (ventifacts), and fractured leading to an accumulation of meter-scale, angular boulders (a) at their toe. (e) Close-up of the two upper stratigraphic units forming the summit of the southern end of the mesa M1. The stratigraphic unit T5 consists of few meter-thick layers dipping  $\sim 1^\circ$ S. Many debris aprons cover their scarp. The stratigraphic unit T6 is composed of few 10s meter thick, sub-horizontal layers, fractured by polygons, from which boulders accumulate at their toe. (f)–(h) 3D views of the previous close-ups. Dips are indicated in circle. (i) Geologic cross-section where T labels correspond to stratigraphic units. See the text for their description.

(T4) 350 m of thin (<1 m) light-toned layers showing local bending ( $3^\circ$ S) (Fig. 11c), forming sedimentary wedges.

(T5) 500 m of repetitive meter-scale thick, cohesive, light-toned layers alternating with thinner and more friable light-toned layers, whose succession was generally 5 m thick and dipping  $\sim 1^\circ$  southward. The eroded material accumulated at the scarp toe of cohesive meter-scale layers, forming 50 m long triangular, dark-toned, debris aprons.

(T6) 300 m thick stratigraphic unit composed of  $\sim 5$  m thick, sub-horizontal ( $0.5^\circ$ S), light-toned layers fractured at the meter-scale (Fig. 7c), which contained Fe/Mg phyllosilicates (Fig. 7).

**4.2.1.4. Summary.** Based on these data, the geologic cross-section AA' showed the regional structure of light-toned layers in the mesa M1 where data were available (Fig. 12). The summit surface of the

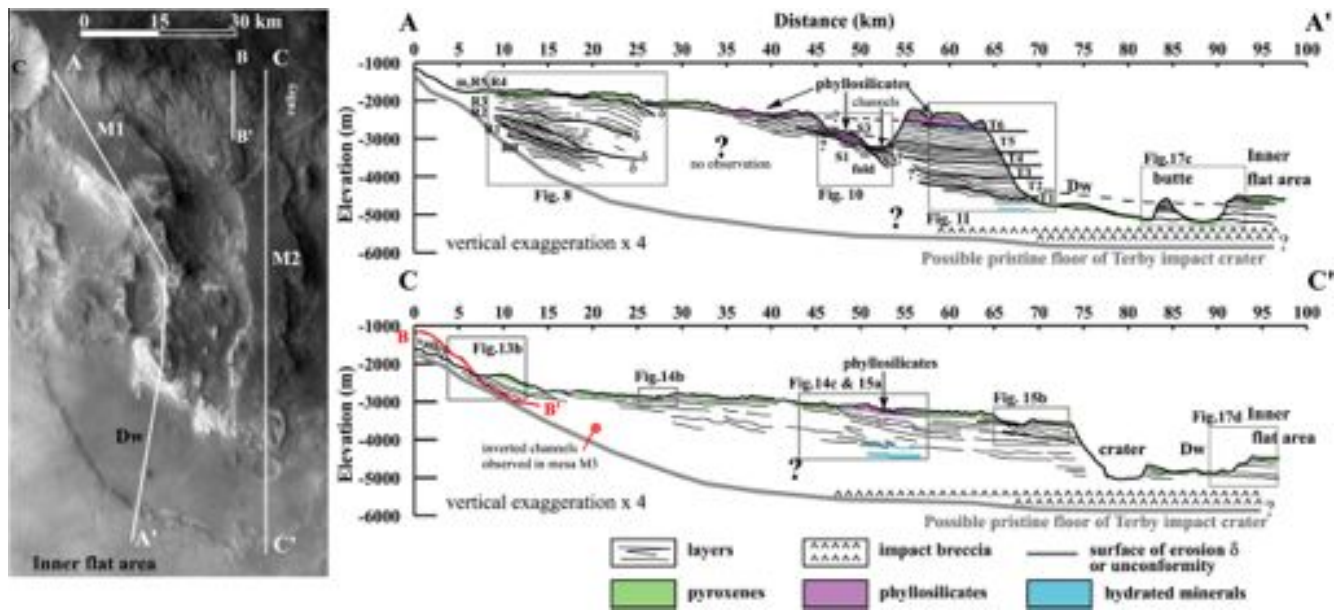


**Fig. 12.** Geologic cross-sections of mesas M1 and M2, made from HRSC images and DEM, MOC and HiRISE images, whose location (AA', BB' and CC') is plotted in the HRSC image (left) viewed in Fig. 6. Topographic profiles AA' and CC' are in black except the BB' in red. The geologic cross-sections are composed of different geologic close-ups previously detailed in reference figure. Thin lines outline major stacks of layers, usually separated by erosional surfaces or unconformities  $\delta$  (thick black lines) highlighted by layer wedges. The mineralogy is deduced from NIR spectral maps: pyroxenes in green, phyllosilicates in purple and hydrated minerals in blue. See the text for detailed explanation. (For interpretation of the references to color in this figure legend, the reader is referred to the web version of this article.)

mesa M1 is partially covered by a dust mantle and pyroxene sand dunes. A series of light-toned layers piles up to a thickness of 2500 m, with a gentle regional southward dip. The geometric arrangement of these layers could not be reduced to a succession of sub-horizontal layers. Detailed measurements indicated that many of the layers are arranged in stratigraphic units of similar geometry, sharply separated from other sequences by a discontinuity surface or unconformity  $\delta$  suggesting that these units experienced a depositional hiatus or an erosional event. Several units (e.g., R1, R2, R3, and S3) show that the layers are arranged in clinoforms or sigmoidal shapes, with the local presence of a syndimentary gravity fold or diapir. In addition, wide distributary channels are present inside the stacks of layers,  $\sim 50$  km away from the Terby impact rim. On Earth, these types of structures are present in sedimentary bodies formed by sub-aqueous depositional regimes. A more detailed interpretation and discussion is presented in Section 5.1.

#### 4.2.2. Mesa M2

The central mesa M2 is characterized by a relatively smooth surface, tilted  $0.7^\circ$  southward, standing at  $-3$  km (Fig. 1). The 3D HRSC view shows that the summit of the mesa M2 is covered by a dark mantle, and that the western side, 1.5 km high, is composed of sub-horizontal light-toned layers (Fig. 13a). On contrary to the mesa M1, this mesa starts at the outlet of a 10 km wide, N–S trending valley that crosscuts the crater rim (Figs. 1 and 13). The valley head stands at  $-1500$  m in elevation (Fig. 1) at the mouth of a plain located north of Terby.

On the northern side of mesa M2, the summit consists of light-toned, layered material, easily eroded by wind (Figs. 7d, 14b), dipping regionally  $1\text{--}2^\circ$  southward with lateral variations reaching  $5^\circ$  (see Table A4 for measures of layer attitude). In the southern part of the mesa M2, the layers keep this regional gentle dip (Fig. 14). Near the southeastern end of the mesa, the upper layers show a kilometer-scale “en éventail” structure (Fig. 15b) with flat layers on the summit overlapping layers dipping  $4\text{--}8^\circ$  southward. The dipped layers may correspond to beds truncated at their upper part

by an erosion surface that are covered by late horizontal beds passing southward to beds dipping at  $8^\circ$ . This layer arrangement is comparable to a clinoform downlapping previously eroded dipped layers and the structure stands between  $-3500$  and  $-4000$  m in elevation.

The mineralogy of these layers is partially shown by CRISM data that indicates that they are composed of Fe/Mg phyllosilicates at the top of the mesa (Figs. 4, 5b and 15a) and undetermined hydrated minerals at the toe of the mesa ( $-4500$  m in elevation). Although the layers at the summit of the mesa consist of Fe/Mg phyllosilicates, as for mesa M1, their nature appears to be more rich in Mg (absorption bands around  $2.31\text{--}2.32$   $\mu\text{m}$ ) as compared to those found on the summit of the mesa M1, suggesting that these phyllosilicates could be saponite (Fig. 5b and c).

A geologic cross-section CC' is proposed (Fig. 12) displaying a general organization of layers similar to those observed in the western mesa M1: regional sub-horizontal layers passing to “clinoform” structures (a flat-to-gentle dip of  $<10^\circ$ ) whose closest analogue could consist of sub-aqueous sedimentary deposition.

#### 4.2.3. Mesa M3

The mesa M3 was less targeted by the various instruments. The lack of high resolution images on this mesa M3 was a limit to the understanding of depositional processes and environments. Nevertheless, the mesa M3 was the only one attached to the flat inner area of the Terby impact crater, and at this setting, the internal organization of the layers would be a key for determining the nature of the whole filling for the Terby impact crater. MOC images show that the mesa consists of a thick succession of sub-horizontal, meter-scale, and light-toned layers with numerous local layer wedges, indicative of erosional surfaces before the late upper deposit. The layers are, in general, partially covered by a thick dust mantle and numerous dunes, tens of meters long. The HiRISE image (Fig. 16) allowed us to observe the northern part of the mesa M3, where the layers are arranged in two major units: the summit consists of a  $\sim 200$  m thick stack of meter-scale thick, relatively dark layers, fractured, and forming numerous boulders (Fig. 16b

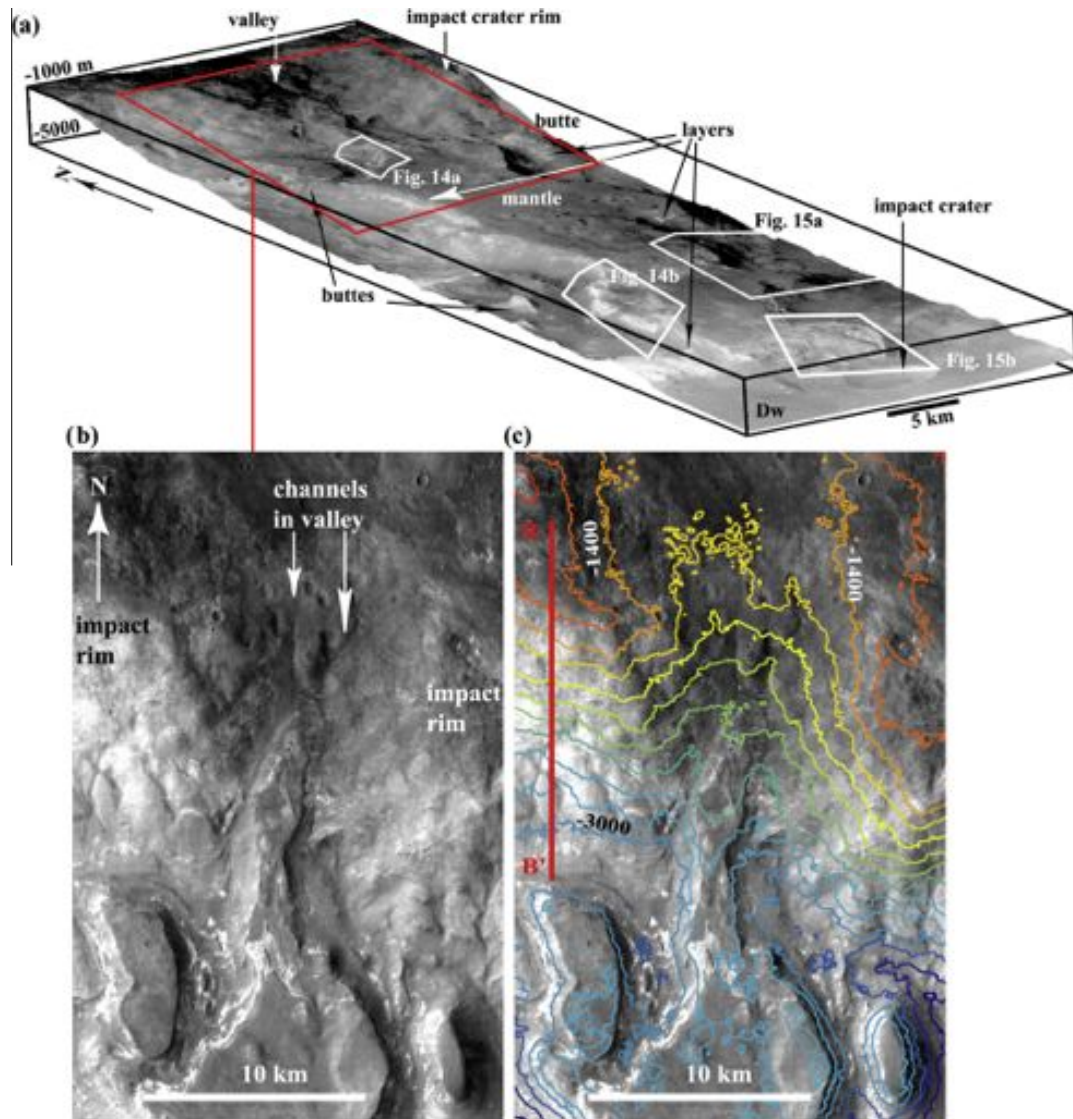


**Fig. 13.** (a) 3D view of the mesa M2 observed by the HRSC camera. Its topographic summit is very flat lowly dipped southward. Its western scarp shows a sub-horizontal light-toned layer. Note that northern side of the mesa M2 starts at the outlet of valley incising the Terby impact rim (red box). (b) Close-up of the northern side of the mesa M2, showing a valley cross-cutting the Terby impact rim in which several channels are present. The bottom of the valley is filled by layers belonging to the mesa M2. (c) Same HRSC image on which color HRSC height contours are spaced of 200 m. The Red line corresponds to the location of topographic profile BB' viewed in Fig. 12. (For interpretation of the references to color in this figure legend, the reader is referred to the web version of this article.)

and d). The bottom consists of a  $\sim 100$  m thick stack of thin, light-toned layers composed of material easily eroded by wind-driven abrasion forming yardangs (Fig. 16b and d).

At the toe of the northeastern part of the mesa M3,  $>100$  m long,  $\sim 40$  m wide sinuous ridges show an immature branching organization (Fig. 16c), suggesting that they are inverted channels (i.e. channel deposits indurated and inverted by differences in erosion). The landforms were observed on a  $<3^\circ$  SW tilted surface at an elevation of  $-3700$  m in MOLA data. The HiRISE image showed that these inverted channels are embedded within light-toned layers (Fig. 16c). The geometric relationship may indicate that river streams were once running at the elevation of  $-3700$  m before the upper stacks of layers were deposited. Alternatively, the layers could form in a sub-aqueous environment (i.e. distributary channels of sub-aqueous fan).

No geologic cross-section is plotted for M3 due to the lack of high resolution imagery. Nevertheless, the location of inverted channels observed in this mesa M3 is indicated in the cross-section of the mesa M2 (Fig. 12).

### 4.3. Geometry of layers in the closed depressions

Light-toned layers also outcrop in remnant buttes present between the mesas, on the floor of a closed-depression Dw (Fig. 17), implying that the layers were continuous between the mesas and for the inner flat area of the Terby impact crater before erosion. Using MOC images and HRSC DEM in combination, the geometry of these light-toned layers appears relatively flat with dip angles on the same order as those observed for the mesas (Fig. 17). However, the dip angles decrease progressively southward in the remnant buttes south of the mesa M1 (Fig. 17b and c) and reach the horizontal level in the layers observed in the northern scarp of the inner flat, a 700 m high area (Fig. 17c and d) (see the Table A5 for the layer attitude). The mineral composition of these layers remains unknown due to a lack of NIR data. However, they have the same geomorphic characteristics as light-toned layers in mesas. Geologic cross-sections were completed based on these observations (Fig. 12), and showed the spatial continuity of light-toned layers up to the inner flat area of the Terby impact crater.

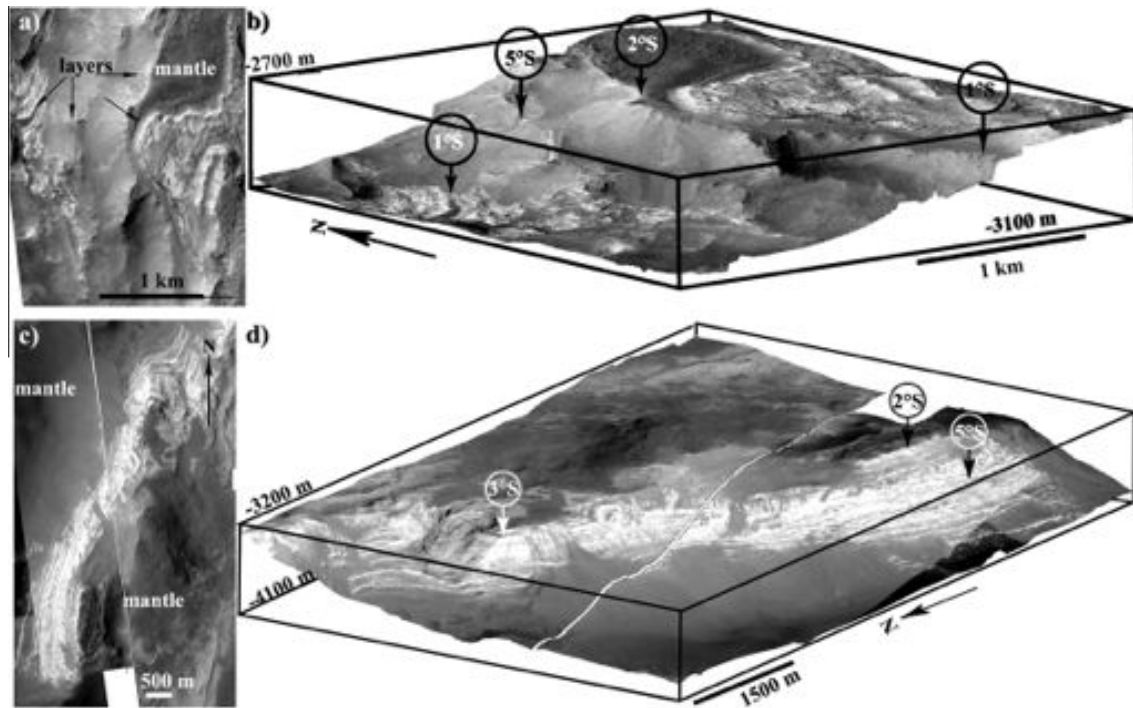


**Fig. 14.** (a) Zoom on the HiRISE PSP\_006831\_1525 image located at the northern part of the mesa M2 (see Fig. 13 for location): remnant butte and light-toned layers showing a low dip southward at the summit. Some ripples and dunes are present on the top of benches. Whole western scarp of the Mesa M2 showing a set of sub-horizontal light-toned layers partially covered by dust mantle. (b) 3D view of the western scarp of the Mesa M2 on which layer dips are labeled in open-circle. (c) Detailed view on the central part of the mesa M2, extracted from the mosaic of MOC images (M1901933, R0300753, R0301060, R0301404, R0400232, E102645 and E1700114): remnant buttes at the summit and regional low dipping of layers southward, viewed in 3D on the right (d).

#### 4.4. Mineralogy of the southern impact crater

In the southern part of the Terby impact crater, a ~45 km diameter complex impact crater stands on the Terby impact rim and the inner flat area (Figs. 1 and 18). The impact crater displays degraded ejecta that blanket part of the inner flat area of the Terby crater (Fig. 18), implying that it postdates filling. Ejecta display an intermediate/dark tone in night-time IR THEMIS images (Fig. 18b), suggesting that they consist of non-cohesive, fine-grained material. From a mineralogical point of view, the OMEGA orbits #2327 and #232 show that these ejecta have a high amount of pyroxenes (Fig. 16e). The associated OMEGA spectra show two broad absorption bands centered at 1.0 and 2.2  $\mu\text{m}$  that are interpreted as a pyroxene signature (Fig. 3b).

The impact crater displays a relatively high degradation level since its 1.5 km high inner rim appears mantled and carved by old gullies and landslides (Fig. 18a). The floor appears relatively smooth at the visible THEMIS image scale, in the NE and SW part (Fig. 18a) as confirmed by the dark signal in night-time IR THEMIS images, indicating that this area is covered by fine-grained material upon which the OMEGA data show a characteristic pyroxene signature (Fig. 18b).

The central peak is partially rough on its northern side (Fig. 18a) and is correlated with a bright signal in night-time IR THEMIS images (Fig. 18b), indicative of a coarse-grained material or indurated/rock outcrop. The material is associated with an olivine-rich area as determined by the OMEGA spectrometer (Fig. 18b). The spectra extracted from orbit #h2327 show a broad absorption band between 0.8 and 1.5  $\mu\text{m}$  characteristic of the olivine family. The bands are not relatively flat for wavelengths  $>1.5 \mu\text{m}$ , as expected for an olivine signal, but they do show a broad absorption band from 1.2 to 2.2  $\mu\text{m}$  that, which would correspond to a mixing of olivine and pyroxene minerals. The pattern implies that the central peak would consist of mafic bedrock (olivine + pyroxene), mantled later by local olivine + pyroxene dust/sand.

No hydrated mineral was detected in the central peak and in the ejecta. As the impact crater postdates the filling of the Terby crater, the observation suggests either that sedimentary filling of the Terby crater is thin, or absent, at this location, and that the majority of the ejecta would correspond to the mafic basement, or alternatively that the filling does not represent a significant proportion of the altered minerals here.

#### 4.5. Late geologic landforms in the Terby impact crater

The inner flat area and the mesas are mantled by dust and dunes (Fig. 7e), or eroded by ventifacts (Fig. 7d) indicating that the currently active geologic process is wind. A second active process is the diurnal w/o seasonal frost/defrosting, likely favoring the cryo-fracturation of cohesive material (e.g., fractures in light-toned layers, Fig. 7c). Viscous flows were also observed in mantled ice-rich areas having a relatively steep slope (e.g., viscous flows in 20 km-in-diameter impact craters on the northern rim of the Terby impact crater, Fig. 1e).

The Terby impact crater has also been subjected to late minor fluvial activity. Small valleys (V, in Fig. 1) are found on the eastern side of the Terby impact crater, and they debouch on the current inner topography of the Terby impact crater. Sedimentary deposits are difficult to determine with confidence using the available data, but they partially incise the flat inner area (e.g., 75.5°E/28°S in Fig. 1e). On the northwestern side of the floor of the Terby impact crater, several late alluvial fans are found (Fig. 19) where meandering channels are present. The northern alluvial fan (Fig. 19b), as first observed by Wilson et al. (2007), covers a 11 km  $\times$  15 km area tilted by 2° southward, and its distal region covers an older alluvial fan whose distributary channels have an inverted topography due to wind-abrasion (Fig. 19c). Although cratered, the channels formed relatively late in the history of filling for the Terby impact crater since they formed after the deposition and subsequent erosion of mesas M1 to M3 layers.

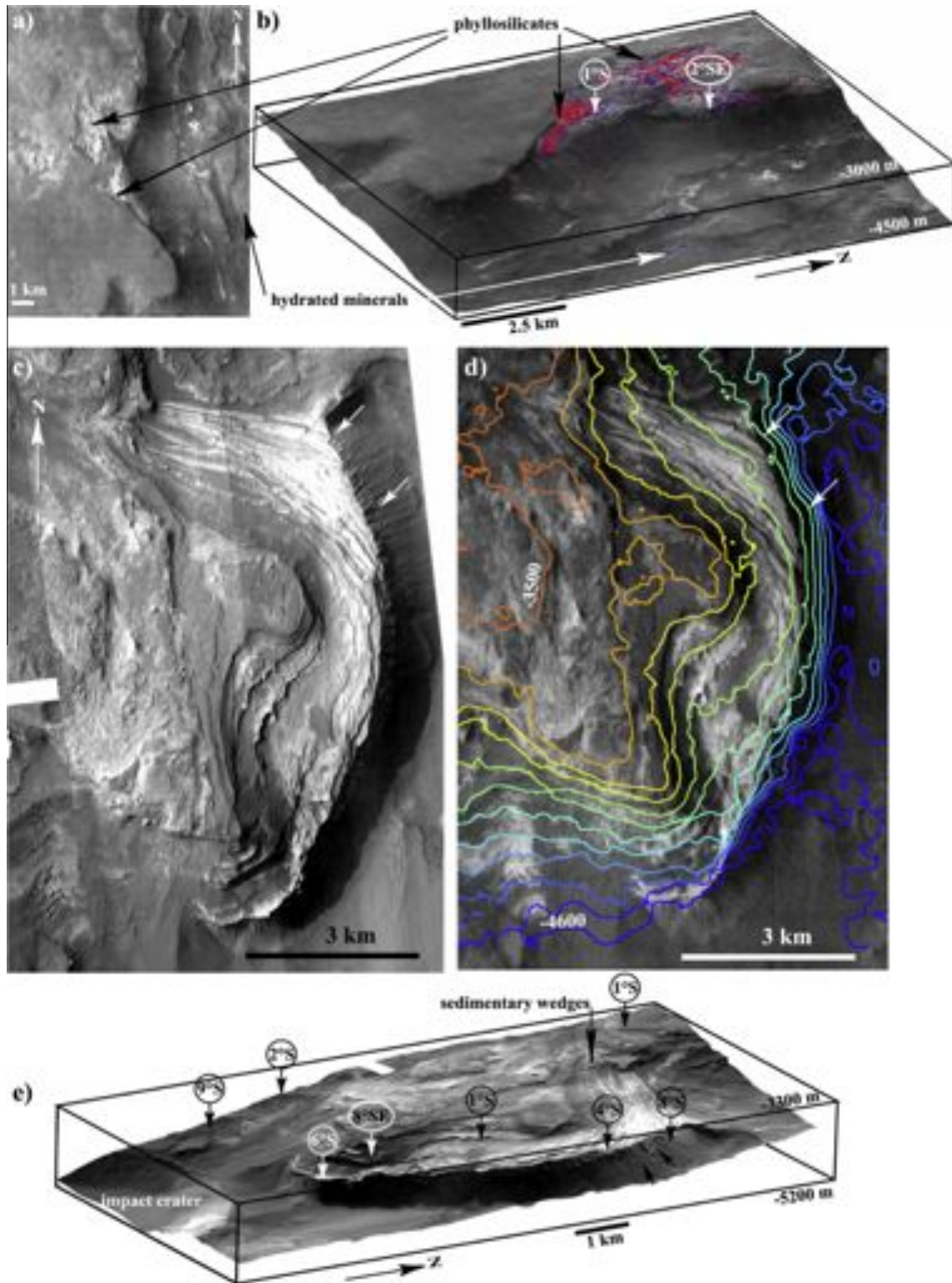


**Fig. 15.** Detailed views on the eastern side of the mesa M2 (see Fig. 13 for context): (a) Zoom on HRSC image showing bright layered areas at the summit of the mesa lowly dipping southward. (b) Same image draped on HRSC DEM, on which phyllosilicates (red–blue regions) have been detected by CRISM. At the toe of the mesa, the floor shows remnant buttes composed of light-toned layers on which hydrated minerals (blue regions) have been detected by CRISM. (c) Detailed view of the southeastern end of the mesa M2 showing a set of thin light-toned layers dipping regionally southward with different dip values forming layer wedges. This view corresponds to a close-up of the mosaic of MOC images (M1901933, R0300753, R0301060, R0301404, R0400232, E102645 and E1700114). Arrows point a set of layers dipping to the south viewed in two orthogonal sections (plan view in left and vertical view in right). (d) The same area viewed by the HRSC camera, on which the HRSC height contours spaced of 100 m are plotted. The arrows indicate the location of layers dipping to the South. (e) 3D view of the MOC image mosaic draped on the HRSC DEM showing the sedimentary wedges. (For interpretation of the references to color in this figure legend, the reader is referred to the web version of this article.)

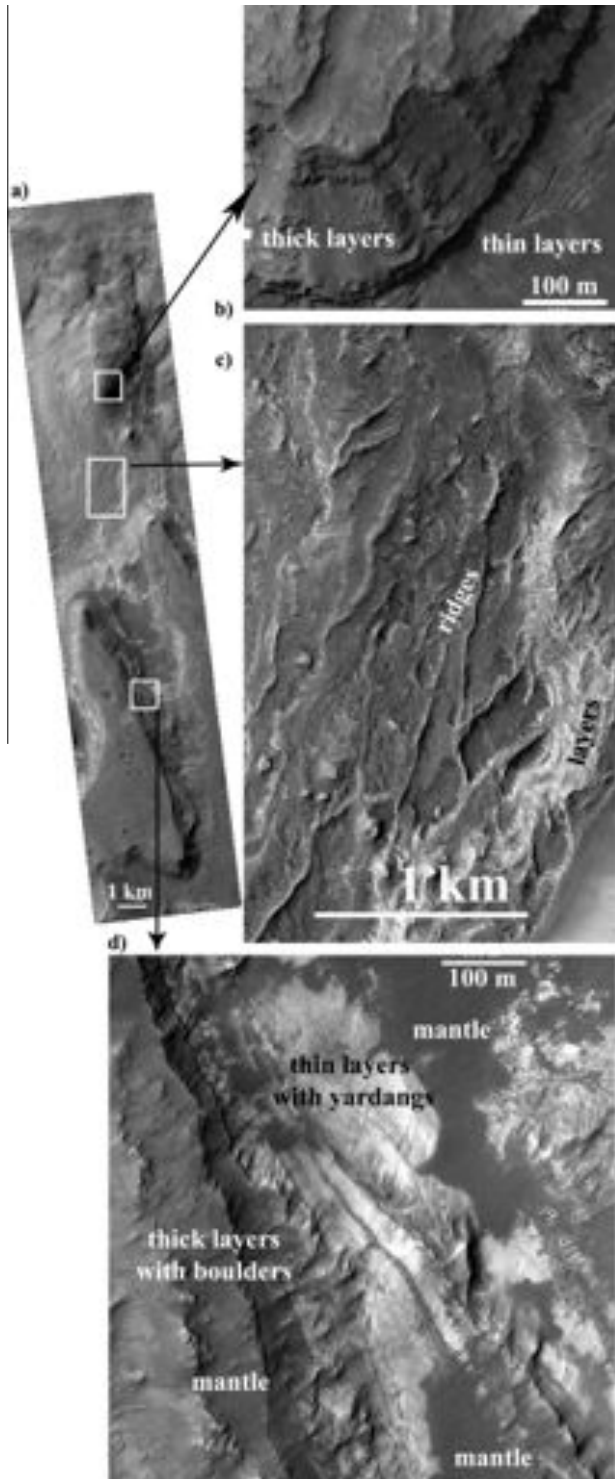


**Fig. 16.** Layers within the northwestern part of the mesa M3 (see Fig. 1 for context): (a) HiRISE PSP\_006475\_1525 with a spatial resolution of 25 cm pixel<sup>-1</sup>. (b) Detailed view of layers forming a remnant butte: few 10s m thick, fractured layers with sedimentary wedges superposing on few meters thick, light-toned layers. (c) The bottom shows sinuous, branching ridges which are partially covered by light-toned layers at the East. (d) light-toned layers are composed of fine-grained material easily eroded by wind-driven abrasion forming yardangs, and they are partially covered by ripples and dunes. The upper thick layers are fractured from which numerous boulders are broken away.

#### 4.6. Age of Terby impact crater and its filling

For our study, we used two methods to estimate the surface retention age of the Terby impact crater and its filling: (1) cumula-

tive crater counts per 10<sup>6</sup> km<sup>2</sup> (Tanaka, 1986, for craters ≥ 1 km in diameter), and (2) the density of craters per km<sup>2</sup> versus their diameter plotted on a logarithmic incremental histogram (Hartmann and Neukum, 2001). We applied these two methods on a mosaic of day-time IR THEMIS images for the entire area (48,709 km<sup>2</sup>) as shown in Fig. 1, and on the filling of Terby crater (20,252 km<sup>2</sup>), including mesas, closed depressions and the inner flat area.

Although the area studied is limited to a small region around the Terby impact crater, we found a Noachian age for the Terby impact crater based on the population of large age impact craters (e.g.  $N(16)/10^6$  km<sup>2</sup> and  $N(5)/10^6$  km<sup>2</sup> (Table 3)), as also observed in the crater density graph versus crater diameter, for which large (>5 km in diameter) impact craters cross-cut the Noachian period until the Hesperian (Fig. 20). This result suggests that the region has been subjected to intense geological processes as compared to impact flux during the Noachian and Hesperian periods. The region has been in equilibrium with the impact flux since the end of the Hesperian, since the density of the impact craters follows an isochron between 3.0 and 3.5 Gyr (Fig. 18). The result confirms previous work based on Viking images (Tanaka, 1986; Leonard and Tanaka, 2001), for which the Terby impact crater was determined to have formed in the Early Noachian bedrock after the formation of the Hellas basin.

The inner filling of the Terby impact crater has been dated to the boundary of the Noachian/Hesperian periods (Barlow, 1990; Leonard and Tanaka, 2001), based on Viking images. Our crater counts based on THEMIS imagery suggests a slightly younger age up to the middle of the Hesperian period (3–3.5 Ga), taking into account both the cumulative crater count per 10<sup>6</sup> km<sup>2</sup> and the density of craters per km<sup>2</sup> versus their diameter (Table 3 and Fig. 20). These results suggest that the infilling began during the Noachian period and ended either at the end of the Early Hesperian or the beginning of the Late Hesperian (see also Ansan and Mangold, 2004; Ansan et al., 2005; Wilson et al., 2007). Therefore, late alluvial fans (Fig. 19) which superpose the inner flat terrains and eroded sections of mesa deposits formed during this later Hesperian period and are disconnected from the main deposition episodes during the Middle to Late Noachian.

### 5. Geologic history of the Terby impact crater

Given the large number of anomalous Noachian craters at the surface of Mars, understanding the nature of thick filling in the Terby crater is fundamental for understanding Early Mars since in the Terby impact crater, the deposits have been eroded and are accessible over a thickness >2 km. Such a thick stack of deposits may have formed from a variety of processes including: (i) aqueous deposition, (ii) aeolian deposition, (iii) volcanism, and (iv) mass wasting. Hereafter, we show how the various processes can, or cannot, explain the observations before discussing a chronological scenario of formation.

#### 5.1. The formation of mesa deposits

##### 5.1.1. Sedimentary processes

In the northern area of the Terby impact crater, three mesas display a ~60-km long, relatively flat plateau with a sharp, convex-shaped edge. The mesas are composed of meter-scale layers arranged in stratigraphic units or depositional sequences bounded by erosional surfaces or unconformities (Fig. 12). As suggested from a detailed study of the mesas, many observations favor a depositional architecture that originated in a fluvio-lacustrine setting:

- (1) Layers display a unique geometry (e.g., Fig. 12) with an upper platform displaying sub-horizontal sediment layers (i.e. topset), passing gradually to layers dipping 6–10° southward

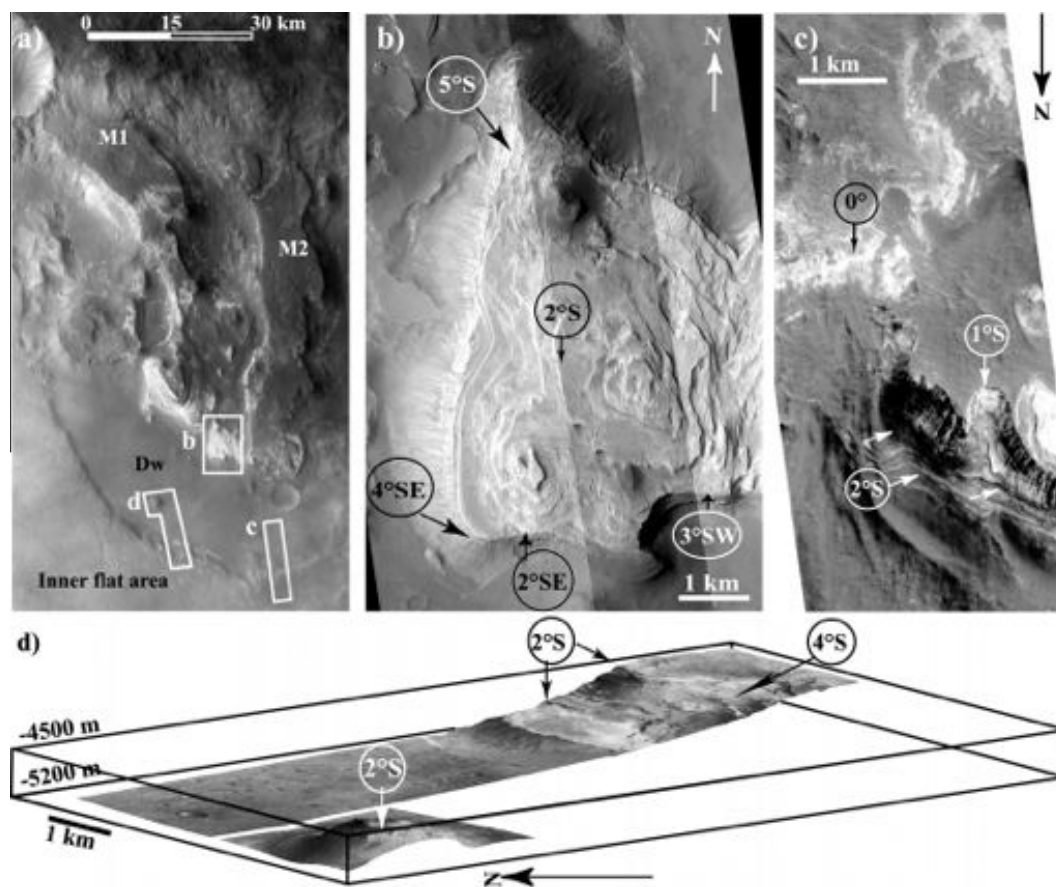


**Fig. 17.** Layers in closed-depression Dw: (a) HRSC nadir image on which are located detailed views (white boxes). (b) Mosaic of MOC images (R0402025, R0500253, and R0501482) showing the remnant butte inside the closed-depression Dw, consisting of layers dipping gently southward. (c) Close-up of MOC image (R1200951) showing the northern scarp of the inner flat area of Terby. It consists of layers lowly tilted southward. Notice an unconformity pointed by white arrows. (d) 3D view of mosaic of MOC images (R0800448 and R0801718) draped on HRSC DEM, showing the residual butte and the northern scarp of the inner flat area of Terby crater containing light-toned layers.

(i.e. foreset), along a horizontal distance of a few hundred meters to kilometers, and terminating as horizontal to gently-inclined layers (i.e. bottomset). The general shape corresponds to a sigmoidal clinoform characteristic of sub-aqueous accumulation of clastics upon a slope (e.g., Rich, 1951; Mitchum, 1977; Reading, 1996), and usually results from grain sorting along the clinoform (i.e. gravel/sand in topset and foreset, silt, and clays in bottomset). The clinoform surface is indicative of the slope depositional surface that is commonly associated with strata prograding into deep waters (Mitchum, 1977).

- (2) Layers are stacked with the same stratal pattern (clinoform), forming >1 km long and >100 m thick sedimentary wedges (i.e. onlaps and downlaps). The sets of conformable layers are truncated by local or widespread erosional surfaces or unconformities (Figs. 8–15), forming local sedimentary wedges. Such sizes and architectures of sedimentary wedges are characteristic of depositional sequences present in fan delta (Vail, 1987).
- (3) Such a sequence in geometry has been observed several times, at different elevations, and for different locations inside both mesas M1 and M2 (Fig. 12). The lateral succession of this depositional sequence may indicate that a fan delta extended toward the center of the lake (i.e. progradation), and thickened along a vertical axis (i.e. aggradation) depending on filling phases.
- (4) The progressive junction of the mesa M3 top into the inner crater layers indicates that the deposition of mesa material

is connected with inner crater filling, with its upper flat surface standing at  $-4.5$  km in elevation. The geometry is similar to that observed in terrestrial fan deposits that progressively join lake-bed filling composed of a series of sub-horizontal layers. The layer geometry in Terby crater also argues for a continuity of M3 with M1 and M2, and inner crater filling whose current moat shape (closed depressions) includes residual layered buttes (Fig. 17), and is probably due to a later erosion rather than to a lack of sedimentation.

- (5) A few transverse cross-sections of distributary channels have been observed approximately 50 km from the Terby impact rim inside the stratigraphic units S3 and T4 of mesa M1 (Figs. 10c and 12). These channels show wing-shaped sedimentary structures interpreted to be fine-grained bars (i.e. sand and silt) locally draped by shale layers. The sedimentary structures are characteristic of channel deposits (Allen, 1983), and their presence in a depositional sequence of the fan delta faraway from the Terby impact rim suggests that they are distributary channels of a sub-aqueous fan or a delta fan.
- (6) The presence of inverted channels inside layering (Fig. 16) highlights the presence at one elevation (and at one lapse of time) of channelized, confined flows that are either a part of an alluvial fan or proximal area of sub-aqueous fan deposits. Alluvial fans are a possible hypothesis for explaining part of the layers structures, such as, for example, material dipping toward the basin center. However, alluvial fans display

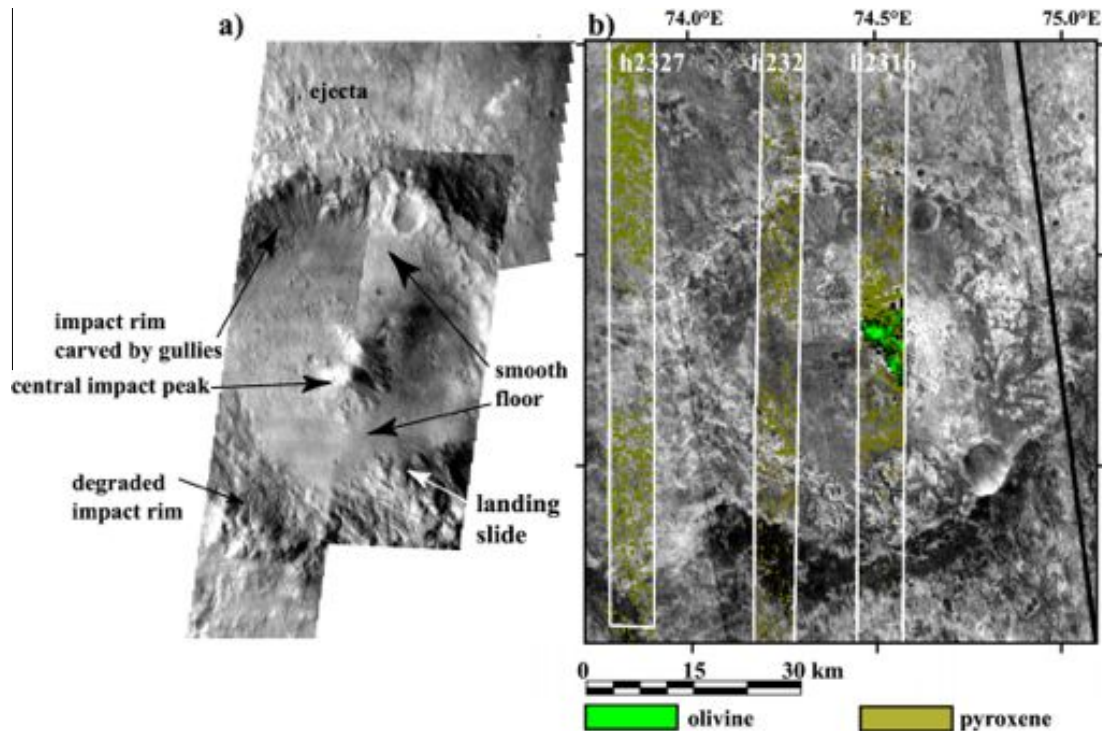


**Fig. 18.** Complex impact crater at the boundary of the southern Terby impact rim and the inner flat area (see Fig. 1 for context). (a) Mosaic of available visible THEMIS images at a resolution of  $17 \text{ m pixel}^{-1}$  (V06739001, V10446001, V05266001, V07850005, and V15962001). (b) Close-up of the night-time IR THEMIS images on which the OMEGA mineral map is plotted. The scale is the same for two images.

decreasing, not increasing, slopes outward, which contradicts the clinofrom geometries we have described.

Therefore, layer geometry favors a depositional system in a water body such as a fan delta complex and/or a deep-water fan. This sedimentary environment is quite different to that proposed by Wilson et al. (2007) favoring lacustrine environment without fluvial contribution (no alluvial fan *s.l.* or delta fan). The potential Terby sub-aqueous fan complex would include mesas and a part of the closed-depression Dw in which residual layered buttes are observed like two buttes located on the western side of Mesa M1 (Fig. 1). The sub-aqueous fan complex would cover  $\sim 3750 \text{ km}^2$ , bounded between the latitudes of  $26.6^\circ\text{S}$  and  $28^\circ\text{S}$  and the longitudes of  $73.6^\circ\text{W}$  and  $75.4^\circ\text{W}$ . Based on the eastward decrease in elevation for the present-day summit of the mesas (Fig. 1c), we estimate that the mean height of the overall sub-aqueous fan complex is  $\sim 1.5 \text{ km}$ , taking the reference elevation of the base as  $-5000 \text{ m}$ . The sedimentary volume would be  $\sim 5625 \text{ km}^3$ . The delta would have formed in a deep lake (i.e.  $3000 \text{ m}$  for a maximum depth), with a maximum level standing at  $-2000 \text{ m}$  in elevation, corresponding to the highest summit of the mesas.

#### 5.1.2. Alternative and/or additional processes

While geometric properties of the mesa are in favor of sedimentary processes, other processes could have formed or contributed to layer accumulation. Aeolian deposition on Mars can form dust deposits or sand dunes. Aeolian mantling by dust (i.e. air-fall dust deposit) would homogeneously drape the topography and would not show such a variety in sedimentary layered structures with various thicknesses, such as a gentle dip toward the crater center in the location where no underlying topography is present. However, we do not exclude a contribution for aeolian dust in the inner crater layers that are flat and regular, as proposed by Wilson et al. (2007) and Grant et al. (2009).

Sand-sized grains can generate dunes that can display internal structures, such as bedsets, cross-bedding, reactivation surfaces, and high angle foresets. However, these internal structures of aeolian dunes have a meter-scale or smaller that cannot be observed at the scale of orbital images, even with a resolution as high as the HiRISE one. The structure of the layers inside the Terby mesas is difficult to explain with sand dunes only: clinofroms with a single direction of dip at the hecto/kilo-meter-scale, as observed in several sequences, are not observed in aeolian structures in which internal stratification is oblique, parallel to the grain slip-face, and embedded in large-scale tabular sand sheets. Dark sand dunes are known to fill many large impact craters of the southern hemisphere. Mesas layers could correspond to the erosion of indurated sand dunes deposited a long time ago. However, no large aeolian dune has been observed as being composed of light-toned deposits (Malin and Edgett, 2000), except for the case of indurated sulfate dunes in Meridiani Planum (Grotzinger et al., 2005; Metz et al., 2009a,b). Dunes are generally composed of dark material containing pyroxenes, but pyroxene seems to only be present in mesas as aeolian mantling that formed later than for erosion. Therefore, the mineralogy of layers does not favor an aeolian assemblage, too.

Volcanic filling has to be considered since the Terby impact crater is not far from volcanic regions like Tyrrhena Patera (i.e.  $\sim 1500 \text{ km}$ ). A succession of volcanic events could lead to a vertical stacking of volcanic ash and/or lava flows. However, the texture of individual layers with fine grained light-toned layers is different from any of the volcanic lava flows that have been observed on Mars. Perhaps volcanic ash could explain such a thin accumulation of bright material containing phyllosilicates, as has been proposed, for example, in the Mawrth Vallis region (Loizeau et al., 2007). However, the spatial arrangement of layers would be very different from those observed in the mesas: Volcanic ash, like aeolian dust, drape the topography homogeneously, and cannot generate such an internal structure. Additionally, no geomorphic landform

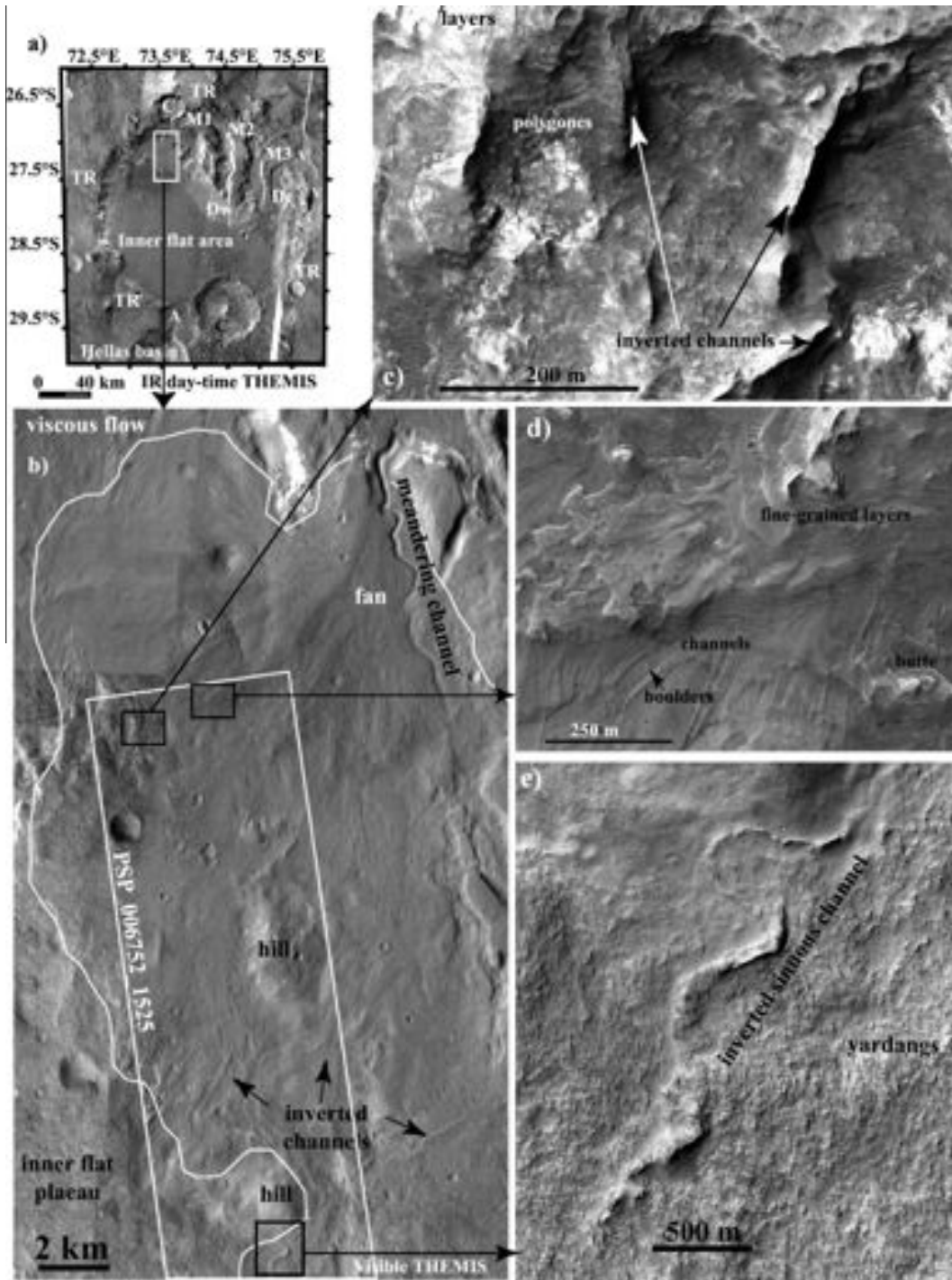


**Fig. 19.** (a) THEMIS day-time image on which white box corresponds to the location of the studied area. (b) Visible THEMIS image on alluvial fan cut by meandering channels, and viscous flows in the upper left corner of image. White box corresponds to the location of the HiRISE image PSP\_006752\_1525 from which are extracted zooms: (c) Distal area of alluvial fan with fine-grained layers covering inverted channels. Some layers are fractured by polygons. (d) Internal sedimentary deposits of alluvial fan. (e) Meanders of an inverted channel of an old alluvial fan. Sedimentary deposits on each side are eroded by wind-abrasion forming small yardangs.

typical of volcanoes was observed, neither was dike inside layers that would suggest local volcanic activity.

Finally, landslides could partially fill the Terby impact crater, explaining the presence of layers in only one side of the crater. Thick landslides have been observed on Mars in the Valles Marineris area (e.g., Lucchitta, 1978; Quantin et al., 2004), and they have a typical shape with grooves and strong internal cohesion. However, no internal layering has ever been reported and typical topographic profiles are concave. Here, no geomorphic feature (e.g., alcove scarp on the Terby inner impact rim with lobate deposition at

its bottom) attests this hypothesis, and the internal geometry of the layers is totally incompatible with mass wasting which should create massive deposits with large rocks embedded in the slump as breccia. Therefore, no alternative hypothesis explains the geometry as well as the sub-aqueous fan deposition.

5.2. Scenario of Terby crater filling and erosion

Based on these results, a geologic scenario can be proposed (Fig. 21). After the formation of the Terby crater during the Early

**Table 3**  
Cumulative crater count.

	Day-time IR Themis (~100 m pixel <sup>-1</sup> )	
	Terby crater area	Terby filling
Surface (km <sup>2</sup> )	48,709	20,252
$N(16)/10^6$ km <sup>2</sup>	201 ± 64	27 ± 36
$N(5)/10^6$ km <sup>2</sup>	324 ± 81	125 ± 78
$N(2)/10^6$ km <sup>2</sup>	693 ± 119	422 ± 144
$N(1)/10^6$ km <sup>2</sup>	2438 ± 223	1804 ± 298
Martian period <sup>a</sup>	Hesperian/Noachian	Hesperian

<sup>a</sup> Tanaka (1986).

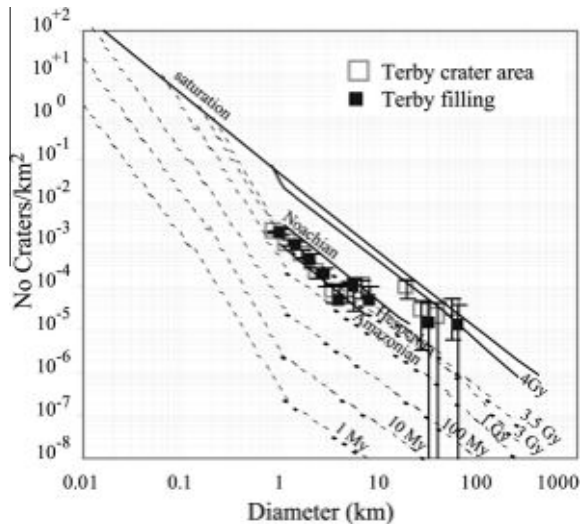


**Fig. 20.** Crater density on the Terby impact crater based on the IR night-time THEMIS images. The isochrones are derived from Hartmann and Neukum (2001). The top solid line corresponds to the saturation equilibrium level, and the short solid lines correspond to period boundaries defined by Tanaka (1986) between Amazonian (bottom), Hesperian (middle) and Noachian (top). The empty squares correspond to craters counted on the area covered by whole day-time IR THEMIS image (48,709 km<sup>2</sup>) seen in Fig. 1. The solid squares correspond to craters counted on the Terby filling including mesas, inner flat area and closed depressions and covering a surface of 20,252 km<sup>2</sup>.

Noachian (Fig. 21a), the crater rim was submitted to an intense degradation, likely runoff, leading to the formation of an interior lake (Fig. 21b). Erosional products were deposited, preferentially, in sub-aqueous fans at the northern rim of the crater, likely where river outlets joined the crater, as suggested from the local presence of a valley (mesa M2) and a regional slope from north to south. The water filling of Terby crater would have been discontinuous with episodes of drying, leading to salts enrichment of lake water (brine) to evaporite environments (e.g. sebkha or playa) which hydrated minerals observed at the bottom of mesas are markers. During the relatively fresh water episode of lake, lacustrine fine-grained sediments were deposited in the central area (Fig. 21b), composing the basal, sub-horizontal light-toned layers observed on the northern cliff of the inner flat area of the Terby crater (Fig. 17).

As the Terby impact crater was progressively filled with water, sedimentary filling continued from several sub-aqueous fan depositional sequences, locally bearing hydrated minerals with phyllosilicates present at the top of several stratigraphic units and likely transported from the region north of Terby (Fig. 21b). Owing to the geometry of layers inside different mesas, we propose that either there was one single sub-aqueous fan (with one main feeding river), whose deposits changed in location during the different sedimentary sequences, or that there were several sub-aqueous fans

(with several feeding valleys), whose sedimentary deposits could be inter-fingered. Whatever the interpretation, fan sedimentary deposits prograded southwards, towards the center of the Terby impact crater, explaining the length (60 km) and thickness (>2 km) of layered deposits. Sediments were likely deposited at varying water lake levels (Fig. 21c), due to the presence of unconformities observed in different locations within mesas (Fig. 12) bounding sedimentary units and due to inverted channels inter-fingered in sub-aqueous fan sedimentary deposits (Fig. 16). The latter are observed close to the Terby impact rim (i.e., within the proximal area of the alluvial/sub-aqueous fan). In addition, the mineralogic study of the mesa M1 shows the presence of a mixing of phyllosilicates and possibly sulfates in sub-horizontal layers in the last stratigraphic units T5/T6 at the summit of the mesa (Fig. 12). The formation of sulfates could be explained either by precipitation of brines in shallow water behind emerged lands (implying that the shoreline was displaced toward the center of Terby), or they formed in hyper-saturated deep lake water, which terrestrial analog could be the Castile formation in Guadalupe mountains, TX (Kirkland et al., 2000). A third scenario could be envisaged by a late sulfate precipitation by a secondary process caused by groundwater level change. The timing of the water/sedimentary filling is difficult to constrain more precisely than to the Late Noachian and Early Hesperian, as indicated by crater counts in the inner filling dating this unit to approximately the Early to Late Hesperian transition.

After the Early Hesperian, the lake dried out (Fig. 21d). Deposits were submitted to erosion, possibly glacial erosion (Wilson et al., 2007) or dissolution (Ansan et al., 2005), and formed the three mesas separated by the closed depressions Dw and Dc. The erosion process remains uncertain. A late episode of fluvial activity is recorded on the inner slopes of the Terby impact crater (Fig. 21e): shallow valleys incised the eastern rim and the inner flat area of the Terby impact crater, and the alluvial fans formed on its north-western side (Fig. 19). Minor fluvial activity occurred likely during the end of Early Hesperian, or during the Late Hesperian since the activity was subsequent to the crater floor filling. This fluvial activity may be similar to that having formed alluvial fans in other impact craters at the northern boundary of the Hellas basin (Moore and Howard, 2005).

More recently, since the end of the Late Hesperian or at the beginning of the Amazonian period, the Terby impact crater was submitted to wind-abrasion and deposition, and frost/defrost processes, as shown by dunes, yardangs, polygons, and ice-rich viscous flows (Fig. 21f). This last step is consistent with previous work (Wilson et al., 2007). However, the activity has no apparent relationship with the initial sedimentary filling.

## 6. Discussion

### 6.1. Origin and composition of the sedimentary filling

The origin of layers as remnants of ancient deltaic sediments implies that these layers are mainly composed of clastic sediments. Layers have various induration and show a response to weathering (such as fractures and aeolian grooves, Fig. 7c and d) indicating that they are not homogeneous in lithology. The high spatial resolution in HiRISE images is still insufficient to observe the detailed sedimentary facies of each layer (laminae, grain size, and internal geometry) limiting our interpretation in terms of sedimentary context. Nevertheless, two sets of information do exist regarding layer lithology: (i) the dip of strata and (ii) the mineralogy detected from NIR spectral data.

Usually on Earth, the clastic sediments observed in deltaic formations are composed of coarse-grained material (Reading, 1996), from cobble-size materials to sand-size particles. Since a

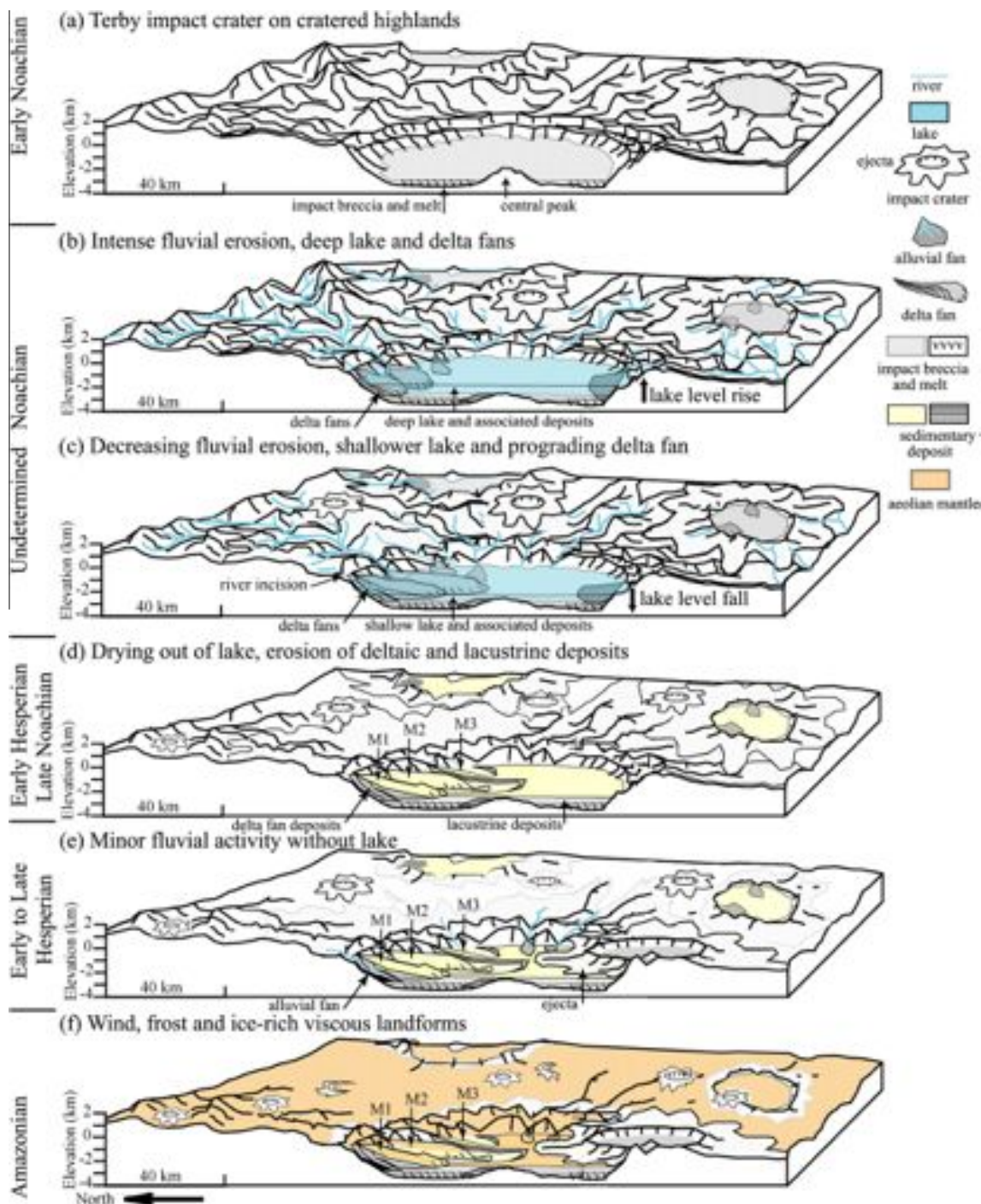


**Fig. 21.** Geologic history of Terby impact crater. Different key steps are shown on the cartoons based on the actual topography for the Amazonian period. See the text for more details (Section 5.2).

decrease in granulometry generates a decrease in the foreset beds dip in gravity-dominated transport (Reading, 1996), the foresets observed in mesas with dips in between  $6^\circ$  and  $10^\circ$  should be predominantly composed of sand-size particles. Gently dipping to horizontal bottomset beds would be dominated by fine-grained particles (silt and clay size particles  $<62 \mu\text{m}$  in diameter, Reading, 1996), as well as by the central inner flat area of the Terby crater corresponding to lacustrine deposits. The presence of dipping strata also implies that water flows of the same density entered into a lake. In this dynamic setting, mud deposits are rare on Earth except in brackish water in which mud deposition is favored by flocculation, but the geometry of deposit is quite different of dipping lay-

ers. Mud decantation exists in the distal or pro-delta area of lacustrine delta as observed in the Selenga delta and in Lake Baikal, southern Siberia (e.g., Coleman et al., 1994; Fagel et al., 2007), where there is little or no water flow. In addition, this sedimentary architecture with sand/silt to shale particles is usual in terrestrial relatively deep-water fans (Posamentier and Venkatarathnan, 2003), where grain sorting is a main process.

On Earth, the presence of clay-sized particles in aqueous deposits generally involves the presence of clay minerals (i.e. phyllosilicates). From a mineralogical point of view, only the uppermost layers of mesas M1 and M2 have phyllosilicate signatures (Fig. 12). Based on our geological cross-sections, these phyllosilicates belong to

two distinct stratigraphic units for mesa M1 (S3 older than T6). Phyllosilicates also display a slight difference in spectral bands depending on mesas (a slight difference in the Fe/Mg band at 2.3  $\mu\text{m}$ ), suggesting that their material source was different (Fig. 12). Both observations suggest that phyllosilicates were formed upstream, transported, and deposited in the Terby impact crater at distinct depositional periods. These phyllosilicates are also located on sub-horizontal layers corresponding to topset or bottomset beds, the latter being a classical situation with regards to the deposition of phyllosilicates in deltas on Earth. Nevertheless, syn-depositional *in situ* alteration cannot be excluded, and may have contributed to the presence of phyllosilicates in distinct layers.

At the base of mesas hydrated minerals have been identified without a more precise determination for their mineralogic family (Fig. 12), although sulfates are possible (Carter et al., 2010). Our hypotheses concerning their composition include the following: (i) phyllosilicates that would have settled in bottomsets of early pro-deltas, or in early lacustrine deposits; (ii) hydrated sulfates that would have formed in early intermittent lakes or sebkhas; and/or (iii) zeolites or hydrated silicates, that would have formed by diagenesis after deposition and compaction. The second environmental setting is intriguing since the presence of evaporite salts/sulfates could explain the present-day morphology of closed depressions at the mesa bottoms (Ansan et al., 2005) and the origin of fold or diapir in the mesa M1 (Fig. 10). Indeed, no secondary deposit was observed in the closed depressions that would correspond to the partial erosion of the mesa suggesting that processes involving chemical dissolution are good candidates for explaining the volume of vanished material.

In summary, deposits are mainly clastic, with phyllosilicates collected in several layers of muddier components, or as the matrix of sand size grains without more details about their context of formation. The difference in mineralogy and texture between layers suggests that the source area for this material is not homogeneous and that it varied during deposition.

## 6.2. Architecture of the sub-aqueous fan: sedimentary supply versus lake-level location

Based on the layer organization, sedimentary filling in the northern part of the Terby impact crater can be interpreted as sub-aqueous fan complex deposits, formed as an alluvial channel entered a standing body of water which deposited its sediments inside (Galloway, 1975; Reading, 1996). On Earth the sedimentary architecture of a sub-aqueous fan is controlled by the following three main factors: (i) tectonics – this factor is absent in the studied area; (ii) water level; and (iii) the sedimentary supply. Hereafter, we explore the possibility for sedimentary sequences to provide more details regarding the variation of water level in the lake filling Terby impact crater.

Several depositional sequences have been identified by erosive surfaces or unconformities, suggesting that the sediment supply was not constant in volume and/or that the relative lake-level changed. On Earth, prograding sub-aqueous fans result from a combination of a high sediment supply from rivers and lake-level highstands, allowing sub-aqueous fans to step toward the basin center (e.g., Galloway, 1975; Posamentier et al., 1988; Reading, 1996). In contrast, as lake-level falls, the deltaic deposits may be removed. If the sediment supply is sufficiently high as the lake-level rises, the superposition of prograding and aggrading fan deltas is possible and they form thick stacked delta wedges. On Earth this vertically-stacked architecture of the fan delta is controlled essentially by tectonic subsidence (e.g., Colella, 1988; Gawthorpe et al., 1994) which does not apply to the Terby crater. Therefore, water level drops and rises, as well as the fluvial supply, may be controlled mainly by climatic variations.

In the mesa M1, where the geometry of layers is well constrained, stratigraphic units Rx, Sx, and Tx were identified (Figs. 12 and 22). The units R0–R5 are close to the Terby impact rim, and they are the oldest ones with R0 being the first deposited, showing an obvious progradation of the sub-aqueous fan southward (foresets) during at least four distinct sedimentary cycles. Stratigraphic units overlap (onlaps and downlaps) each other, indicating that there was an initial phase of aggradation (vertical stacking).

The stratigraphic units S1 and T2 could belong to the same formation step labeled VI (Fig. 22), moving the sub-aqueous fan front 25 km southward (progradation step). The S1 unit would then correspond to a sub-aqueous fan front, indeed, the easiest explanation for the fold may be a mud diapir or a mudlump which usually forms at the toe of the foresets (Coleman, 1988). T2 would then correspond to the fan fine-grained bottomsets passing laterally into lakebed sediments. Alternatively, the hypothesis of a salt diapir is also possible.

After sequence VI, the sub-aqueous fan front was submitted to erosion, as shown by the strong unconformity presumably due to a lake-level drop. After the water level rose again, the stratigraphic units S2 and T3 would then belong to the same deposition step VII, and would correspond to fine-grained bottomsets of another prograding sub-aqueous fan. Foreset beds of this delta are located northward, ~35 km from the Terby crater rim and at –2500 m in elevation. The maximum lake level for this sub-aqueous fan would then be –2200 m.

A general erosion occurred subsequently to the sequence VII, leading to the basal concave-upward unconformity as seen in the base of the stratigraphic units S3 and T4 (Fig. 22), presumably due to another lake-level drop. Above this unconformity, stratigraphic units S3 and T4 would belong to the same formation step VIII due to sedimentary features (thin layers eroded by wind containing phyllosilicates, Fig. 12). Therefore, they could correspond to sub-aqueous bottomsets. Unfortunately, the upper part

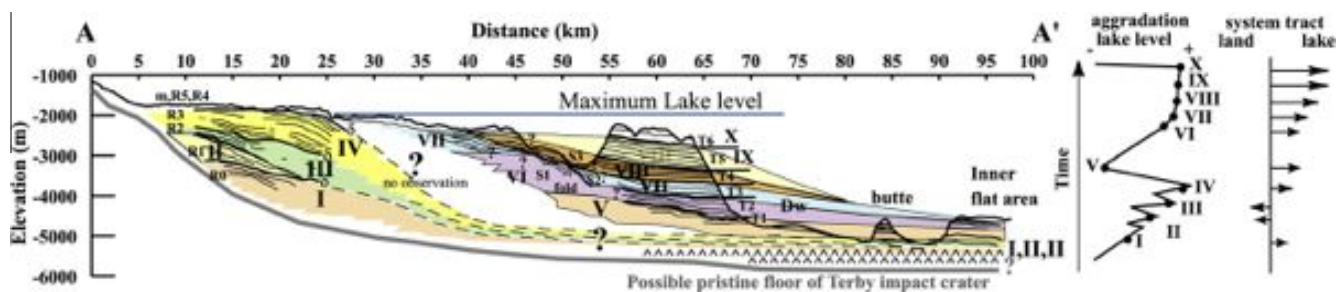


Fig. 22. Stratigraphic sequences of the Mesa M1 with lake levels. Each sequence is underlined by different colors, and labeled in reference to its formation stage. At the center, the relative lake levels associated to the fan aggradation stage are plotted. Lake level is deduced from unconformity locations and the topset–bottomset inflexion for the youngest sequence. On the right, the relative fan progradation toward the center of the Terby lake.

of this delta is absent in the cross-section due to subsequent erosion. Step VIII would be formed during a progressive lake-level rise (Fig. 22).

Stratigraphic units T5 and T6 display a change in sedimentary deposition (Figs. 12 and 22), with a series of meter-scale layers. Due to low dipping and a lack of clinofolds here, their interpretation is difficult. They could correspond to either sub-aqueous fan bottomsets containing phyllosilicates involving an increase in sediment supply, or to sub-aqueous topsets with coarse-grained particles in a phyllosilicate matrix involving a high lake-level (–2000 m in elevation) and lake surface regression. In this hypothesis, the formation of undetermined hydrated minerals like sulfates (Carter et al., 2010) would be explained by the shallow water precipitation behind emerged lands. Alternatively, these last clastic deposits could also correspond to “deep-water” fans that are usually composed of condensed sections that accumulate as drapes of mud (Loutit and Kennett, 1981; Galloway, 1989). However the presence of sulfates could indicate that the deep lake would be filled by a “hyper-saturated” brackish water, as observed in Castile formation in Guadalupe mountains (Kirkland et al., 2000).

In addition, the vertical-stacking architecture of these deltas in the Terby impact crater is also complex in plan view since the summit of the three mesas is standing at different elevations and decreasing eastward (Fig. 1) suggesting that these sub-aqueous fans changed in morphology, in type, and in the location of sediment input over time as they matured and as processes such as river input, lake level, and morphology varied. The best terrestrial example is the Mississippi that changes morphological patterns (lobate to birdfoot), and switches its depositional settings with a typical periodicity on the order of 1500 years (Coleman, 1988). Even if we do not know the original morphology of the lacustrine fans in the Terby impact crater, we can infer that there were one or several switches in sediment depositional settings (i.e., the mesa M1 is the highest area showing a sub-aqueous fan sedimentary organization). However, the stratigraphic correlation between different mesas is difficult without more detailed data.

In summary, the Terby fan delta likely formed by successive depositional stages with progradation and aggradation processes that lead to the formation of a complex and composite sub-aqueous fan. The architecture is interpreted to be controlled by several water lake-level fluctuations (Fig. 22) that developed over a minimum of ten depositional sequences. The progradation of a sub-aqueous fan occurred in at least five stages (Fig. 22, sequences III, V–IX), separated by lake-level falls marked by unconformities. The prograding sequences displayed a relative passive lake restriction that could be associated with a shift in facies and in depositional setting. The vertical stacking of sub-aqueous fans indicates that sedimentary deposition was constrained by lake-level rise, probably together with climate controlled reductions in sediment supply and/or due to modifications in the runoff/evaporation budget.

### 6.3. Implications for paleolake levels

A lake in the Terby crater during the Noachian/Early Hesperian period could occur coeval with other paleolakes that have been identified inside of martian impact craters (e.g., De Hon, 1992; Lucchitta et al., 1992; Scott et al., 1995; Newsom et al., 1996; Grin and Cabrol, 1997; Zimbelman, 1998; Cabrol and Grin, 1999, 2000, 2002; Ansan and Mangold, 2004; Mangold and Ansan, 2006; Wilson et al., 2007; Fassett and Head, 2008). Based on the architecture of overlapping stacked sub-aqueous fans, several vertical changes in lake level have been determined, with a maximum possible elevation for the lake level at –2000 m (Fig. 22) involving a high volume of liquid water as for open-basin lakes (Fassett and Head, 2008).

If we assume that the current topography of the southern rim was the one that existed during the Terby sub-aqueous fan formation, at

a maximum level of –2000 m, the lake would not be bounded by the Terby depression, but would extend far southward to the Hellas basin, submerging the entire depression. Indeed, the current southern Terby rim is >100 m lower than the top of the mesa M1, a possibility that has already been suggested by different authors (Moore and Wilhelms, 2001; Wilson et al., 2007). However, this issue may not be necessary for our scenario. Terby filling resembles a closed basin, especially in light of the very flat inner area for the Terby impact crater (lacustrine deposits) and the lack of apparent deposits over the southern rim. Indeed, the central peak crater with olivine-bearing materials suggests that it is excavated by the crust at a location where no sedimentary deposition is present.

To solve this question, we propose that the southern Terby impact rim was higher than the current elevation (>100 m at least), although it was degraded and its degradation continued after the formation of most sub-aqueous fan deposits. The origin of this degradation is difficult to identify as runoff erosion, impact craters, or glacial weathering and subsequent mass wasting may be possible, because the complex impact crater removed all evidence. The erosion could have occurred at the time of mesa erosion. Similar erosion could have also removed part of the northern rim explaining late alluvial fans. The presence of the central peak crater and its ejecta over the southern rim limits any observation that could be relevant for a better understanding of this hypothesis.

### 6.4. Feeding valley

One question remains concerning the hydrologic system in the Terby crater: Why are feeding valleys so poorly visible? The high volume of sediments filling the Terby crater requires a widespread fluvial catchment area. Only a few valley networks are detected in the cratered highlands north of the Terby crater. A poorly visible residual valley of approximately 10 km wide and 500 m high is observed at the head of mesa M2 (Fig. 13). The valley stands at the same elevation (–1500 m) as the plain located to the north of Terby crater and cross-cut the Terby impact rim. Unfortunately, only its outlet is visible, but this outlet is located at higher elevation than the summit of mesa M1, and the plain upstream is relatively flat suggesting sedimentary fillings that could correspond to alluvial deposits.

In addition, the terrain north of the Terby crater has been submitted to strong erosion by fluvial processes (Hynek and Phillips, 2001; Craddock and Howard, 2002; Howard et al., 2005). The northern region of the Terby impact crater, Tyrrhena Terra, is characterized by widespread hilly terrains with fluvial channels (Nh), and highly cratered and dissected terrains (Npld and Npl1) dated to the Noachian (Leonard and Tanaka, 2001). The latter includes numerous large impact craters that are filled by volcanic and sedimentary deposits, dated of the Noachian–Hesperian boundary up to the Hesperian (e.g., Millichau crater, Mest and Crown, 2005) as well as other unnamed craters (Korteniemi et al., 2005; Moore and Howard, 2005). A northern source of sediment is also supported by OMEGA spectral data by the presence of phyllosilicates and hydrated minerals in Tyrrhena Terra (Poulet et al., 2005; Loizeau et al., 2009).

On Earth, sediments of inactive fan deltas are often preserved without their fluvial catchment area being preserved. For example, the Pliocene Gilbert-deltas near Ventimiglia, NW Italy (Breda et al., 2007) now stand several hundreds of meters above sea level without showing feeding valleys (Fig. 23). By analogy, Noachian terrains surrounding Hellas are strongly modified, especially by later Hesperian volcanic activity (Leonard and Tanaka, 2001), as well as by subsequent aeolian/glacial erosion and filling (Wilson et al., 2007). Valleys can quickly be degraded by such filling or erosion, while thick sediments are partially preserved. Thus, the lack of clearly visible valley networks debouching into the Terby impact crater does not exclude that an ancestral fluvial activity occurred there with only small remnants being visible today.

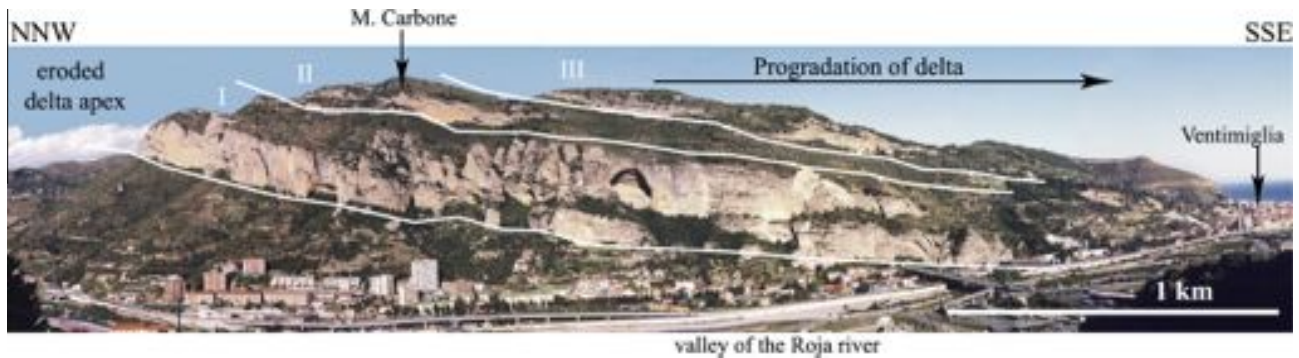


**Fig. 23.** Panoramic view of a vertically stacked Pliocene Gilbert-type delta of Ventimiglia (NW Italy). Three different stratigraphic sequences, labeled I–III, prograding toward the Mediterranean sea. The delta apex and its associated feeder valley are eroded. Photo by Breda et al. (2007).

### 6.5. Implications of the thick sedimentary deposits

The presence of relatively preserved, widespread sub-aqueous fans with a large volume of sediments ( $>5000 \text{ km}^3$ ) in the Terby impact crater raises questions regarding its uniqueness and singularity. The volume is important as compared with other martian fan deltas (e.g.,  $5 \text{ km}^3$  for the Jezero fan (Fassett and Head, 2005),  $6 \text{ km}^3$  for the Eberswalde fan (Malin and Edgett, 2003),  $9.4 \text{ km}^3$  for the Sabrina fan (Hauber et al., 2009), and  $150 \text{ km}^3$  for the Hypanis fan (Hauber et al., 2009)). The Terby sub-aqueous fan is the thickest fan yet identified at the surface of Mars. The volume is also important as compared to the highest terrestrial lacustrine deltas. For example, the active Selenga delta that covers an area of  $\sim 1500 \text{ km}^2$  with a mean sedimentary thickness of 200 m (Urabe et al., 2004), has approximately  $300 \text{ km}^3$  of deposits, since the last 100,000 years. However, it is comparable to several marine terrestrial delta fans (e.g., Mississippi, Niger, and Nile) and deep-water fans (e.g., Niger, Nile, Congo, and Zaire).

Previously cited martian fan deltas have durations estimated at either thousands to millions of years old, if the fluvial flow was quasi-periodic (Moore et al., 2003; Kleinhans, 2005) or to tens of years, if fluvial flow was continuously maintained (Moore et al., 2003; Jerolmack et al., 2004; Kraal et al., 2008). A minimum timescale for Terby deposits can be estimated as for other martian deltas such as for the Jezero that has a sedimentary volume of 500–1000 times less than Terby deposits. By assuming that similar hydrologic conditions existed during the formation of the Terby sub-aqueous fan complex, the minimum duration is expected to be 500 times longer, therefore, from 10,000s years to  $500 \times 10^6$  years. However, this cumulative duration should be taken with caution since the vertical stacking of Terby sub-aqueous fans suggests that sedimentary deposition has occurred in several steps for which we do not yet know the time lapse between occurrences. Nevertheless, the building duration of Terby sub-aqueous fan complex is long, implying that fluvial erosion was maintained over a long period of time. The involved timescale is long on a geologic time scale and the evidence indicates sustained liquid water activity during the early period on Mars.

## 7. Concluding remarks

In terms of structure and process, the stratigraphy of Terby impact crater filling as determined from visible images, thermal data, and topography shows a complex structure of light-toned layers. Terby northern mesas display sediments organized in nine sedimentary sequences, formed by meter-thick layers, at least several hundreds of meters thick. The sequences are limited by unconformities. Several of these sequences show 100 m to 1 km long clino-

forms composed of sub-horizontal topsets, steeply  $6\text{--}10^\circ\text{S}$  dipping foresets and gently dipping to horizontal bottomsets, as uniquely observed on Earth in delta fans. Therefore, the 2 km thick mesas correspond to an accumulation of several sub-aqueous fans, having various sizes and shapes, due to lake-level rises and drops, progradation of sediments toward the crater center, and climate controlled variations in sedimentary supply. In front of the residual fan, several hundreds of meters of horizontal lacustrine deposits have filled the central depression, corresponding to the current inner flat area of the Terby impact crater. The Terby sub-aqueous fan complex is the thickest paleo-deltaic complex observed at the surface of Mars, 100–1000 times more voluminous than delta fans such as those in the Eberswalde or the Jezero craters, suggesting long-term activity with sustained liquid water.

In terms of chronology and mineralogy, crater counts indicate that the Terby impact crater formed during early impact bombardment, after the Hellas Basin formation, during the Noachian period. Despite strong perturbations by unfavorable atmospheric conditions (dust storms, ice clouds, etc.) in this region, hydrated minerals, namely Fe/Mg smectites, were found in three sequences that are located in the uppermost part of the mesas. The altered minerals are preferentially interpreted as being transported from northerly sources of phyllosilicates due to their presence in sequences of a clastic origin, but *in situ* formation is not excluded. In both cases, crater counts in the inner crater filling showed that sedimentary deposition stopped during the Early Hesperian at the latest. Therefore, these deposits accumulated at the same time, or slightly after, the period favoring phyllosilicates formation (Phyllosian, Bibring et al., 2006). From the huge volume of deposits, it is likely that the Terby deposits accumulated over a long duration during the warmer environment of the Noachian/Phyllosian era.

In the Early Hesperian period, a strong erosion of layered deposits predates the accumulation of small alluvial fans that require a late fluvial reactivation. The late fluvial activity may correspond to episodes that have already been identified in several locations on Mars, and that have been dated to the Early to Late Hesperian depending upon location (e.g., Cabrol and Grin, 1999; Mangold et al., 2004, 2007; Quantin et al., 2005; Di Achille et al., 2007; Bouley et al., 2009). The process at the origin of layers erosion is difficult to identify, but it may have taken place under a drier, colder environment that could fit the environment postulated for the Theiikian period (Bibring et al., 2006). Indeed, the strong erosion of the mesas could suggest an acidic environment to explain the missing volume of material by partial dissolution. Finally, the whole Amazonian period was dominated by an aeolian activity and water ice deposition under a permanently cold climate, as determined by water ice-bearing viscous landforms. Thus, the Terby impact crater records, at least in one location, the three main periods of time of the geological history on Mars, making the

sedimentary filling of Terby crater one “potential reference geological cross-section” for Mars stratigraphy like layers in Gale crater (Milliken et al., 2010).

## Acknowledgments

We thank Anna Breda (University of Padova, Italy) for the picture of paleo-Gilbert-type delta near Ventimiglia, NW Italy, and helpful discussion. Special thanks to Evelyne Gailhardis for her technical support. We thank two anonymous reviewers for their

comments and constructive point of views. We acknowledge the effort of HRSC, OMEGA and CRISM team members who have contributed to these investigations in the preparatory phases. The Programme National de Planétologie (PNP) of Institut National des Sciences de l’Univers (INSU-CNRS) and the Centre National d’Etude Spatial (CNES) granted French authors.

## Appendix A

### Tables A1–A5.

**Table A1**

Attitude of layers along the cross-section in the Fig. 8c.

pt	Location	Location on cross-section (km)	Strike (clockwise) (°)	Dip (°)	Dip azimuth dip (°)	Apparent dip	True
1	26°52'49"S/73°58'32"E	1.0	N155 ± 30	0.8 ± 2.5	SW		*
2	26°53'18"S/74°2'11"E	3.1	N132 ± 30	2.3 ± 1.0	SW		*
3	26°55'53"S/74°2'31"E	3.6	N164 ± 30	6.3 ± 1.0	SW		*
4	26°56'55"S/74°1'5"E	4.6	N42 ± 30	2.0 ± 0.3	SE	*	
5	26°53'493"S/74°3'19"E	5.9	N135 ± 30	1.2 ± 2.5	SW		*
6	26°58'33"S/74°2'35"E	6.6	N44 ± 30	1.9 ± 0.3	SE	*	
7	26°57'33"S/74°4'2.1"E	7.5	N160 ± 30	5.0 ± 1.5	SW		*
8	26°59'5"S/74°4'3"E	9.5	N51 ± 30	1.9 ± 1.0	SE	*	
9	26°59'11"S/74°8'48"E	14.4	N52 ± 30	0.9 ± 2.0	SE		*
10	27°2'383S/74°9'7"E	15.9	N125 ± 30	6.3 ± 1.0	SW		*

**Table A2**

Attitude of layers along the cross-section in the Fig. 10c.

pt	Location	Location on cross-section (km)	Strike (clockwise) (°)	Dip (°)	Dip azimuth (°)	Apparent dip	True dip
1	27°12'49"S/74°15'11"E	1.1	N80 ± 30	3 ± 0.3	SE	*	
2	27°15'35"S/74°16'5"E	2.1	N129 ± 30	5.1 ± 1.0	SE		*
3	27°17'46"S/74°15'35"E	5.2	N90 ± 30	1.0 ± 1.5	S	*	
4	27°18'58"S/74°17'18"E	5.7	N104 ± 30	1.1 ± 1.5	SW		*
5	27°20'10"S/74°15'51"E	7.5	N86 ± 30	3.4 ± 1.0	S		*
6	27°20'173S/74°15'15"E	8.1	N95 ± 30	10.1 ± 0.3	S	*	

**Table A3**

Attitude of layers in the Fig. 11.

pt	Location	Location on 3D	Strike (clockwise) (°)	Dip (°)	Dip azimuth (°)	Apparent dip	True dip
1	27°33'3"S/74°10'3"E	T1 (Fig. 11f)	N149 ± 30	1.5 ± 1.0	SW		*
2	27°32'31"S/74°10'32"E	T2 (Fig. 11f)	N7 ± 30	5.1 ± 1.0	E		*
3	27°33'58"S/74°13'30"E	T3 (Fig. 11f)	N156 ± 30	2.1 ± 1.0	SW		*
4	27°32'37"S/74°14'273"E	T4 (Fig. 11f)	N90 ± 30	2.4 ± 1.0	S		*
5	27°33'3"S/74°16'33"E	T5 (Fig. 11h)	N51 ± 30	1.9 ± 1.0	SE		*
6	27°32'38"S/74°16'16"E	T6 (Fig. 11h)	N59 ± 30	1.2 ± 1.0	SE		*

**Table A4**

Attitude of layers in the mesa M2.

pt	Location	Location on 3D	Strike (°)	Dip (°)	Dip azimuth (°)	Apparent dip	True dip
1	26°47'443S/74°36'583"E	Toe of scarp (Fig. 14b)	N88 ± 30	1.5 ± 1.0	S		*
2	26°47'47S/74°37'54"E	Scarp (Fig. 14h)	N90 ± 30	5.0 ± 1.5	S	*	
3	26°48'5"S/74°37'55"E	Top of scarp (Fig. 14b)	N90 ± 30	2.0 ± 1.5	S	*	
4	27°24'30"S/74°33'30"E	Top of mesa (Fig. 14d)	N90 ± 30	2.0 ± 1.5	S	*	
5	27°29'0"S/74°30'59"E	Toe of scarp (Fig. 14d)	N100 ± 30	5.0 ± 1.5	SW	*	
6	27°26'14"S/74°43'13"E	Top of mesa (Fig. 15b)	N1 ± 30	2.1 ± 1.5	SE		*
7	27°38'483S/74°37'52"E	Top of mesa (Fig. 15e)	N85 ± 30	1.1 ± 1.0	SE		*
8	27°40'40"S/74°42'45"E	Scarp (Fig. 15e)	N100 ± 30	8.7 ± 1.0	SW	*	
9	27°42'41"S/74°43'17"E	Scarp (Fig. 15e)	N124 ± 30	4.3 ± 1.5	SW	*	
10	27°44'13"S/74°41'493"E	Scarp (Fig. 15e)	N8 ± 30	1.4 ± 1.0	SE	*	
11	27°46'41"S/74°41'44"E	Scarp (Fig. 15e)	N89 ± 30	8.1 ± 1.5	SE	*	
12	27°47'33"S/74°41'49"E	Scarp (Fig. 15e)	N85 ± 30	5.9 ± 1.0	SE		*

**Table A5**

Attitude of layers in the residual buttes and flat area of Terby.

pt	Location	Location on figure	Strike (°)	Dip (°)	Dip azimuth (°)	Apparent dip	True dip
1	27°37'20"S/74°24'35"E	Fig. 17b	N10 ± 30	5.1 ± 1.0	SE	*	*
2	27°40'55"S/74°25'1"E	Fig. 17b	N69 ± 30	2.4 ± 1.5	SE	*	*
3	27°44'10"S/74°25'1"E	Fig. 17b	N75 ± 30	2.0 ± 1.5	SE	*	*
4	27°44'29"S/74°24'6"E	Fig. 17b	N78 ± 30	4.1 ± 1.0	SE	*	*
5	27°44'3"S/74°27'31"E	Fig. 17b	N92 ± 30	2.9 ± 1.5	SW	*	*
6	28°4'373"S/74°37'8"E	Fig. 17c	N102 ± 30	1.0 ± 1.0	SW	*	*
7	28°4'16"S/74°37'57"E	Fig. 17c	N94 ± 30	2.0 ± 1.0	SW	*	*
8	28°1'1"S/74°17'10"E	Fig. 17d	N86 ± 30	1.9 ± 1.0	SE	*	*
9	28°3'11"S/74°17'11"E	Fig. 17d	N81 ± 30	3.9 ± 1.0	SE	*	*

## References

- Akabane, T., Iwasaki, K., Saito, Y., Narumi, Y., 1992. Opacities of the 1973 dust storm over the Solis Llacus, Hellas, and Syrtis Major areas of Mars. *Astron. Astrophys.* 255 (1–2), 377–382.
- Albertz, J. et al., and the HRSC Co-Team, 2005. HRSC on Mars Express – Photogrammetric and cartographic research. *Photogram. Eng. Rem. Sens.* 71 (10), 1153–1166.
- Allen, J.R.L., 1983. Studies in fluvial sedimentation: Bars, bar complexes and sandstone sheets (low sinuosity braided streams) in the Brownstones (L. Devonian), Welsh Borders. *Sediment. Geol.* 33, 237–293.
- Ansan, V., Mangold, N., 2004. Impact crater paleolakes in Hellas and Thaumasia areas, Mars. In: Early Mars Conference, Jackson Hole, USA.
- Ansan, V., Mangold, N., 2006. New observations of Warrego Valles, Mars: Evidence for precipitation and surface runoff. *Planet. Space Sci.* 54, 219–242.
- Ansan, V., Mangold, N., Lucas, A., Gendrin, A., Le Mouelic, S., Poulet, F., Bibring, J.-P., and the OMEGA Co-Investigator Team, 2005. Analysis of layered deposits in Terby crater (Hellas region, Mars) using multiple datasets MOC, THEMIS and OMEGA/MEX data. *Lunar Planet. Sci. XXXVI*, Houston, USA. Abstract #1324.
- Ansan, V., Mangold, N., Lucas, A., 2006. Layered deposits in Terby crater (Hellas region, Mars) from multi-datasets (MOLA, THEMIS AND MOC): Geologic implications. *Lunar Planet. Sci. XXXVII*, Houston, USA. Abstract #1877.
- Ansan, V., Mangold, N., Masson, Ph., Gailhardis, E., Neukum, G., 2008. Topography of valley networks on Mars from the Mars Express High Resolution Stereo Camera Digital Elevation Models. *J. Geophys. Res.* 113, E07006. doi:10.1029/2007JE002986.
- Baker, V.R., Kochel, R.C., 1979. Martian channel morphology: Maja and Kasei Valles. *J. Geophys. Res.* 84, 7961–7983.
- Baker, V.R., Carr, M.H., Gulick, V.C., Williams, C.R., Marley, M.S., 1992. Channels and valley networks. In: Kieffer, H.H. et al. (Eds.), *Mars*. University of Arizona Press, Tucson, pp. 493–522.
- Baratoux, D., Mangold, N., Delacourt, C., Allemand, P., 2002. Evidence of liquid water in recent debris avalanche on Mars. *Geophys. Res. Lett.* 29, 1156. doi:10.1029/2001GL014155.
- Barlow, N.G., 1990. Constraints on early events in martian history as derived from the cratering record. *J. Geophys. Res.* 95, 14191–14201.
- Bibring, J.-P. et al., 2004. OMEGA: Observatoire pour la Minéralogie, l'Eau, les Glaces et l'Activité. In: Wilson, A. (Ed.), *Mars Express: The Scientific Payload*. ESA SP-1240, Noordwijk, Netherlands: ESA Publications Division, pp. 37–49. ISBN 92-9092-556-6.
- Bibring, J.P. et al., 2005. Mars surface diversity as revealed by the OMEGA/Mars Express observations. *Science* 307 (5715), 1576–1581. doi:10.1126/science.1108806.
- Bibring, J.P., Langevin, Y., Mustard, J.F., Poulet, F., Arvidson, R., Gendrin, A., Gondet, B., Mangold, N., Pinet, P., Forget, F., 2006. Global mineralogical and aqueous Mars history derived from OMEGA/Mars express data. *Science* 312 (5772), 400–404. doi:10.1126/science.1122659.
- Bouley, S., Ansan, V., Mangold, N., Masson, Ph., Neukum, G., 2009. Fluvial morphology of Naktong Vallis, Mars: A late activity with multiple processes. *Planet. Space Sci.* 57, 982–999. doi:10.1016/j.pss.2009.01.015.
- Brakenridge, G.R., Newsom, H.E., Baker, V.R., 1985. Ancient hot springs on Mars – Origins and paleoenvironmental significance of small martian valleys. *Geology* 13, 859–862.
- Breda, A., Mellere, D., Massari, F., 2007. Facies and processes in a Gilbert-delta-filled incised valley (Pliocene of Ventimiglia, NW Italy). *Sediment. Geol.* 200, 31–55.
- Cabrol, N.A., Grin, E.A., 1999. Distribution, classification, and age of martian impact crater lakes. *Icarus* 142, 160–172.
- Cabrol, N.A., Grin, E.A., 2000. Recent lakes on Mars. 1st Astrobiology Science Conference. NASA Res. Center. Abstract 199.
- Cabrol, N.A., Grin, E.A., 2002. Overview on the formation of paleolakes and ponds on Mars. *Global Planet. Change* 35, 199–219.
- Cantor, B.A., 2007. MOC observations of the 2001 Mars planet encircling dust storm. *Icarus* 186, 60–96. doi:10.1016/j.icarus.2006.08.019.
- Carr, M.H., 1996. In: Carr, M.H. (Ed.), *Water on Mars*. Oxford Univ. Press, New York, 229pp.
- Carr, M.H., Clow, G.D., 1981. Martian channels and valleys: Their characteristics, distribution, and age. *Icarus* 48, 91–117.
- Carter, J.A., Poulet, F., Bibring, J.-P., Murchie, S., Ansan, V., Mangold, N., 2010. Mineralogy of layered deposits in Terby Crater, N. Hellas Planitia. *Lunar Planet. Sci. XXXXI*. Abstract #1866.pdf.
- Chapman, C.R., 1974. Cratering on Mars. 1. Cratering and obliteration history. *Icarus* 22, 272–291.
- Chicarro, A., Martin, P., Trautner, R., 2004. The Mars Express Mission: An overview. In: Wilson, A. (Ed.), *Mars Express: The Scientific Payload*. ESA SP-1240, Noordwijk, Netherlands: ESA Publications Division, pp. 3–16. ISBN 92-9092-556-6.
- Christensen, P.R. et al., 2001. Mars Global Surveyor Thermal Emission Spectrometer experiment: Investigation description and surface science results. *J. Geophys. Res.* 106 (E10), 23823–23871.
- Christensen, P.R. et al., 2003. Morphology and composition of the surface of Mars: Mars Odyssey THEMIS results. *Science* 300, 2056–2061.
- Clark, R.N., King, T.V.V., Klejwa, M., Swayze, G.A., Vergo, N., 1990. High spectral resolution reflectance spectroscopy of minerals. *J. Geophys. Res.-Solid Earth and Planet.* 95, 12653–12680.
- Clark, R.N., Swayze, G.A., Gallagher, A., King, T.V.V., Calvin, W.M., 1993. The USGS Digital Spectral Library: Version 1: 0.2 to 3.0 microns. *US Geol. Surv. Open File Rep.*, 93-592, 1340pp. <<http://speclab.cr.usgs.gov>>.
- Colella, A., 1988. Pliocene–Holocene fan deltas and braid deltas in the Crati basin, southern Italy: A consequence of varying tectonic conditions. In: Nemeč, W., Steel, R.J. (Eds.), *Fan Deltas*. Sedimentology and Tectonic Setting. Blackie and Son, New York, pp. 50–74.
- Coleman, J.M., 1988. Dynamic changes and processes in the Mississippi River delta. *Geol. Soc. Am. Bull.* 100, 999–1015.
- Coleman, S.M., Carter, J., Hatton, J., Haskel, B.J., 1994. Cores Collected by the US Geological Survey in Lake Baikal, Siberia: Visual Descriptions, Photographs, X-Radiographs, Bulk Density and Grain Size. *US Geological Survey Open-File Report* 94-445, 122pp.
- Craddock, R.A., Howard, A.D., 2002. The case for rainfall on a warm. *Wet Early Mars*. *J. Geophys. Res.* 107 (5111), 1–36.
- Craddock, R.A., Maxwell, T.A., 1993. Geomorphic evolution of martian highlands through ancient fluvial processes. *J. Geophys. Res.* 98, 3453–3468.
- Crown, D.A., Price, K.H., Greeley, R., 1992. Geologic evolution of the east rim of the Hellas basin, Mars. *Icarus* 100, 1–25.
- De Hon, R.A., 1992. Martian lake basins and lacustrine plains. *Earth, Moon, Planets* 56, 95–122.
- Di Achille, G., Ori, G.G., Reiss, D., 2007. Evidence for late Hesperian lacustrine activity in Shalbatana Vallis, Mars. *J. Geophys. Res.* 112, E07007. doi:10.1029/2006JE002858.
- Duxbury, T.C., Kirk, R.K., Archinal, B.A., Neumann, G.A., 2002. Mars geodesy/cartography working group recommendation on Mars cartographic constants and coordinate systems. In: *Symposium on Geospatial Theory, Processing and Application*. Ottawa, p. 4.
- Edgett, K.S., Malin, M.C., 2002. Martian sedimentary rock stratigraphy: Outcrops and interbedded craters of northwest Sinus Meridiani and southwest Arabia Terra. *Geophys. Res. Lett.* 29 (24), 2179. doi:10.1029/2002GL016515.
- Ehlmann, B.L., Mustard, J.F., Fassett, C.I., Schon, S.C., Head, J.W., Desmarais, D.J., Grant, J.A., Murchie, S.L., 2008. Clay minerals in delta deposits and organic preservation potential on Mars. *Nat. Geosci.* 1, 355–358.
- Fagel, N., Thomó-Bózsó, E., Heim, B., 2007. Mineralogical signatures of Lake Baikal sediments: Sources of sediment supplies through late Quaternary. *Sediment. Geol.* 194, 37–59. doi:10.1016/j.sedgeol.2006.04.006.
- Fassett, C.I., Head, J.W., 2005. Fluvial sedimentary deposits on Mars: Ancient deltas in crater lake in Nili Fossae region. *Geophys. Res. Lett.* 32, L14201.
- Fassett, C.I., Head, J.W., 2008. Valley network-fed, open-basin lakes on Mars: Distribution and implications for Noachian surface and subsurface hydrology. *Icarus* 198, 37–56. doi:10.1016/j.icarus.2008.06.016.
- Forget, F., Haberle, R.M., Montmessin, F., Levrard, B., Head, J.W., 2006. Formation of glaciers on Mars by atmospheric precipitation at high obliquity. *Science* 311 (5759), 368–371.
- Galloway, W.E., 1975. Process framework for describing the morphologic and stratigraphic evolution of deltaic depositional systems. In: Broussard, M.L. (Ed.), *Deltas: Models for Exploration*. Houston Geological Society, Houston, pp. 87–98.
- Galloway, W.E., 1989. Genetic stratigraphic sequences in basin analysis. I. Architecture and genesis of flooding-surface bounded depositional units. *AAPG Bull.* 73, 125–142.

- Gawthorpe, R.L., Fraser, A.J., Collier, R.E.L., 1994. Sequence stratigraphy in active extensional basins: Implications for the interpretation of ancient basin-fills. *Mar. Pet. Geol.* 11 (6), 642–658.
- Golombek, M.P., Bridges, N.T., 2000. Erosion rates on Mars and implications for climate change: Constraints from the Pathfinder landing site. *J. Geophys. Res.* 105, 1841–1853.
- Grant, J.A., 2000. Valley formation in Margaritifer Sinus, Mars, by precipitation-recharged ground-water sapping. *Geology* 28, 223–226.
- Grant, J.A., Irwin, R.P., Grotzinger, J.P., Milliken, R.E., Tornabene, L.L., McEwen, A.S., Weitz, C.M., Squyres, S.W., Glotch, S.W., Thomson, B.J., 2008. HiRISE imaging of impact megabreccia and sub-meter aqueous strata in Holden Crater, Mars. *Geology* 36, 195–198.
- Grant, J.A., Wilson, S.A., Cohen, B.A., Golombek, M.P., Geissler, P.E., Sullivan, R.J., Kirk, R.L., Parker, T.J., 2009. Degradation of Victoria crater, Mars. *J. Geophys. Res.* 113, E11010. doi:10.1029/2008JE003155.
- Grin, E.A., Cabrol, N.A., 1997. Limnological analysis of the Gusev crater paleolake, Mars. *Icarus* 130, 416–474.
- Grotzinger, J.P. et al., 2005. Stratigraphy and sedimentology of a dry to wet eolian depositional system, Burns formation, Meridiani Planum, Mars. *Earth Planet. Sci. Lett.* 240 (1), 11–72. doi:10.1016/j.epsl.2005.09.039.
- Gulick, V.C., 2001. Origin of the valley networks on Mars: A hydrological perspective. *Geomorphology* 37, 241–268.
- Gulick, V.C., Baker, V.R., 1989. Fluvial valleys and martian paleoclimates. *Nature* 341, 514–516.
- Gwinner, K., Scholten, F., Jaumann, R., Roatsch, T., Oberst, J., Neukum, G., 2007. Global mapping of Mars by systematic derivation of Mars Express HRSC High-Resolution Digital Elevation Models and orthoimages. ISPRS Commission IV, Working Group 9, Extraterrestrial Mapping Workshop “Advances in Planetary Mapping”, Houston, Texas.
- Hartmann, W.K., 2005. Martian cratering. 8. Isochron refinement and the history of martian geologic activity. *Icarus* 174, 294–320.
- Hartmann, W.K., Neukum, G., 2001. Cratering chronology and the evolution of Mars. *Space Sci. Rev.* 96, 165–194.
- Hauber, E., Gwinner, K., Kleinshans, M., Reiss, D., Di Achille, G., Ori, G.G., Scholten, F., Marinangeli, L., Jaumann, R., Neukum, G., 2009. Sedimentary deposits in Xanthe Terra: Implications for the ancient climate on Mars. *Planet. Space Sci.* 57, 944–957. doi:10.1016/j.pss.2008.06.009.
- Howard, A.D., 1988. Sapping features of the Colorado Plateau. In: Howard, A.D., Kochel, R.C., Holt, H.E. (Eds.), *A Comparative Planetary Geology Field Guide*. NASA SP-491, 108pp.
- Howard, A.D., Moore, J.M., Irwin, R.P., 2005. An intense terminal epoch of widespread fluvial activity on Early Mars: 1. Valley network incision and associated deposits. *J. Geophys. Res.* 110, E12S14. doi:10.1029/2005JE002459.
- Hynek, B.M., Phillips, R.J., 2001. Evidence for extensive denudation of the martian highlands. *Geology* 29, 407–410.
- Irwin, R.P., Howard, A.D., 2002. Drainage basin evolution in Noachian Terra Cimmeria, Mars. *J. Geophys. Res.* 107 (E7), 5056. doi:10.1029/2001JE001818.
- Irwin, R.P., Howard, A.D., Craddock, R.A., Moore, J.M., 2005. An intense terminal epoch of widespread fluvial activity on Early Mars: 2. Increased runoff and paleolake development. *J. Geophys. Res.* 110, E12S15. doi:10.1029/2005JE002460.
- Jakosky, B.M., 1986. On the thermal properties of martian fines. *Icarus* 66, 117–124.
- Jakosky, B.M., Christensen, P.R., 1986. Global dicrusted on Mars: Analysis of remote-sensing data. *J. Geophys. Res.* 91, 3547–3559.
- Jaumann, R. et al., and the HRSC Co-Investigator Team, 2007. The High Resolution Stereo Camera (HRSC) experiment on Mars express: Instrument aspects and experiment conduct from interplanetary cruise through the nominal mission. *Planet. Space Sci.* 55, 928–952. doi:10.1016/j.pss.2006.12.003.
- Jerolmack, D.J., Mohrig, D., Zuber, M.T., Byrne, S., 2004. A minimum time for formation of Holden Northeast fan, Mars. *Geophys. Res. Lett.* 31, L21701. doi:10.1029/2004GL021326.
- Kirkland, D.W., Denison, R.E., Dean, W.E., 2000. Parent brine of the Castile evaporites (Upper Permian), Texas and New Mexico. *J. Sediment. Res.* 70, 749–761.
- Kleinshans, M.G., 2005. Flow discharge and sediment transport models for estimating a minimum timescale of hydrological activity and channel and delta formation on Mars. *J. Geophys. Res.* 110, E12003. doi:10.1029/2005JE002521.
- Korteniemi, J., Kostama, V.P., Törmänen, T., Aittola, M., Öhman, T., Lahtela, H., Raitala, J., Neukum, G., 2005. Complex geology of two large impact craters in Tyrrhena Terra, Mars: Detailed analysis using MEX HRSC camera data. *J. Geophys. Res.* 110 (E12), E12S18. doi:10.1029/2005JE002427.
- Kraal, E.R., van Dijk, M., Postma, G., Kleinshans, M.G., 2008. Martian stepped-delta formation by rapid water release. *Nature* 451, 973–976.
- Leonard, G.J., Tanaka, K.L., 2001. Geologic map of the Hellas Region of Mars, scale 1:5000,000, USGS Geologic Investigations Series I-2694.
- Lewis, K.W., Aharonson, O., 2006. Stratigraphic analysis of the distributary fan in Eberswalde crater using stereo imagery. *J. Geophys. Res.* 111, E06001. doi:10.1029/2005JE002558.
- Loizeau, D. et al., 2007. Phyllosilicates in the Mawrth Vallis region of Mars. *J. Geophys. Res.* 112, E08S08.
- Loizeau, D. et al., 2009. Tyrrhena Terra: Hydrated lobate ejecta and plains. *Lunar Planet. Sci. XXXX*. Abstract #2010.
- Loutit, T.S., Kennett, J.P., 1981. New Zealand and Australian cenozoic sedimentary cycles and global sea-level changes. *AAPG Bull.* 65, 1586–1601.
- Lucchitta, B.K., 1978. Large landslide on Mars. *Geol. Soc. Am. Bull.* 89 (11), 1601–1609.
- Lucchitta, B.K., McEwen, A.S., Clow, G.D., Geissler, P.E., Singer, R.B., Schultz, R.A., Squyres, S.W., 1992. In: Kieffer, H.H. et al. (Eds.), *The Canyon System on Mars*. Univ. of Arizona Press, Tucson, USA, pp. 453–492.
- Malin, M.C., Edgett, K.S., 2000. Sedimentary rocks of Early Mars. *Science* 290, 1927–1937.
- Malin, M.C., Edgett, K.S., 2003. Evidence for persistent flow and aqueous sedimentation on Early Mars. *Science* 302, 1931–1934.
- Malin, M.C. et al., 1998. Early views of the martian surface from the Mars Orbiter Camera of Mars Global Surveyor. *Science* 279, 1681–1685.
- Mangold, N., 2003. Geomorphic analysis of lobate debris aprons on Mars at Mars Orbiter Camera scale: Evidence for ice sublimation initiated by fractures. *J. Geophys. Res.* 108 (E4), 8021. doi:10.1029/2002JE001885.
- Mangold, N., Ansan, V., 2006. Detailed study of an hydrological system of valleys, a delta and lakes in the Southwest Thaumasia region, Mars. *Icarus* 180, 75–87.
- Mangold, N., Quantin, C., Ansan, V., Delacourt, C., Allemand, P., 2004. Evidence for precipitation on Mars from dendritic valleys in the Valles Marineris area. *Science* 305, 78–81.
- Mangold, N. et al., 2007. Mineralogy of the Nili Fossae region with OMEGA/Mars Express data: 2. Aqueous alteration of the crust. *J. Geophys. Res.* 112, E08S04. doi:10.1029/2006JE002835.
- Mars Channel Working Group, 1983. Channels and valleys on Mars. *Geol. Soc. Am. Bull.* 94, 1035–1054.
- Martin, L.J., 1974. The major martian dust storms of 1971–1973. *Icarus* 23, 108–115.
- McEwen, A.S. et al., 2007. Mars Reconnaissance Orbiter's High Resolution Imaging Science Experiment (HiRISE). *J. Geophys. Res.* 112, E05S02. doi:10.1029/2005JE002605.
- McKim, R., 1996. The dust storms on Mars. *J. Br. Astron. Assoc.* 106, 185–200.
- Mellon, M.T., Jakosky, B.M., Kieffer, H.H., Christensen, P.R., 2000. High-resolution thermal inertia mapping from the Mars Global Surveyor Thermal Emission Spectrometer. *Icarus* 148, 437–455.
- Mest, S.C., Crown, D.A., 2005. Millochau crater, Mars: Infilling and erosion of an ancient highland impact crater. *Icarus* 175, 335–359.
- Metz, J.M., Grotzinger, J.P., Mohrig, D., Milliken, R., Prather, B., Pirmez, C., McEwen, A.S., Weitz, C.M., 2009a. Sublacustrine depositional fans in southwest Melas Chasma. *J. Geophys. Res.* 114, E10002. doi:10.1029/2009JE003365.
- Metz, J.M., Grotzinger, J.P., Rubin, D.M., Lewis, K.W., Squyres, S.W., Bell, J.F., 2009b. Sulfate-rich eolian and wet interdune deposits, Erebus crater, Meridiani Planum, Mars. *J. Sediment. Res.* 79 (5–6), 247–264. doi:10.2110/jsr.2009.033.
- Milliken, R.E., Bish, D.L., 2010. Sources and sinks of clay minerals on Mars. *Philos. Mag.* 90 (17), 2293–2308.
- Milliken, R.E., Mustard, J.F., 2005. Quantifying absolute water content of minerals using near-infrared reflectance spectroscopy. *J. Geophys. Res.* 110 (E12), E12001. doi:10.1029/2005JE002534.
- Milliken, R.E., Mustard, J.F., Goldsby, D.L., 2003. Viscous flow features on the surface of Mars: Observations from high-resolution Mars Orbiter Camera (MOC) images. *J. Geophys. Res.* 108 (E6), 5057. doi:10.1029/2002JE002005.
- Milliken, R.E., Grotzinger, J., Murchie, S., Grant, J.A., and the CRISM Team, 2007. Evidence for hydrated phyllosilicates in Holden Crater, Mars using hyperspectral CRISM data. *Lunar Planet. Sci. XXXIII*. Abstract #1913.
- Milliken, R.E., Grotzinger, J.P., Thomson, B.J., 2010. Paleoclimate of Mars as captured by the stratigraphic record in Gale Crater. *Geophys. Res. Lett.* 37, L04201. doi:10.1029/2009GL041870.
- Milton, D.J., 1973. Water and processes of degradation in the martian landscape. *J. Geophys. Res.* 78, 4037–4047.
- Mitchum Jr., R.M., 1977. Seismic stratigraphy and global changes of sea level. Part 11: glossary of terms used in seismic stratigraphy. In: Payton, C.E. (Ed.), *Seismic Stratigraphy—Applications to Hydrocarbon Exploration*, vol. 26. A.A.P.G. Memoir, pp. 205–212.
- Moore, J.M., Howard, A.D., 2005. Large alluvial fans on Mars. *J. Geophys. Res.* 110, E04005. doi:10.1029/2004JE002352.
- Moore, J.M., Wilhelms, D.E., 2001. Hellas as a possible site of ancient ice-covered lakes on Mars. *Icarus* 154, 258–276.
- Moore, J.M., Howard, A.D., Dietrich, W.E., Schenk, P.M., 2003. Martian layered fluvial deposits: Implications for Noachian climate scenarios. *Geophys. Res. Lett.* 30 (24), 2292. doi:10.1029/2003GL019002.
- Morgan, J.P., Coleman, J.M., Gagliano, S.M., 1968. Mudlumps: Diapiric structures in Mississippi delta sediments, in Diapirism and diapirs. *Am. Assoc. Petrol. Geol. Mem.* 8, 145–161.
- Murchie, S. et al., 2007. Compact Reconnaissance Imaging Spectrometer for Mars (CRISM) on Mars Reconnaissance Orbiter (MRO). *J. Geophys. Res.* 112, E05S03. doi:10.1029/2006JE002682.
- Murchie, S.L. et al., 2009. Compact Reconnaissance Imaging Spectrometer for Mars investigation and data set from the Mars Reconnaissance Orbiter's primary science phase. *J. Geophys. Res.* 114, E00D07. doi:10.1029/2009JE003344.
- Mustard, J.F. et al., 2008. Hydrated silicate minerals on Mars observed by the Mars reconnaissance orbiter CRISM instrument. *Nature* 454, 305–309. doi:10.1038/nature07097.
- Neukum, G., Jaumann, R., and HRSC Co-Investigator Team, 2004. HRSC: The High Resolution Stereo Camera of Mars Express. In: Wilson, A. (Ed.), *Mars Express: The Scientific Payload*. ESA SP-1240, Noordwijk, Netherlands: ESA Publications Division, pp. 17–36. ISBN 92-9092-556-6.
- Newsom, H.E., Brittelle, G.E., Hibbits, C.A., Crossey, L.J., Kudo, A.M., 1996. Impact crater lakes on Mars. *J. Geophys. Res.* 101, 14951–149551.
- Ori, G.G., Marinangeli, L., Baliva, A., 2000. Terraces and Gilbert-type deltas in crater lakes in Ismenius Lacus and Memnonia (Mars). *J. Geophys. Res.* 105 (E7), 17629–17641.

- Peterfreund, A.R., Kieffer, H.H., 1979. Thermal infrared properties of the martian atmosphere. 3. Local dust storms. *J. Geophys. Res.* 84, 2853–2863.
- Pierce, T.L., Crown, D.A., 2003. Morphologic and topographic analyses of debris aprons in the eastern Hellas region, Mars. *Icarus* 163, 46–65.
- Pieri, D.C., 1980. Martian valleys: Morphology, distribution, age and origin. *Science* 210, 895–897.
- Pondrelli, M., Baliva, A., Di Lorenzo, S., Marinangeli, L., Rossi, A.P., 2005. Complex evolution of paleolacustrine systems on Mars: An example from Holden crater. *J. Geophys. Res.* 110, E04016. doi:10.1029/2004JE002335.
- Pondrelli, M., Rossi, A.P., Marinangeli, L., Hauber, E., Gwinner, K., Baliva, A., Di Lorenzo, S., 2008. Evolution and depositional environments of the Eberswalde fan delta, Mars. *Icarus* 197, 429–451. doi:10.1016/j.icarus.2008.05.018.
- Posamentier, H.W., Venkatarathnan, K., 2003. Seismic geomorphology and stratigraphy of depositional elements in deep-water settings. *J. Sediment. Res.* 73, 367–388.
- Posamentier, H.W., Jervey, M.T., Vail, P.R., 1988. Eustatic controls on clastic deposition. I. Conceptual framework. In: Wilgus, C.K., Hastings, B.S., Kendall, C.G., St. C., Posamentier, H.W., Ross, C.A., Van Wagoner, J.C. (Eds.), *Sea Level Changes—An Integrated Approach*, vol. 42. SEPM Special Publication, pp. 110–124.
- Poulet, F., Bibring, J.P., Mustard, J.F., Gendrin, A., Mangold, N., Langevin, Y., Arvidson, R.E., Gondet, B., Gomez, C., 2005. Phyllosilicates on Mars and implications for early martian climate. *Nature* 438 (7068), 623–627.
- Poulet, F., Gomez, C., Bibring, J.-P., Langevin, Y., Gondet, B., Pinet, P., Belluci, G., Mustard, J., 2007. Martian surface mineralogy from Observatoire pour la Minéralogie, l'Eau, les Glaces et l'Activité on board the Mars Express spacecraft (OMEGA/MEX): Global mineral maps. *J. Geophys. Res.* 112, E08S02. doi:10.1029/2006JE002840.
- Poulet, F., Mangold, N., Loizeau, D., Bibring, J.-P., Langevin, Y., Michalski, J., Gondet, B., 2008. Abundance of minerals in the phyllosilicate-rich units on Mars. *Astron. Astrophys.* 487, L41–L44.
- Putzig, N.E., Mellon, M.T., 2007. Apparent thermal inertia and the surface heterogeneity of Mars. *Icarus* 191, 68–94. doi:10.1016/j.icarus.2007.05.013.
- Putzig, N.E., Mellon, M.T., Kretke, K.A., Arvidson, R.E., 2005. Global thermal inertia and surface properties of Mars from the MGS mapping mission. *Icarus* 173, 325–341.
- Quantin, C., Allemand, P., Delacourt, C., 2004. Morphology and geometry of Valles Marineris landslides. *Planet. Space Sci.* 52 (11), 1011–1022. doi:10.1016/j.pss.2004.07.016.
- Quantin, C., Allemand, P., Mangold, N., Dromart, G., Delacourt, C., 2005. Fluvial and lacustrine activity on layered deposits in Melas Chasma, Valles Marineris, Mars. *J. Geophys. Res.* 110, E12S19. doi:10.1029/2005JE002440.
- Reading, H.G. (Ed.), 1996. *Sedimentary Environments: Processes, Facies and Stratigraphy*, third ed. Blackwell Science, Boston, 688pp.
- Rich, J.L., 1951. Three critical environments of deposition and criteria for recognition of rocks deposited in each of them. *Geol. Soc. Am. Bull.* 62, 1–20.
- Scholten, F., Gwinner, K., Roasch, T., Matz, K.-D., Wählisch, M., Giese, B., Oberst, J., Jaumann, R., Neukum, G., and HRSC Co-Investigator Team, 2005. Mars Express HRSC data processing. *Photogram. Eng. Rem. Sens.* 71 (10), 1143–1152.
- Scott, D.H., Dohm, J.M., Rice, J.W., 1995. Map of Mars showing channels and possible paleolake basins. USGS Misc Invent. Map, I-2416.
- Seidelmann, P.K. et al., 2002. Report of the IAU/IAU working group on cartographic coordinates and rotational elements of the planets and satellites: 2000. *Celest. Mech. Dynam. Astron.* 82, 83–110.
- Smith, D.E., 1999. The gravity field of Mars: Results from Mars Global Surveyor. *Science* 286, 94–97.
- Smith, D.E. et al., 1999. The global topography of Mars and Implications for surface evolution. *Science* 284, 1495–1503.
- Squyres, S.W., 1989. Urey Price lecture: Water on Mars. *Icarus* 79, 229–288.
- Tanaka, K.L., 1986. The stratigraphy of Mars. *J. Geophys. Res.* 91, E139–E158.
- Tanaka, K.L., 1999. What is the significance of layering observed by MOC in martian heavily cratered terrain? In *The Vth International Conference on Mars, Pasadena, (CD-ROM)*. Abstract #6048.
- Tanaka, K.L., Dohm, J.M., Lias, J.H., Hare, T.M., 1998. Erosional valleys in the Thaumasia region of Mars – Hydrothermal and seismic origins. *J. Geophys. Res.* 103, 31407–31419.
- Urabe, A., Tateishi, M., Inouchi, Y., Matsuoka, H., Inoue, T., Dmytriev, A., Khlystov, O.M., 2004. Lake-level changes during the past 100,000 years at Lake Baikal, southern Siberia. *Quater. Res.* 62, 214–222. doi:10.1016/j.yqres.2004.06.002.
- Vail, P.R., 1987. Seismic stratigraphy interpretation procedure. In: Balley, B.B. (Ed.), *Seismic stratigraphic atlas*, AAPG, Studies in geology, 27, Tulsa, pp. 1–10.
- Werner, S.C., 2008. The early martian evolution – Constraints from basin formation ages. *Icarus* 195, 45–60. doi:10.1016/j.icarus.2007.12.008.
- Wilson, S.A., Howard, A.D., Moore, J.M., Grant, J.A., 2007. Geomorphic and stratigraphic analysis of Crater Terby and layered deposits north of Hellas basin, Mars. *J. Geophys. Res.* 112, E08009. doi:10.1029/2006JE002830.
- Zimbleman, J.R., 1998. Possible lacustrine deposits on crater floor as targets for Mars surveyor sample return mission. In: Gulick, V.C. (Ed.), *Mars Surveyor 2001 Landing Site Workshop*. NASA, Washington, DC, USA, pp. 92–93.
- Zurek, R.W., 1982. Martian great dust storms: An update. *Icarus* 45, 202–215.